University of Cape Town

AST5000W

Submitted in fulfillment of the requirements for the degree MSc Astronomy

MeerKAT Observations of Novalike Cataclysmic Variables

Author:

Danté Michael Hewitt

July 2020

The financial assistance of the National Research Foundation (NRF) towards this research is hereby acknowledged. Opinions expressed and conclusions arrived at, are those of the author and are not necessarily to be attributed to the NRF.

Abstract

I have conducted a systematic survey of eleven nearby novalike cataclysmic variables in the radio band, using the MeerKAT radio interferometer. Radio emission is detected from four out of the eleven systems: IM Eri, RW Sex, V3885 Sgr and V603 Aql. While RW Sex, V3885 Sgr and V603 Aql had been previously detected, this is the first reported radio detection of IM Eri. These observations have doubled the sample of non-magnetic cataclysmic varaibles with sensitive radio data. I observe that at these radio detection limits, a specific optical luminosity $\gtrsim 2.2 \times 10^{18}\,\mathrm{erg\,s^{-1}\,Hz^{-1}}$ (corresponding to $M_V \lesssim 6.0$) is required to produce a radio detection. I also find that the X-ray and radio luminosities of the detected novalikes are on an extension of the $L_X \propto L_R^{\sim 0.7}$ power law originally proposed for non-pulsating neutron star low-mass X-ray binaries. No other correlations are found between the radio emission and emission in other wavebands or any other system parameters for the existing sample of radio-detected novalikes. In-band (0.9–1.7 GHz) radio spectral indices are measured, and are found to be consistent with reports from earlier work. I construct broad spectral energy distributions for this sample from published multi-wavelength data, and use them to place constraints on the mass transfer rates of these eleven systems. Finally, I also present the results of time-resolved optical spectroscopy of two little-studied systems in the sample: V5662 Sgr and LSIV -08 3. I obtain orbital periods for these two systems that are consistent with previous measurements in the literature.

Acknowledgements

First and foremost, I would like to express my deepest thanks and appreciation to my primary supervisor, Dr ML (Retha) Pretorius. Over the past few years she has provided me with unrivaled advice, guidance, feedback and support. She has pointed me to more paths of opportunity than I could've hoped for, and played a pivotal role in shaping my scientific mind. Bitter baie dankie vir alles, Retha.

I would also like to extend my deepest gratitude to Prof PA (Patrick) Woudt, my secondary supervisor. He has diligently helped solve every single problem that I have come to him with, and moreover, with a kindness and respect that I greatly admire and aspire towards.

The vast majority of the research done in this dissertation would not have been possible had it not been for the help, lessons, time and endless patience of Dr E (Lilia) Tremou. She went out of her way – every time and without exception, to provide comprehensive answers to my never-ending questions about the arcane art of radio astronomy.

I'm extremely grateful to Dr M (Mickaël) Coriat who also spent a great amount of time, effort and patience teaching me the ins and out of radio astronomy imaging software.

Emma Brooks and Anke van Dyk have been dear friends to me since I moved to Cape Town. They have helped me on an everyday basis, with various life and academic challenges. Anke was even willing to provide compassionate and constructive criticism. Thank you to them, and the rest of my problem-solving friends: Keke, Shilpa, Munira, Petro.

I would like to extend a big thank you to Trystan Lambert for teaching me the ways of the observational astronomer and all his IRAF secrets.

Many thanks to the co-authors that contributed to the publication (arXiv:2006.07918) of some of the work presented here; especially Prof JCA Miller-Jones, Prof C Knigge, N Castro-Segura, Dr DRA Williams and Prof RP Fender.

I gratefully acknowledge the effort of Ben Hugo who took time out of his very busy schedule to help get DDFacet installed on IDIA and walked me through alternative radio data reduction techniques.

Thanks to Dr B (Brent) Miszalksi for help with radial velocity calculations.

Lastly, I would like to acknowledge Dr E Breedt for graciously providing a catalogue of CVs and CV candidates, which was the starting point for this NL survey.

I called and was shown things I did not know.

Contents

Chapter 1

Introduction

Many astrophysical objects undergo accretion during one stage of their lifetime or another. These accreting objects range from young stellar objects in cosmic nurseries, to the remnants of stellar evolution that include non-relativistic white dwarfs (WDs), as well as relativistic neutron stars (NSs) and stellar-mass black holes (BHs). The supermassive BHs that power active galactic nuclei (AGN) are the most massive and energetic examples of accreting objects. In the case of WDs, NSs and BHs, the physical processes that govern the disc-fed accretion and outflow phenomena (such as collimated disc winds or jets) are coupled. Moreover, across this vast range of objects, spreading over several orders of magnitude in mass and size, this *disc-jet coupling* seems to be remarkably universal. These accreting compact objects (ACOs) are the subject of this work.

Radio emission is typically used as a tracer for relativistic collimated outflows (jets) from ACOs, while what is used as a proxy for the accretion rate onto the object, is dependent on the type of ACO. In X-ray binary systems (XRBs; binary systems in which a NS or stellar mass BH accretes material from a stellar companion), the X-ray emission is generally representative of the accretion rate onto the NS or BH. In the literature there is substantial evidence that the physical processes responsible for X-ray and radio emission in low-mass XRBs (henceforth simply referred to as XRBs) are connected. From an observational point of view, a very strong non-linear correlation exists between the X-ray and radio emission of stellar mass BH XRBs in the low accretion, spectrally hard X-ray state (Hannikainen et al. 1998; Corbel et al. 2000, 2003; Gallo et al. 2003; Coriat et al. 2011; Corbel et al. 2013; Tetarenko et al. 2016b; Gallo et al. 2018).

The connection between X-ray and radio emission also spans across various classes of BHs.

Merloni et al. (2003) examined BHs ranging from stellar mass to supermassive, and found that the radio luminosity is highly correlated with both the black hole mass and X-ray luminosity. The authors also found that the disc-jet coupling is well described by the scale-invariant relation between the flux of accretion-powered jets and the mass of the compact object ($F_\nu \sim M^{17/12}$) as derived by Heinz & Sunyaev (2003). Similar work was done by Falcke et al. (2004) that reached analogous conclusions: for BHs across more than seven orders of magnitude in mass, including XRBs (in the hard and quiescent state) and AGN (which include LINERS, FR I radio galaxies and BL Lac objects), the radio and X-ray emission correlate at a significant level.

The discovery of ultra-relativistic outflows in NS systems, comparable with those observed in AGN (Fender et al. 2004b), has shown that outflows of this extreme nature do not require properties unique to BHs (e.g. an event horizon). Furthermore, canonical black hole states can largely be mapped onto NS equivalents, highly suggestive of a ubiquitous physical mechanism (Klein-Wolt & Van der Klis 2008; Migliari & Fender 2006). NS XRBs also show a significant X-ray:radio correlation, and while there is ongoing debate regarding the exact correlation index, a recent study by Gallo et al. (2018) has found that the relation for NSs and BHs are in fact consistent with one another, within 2.5σ. Of great importance to this dissertation, is that the connection between jet power and the inner accretion flow seems to not (entirely) be dependent on the nature of the compact object, but rather on what can be deduced as the accretion rate (e.g. Migliari & Fender 2006). The differences that do exist between these classes of objects, can most likely be attributed to the existence of a boundary layer in NS XRBs.

White dwarfs (WDs) represent the weak-field gravity regime and thus provide an important test case for the universality of accretion and jet formation. Of all the classes of compact objects they are also the most numerous, yet remain the most poorly-studied at radio frequencies. Jets have been observed in various classes of accreting WDs, including supersoft X-ray sources (e.g. Southwell et al. 1996), symbiotic systems (e.g. Taylor et al. 1986), and related to nova eruptions (e.g. Sokoloski et al. 2008).

Recently, other types of accreting WDs have received more attention. Coppejans et al. (2015, 2016) showed that novalike systems (NLs) and dwarf novae (DNe) in outburst, and thus ultimately non-magnetic cataclysmic variables (CVs), are significant sources of radio emission. Coppejans et al. (2015) detected three NLs at radio frequencies: RW Sex, TT Ari and V603 Aql, and five DNe (Coppejans et al. 2016): RX And, SU UMa, U Gem, YZ Cnc and Z Cam. The radio luminosity does not seem to be correlated with the optical luminosity, orbital period or the subclass of CV, however, possible correlations might be masked by the low cadence of

the observations. Initial surveys to detect radio emission from the non-magnetic CVs, including the NLs RW Sex and TT Ari (Cordova et al. 1983; Nelson & Spencer 1988), V603 Aql (Fuerst et al. 1986), and MV Lyr (Nelson & Spencer 1988) were unsuccessful. In fact, prior to the work done by Coppejans et al. (2015, 2016), only five non-magnetic CVs had been detected at radio wavelengths: EM Cyg (Benz & Guedel 1989), SU UMa (Benz et al. 1983), TY Psc (Turner 1985), SS Cyg (Körding et al. 2008) and V3885 Sgr (Körding et al. 2011). Non-detections of CVs in the radio regime led to the belief that CVs do not launch jets, which was used to constrain jet launching models (e.g. Livio 1999). However, since then, SS Cyg has been observed to launch transient jets, producing synchrotron emission (Körding et al. 2008; Miller-Jones et al. 2011; Russell et al. 2016; Mooley et al. 2017; Fender et al. 2019). Körding et al. (2008) compared XRB and CV accretion states and scaled down the outflow-accretion coupling observed in XRBs to CVs. They showed that the radio emission in DNe peak at the start of an outburst and subsequently decline (within $\sim$24 hours) to very low levels, which would have been undetectable by the earliest surveys, thereby explaining numerous non-detections in literature. Moreover, the sensitivity of surveys in the 20th century was simply insufficient (Coppejans et al. 2015). It is thus clear that across these classes of objects, the accretion/outflow phenomena are, at least to some degree, equivalent.

Despite this knowledge, there is still no clear understanding of the presence and nature of radio emission in accreting WDs. With the inauguration of MeerKAT (Jonas 2009) in 2018, the South African Square Kilometer Array (SKA) pathfinder, we now have access to unprecedented sensitivity with which to observe these objects. In this dissertation I will report on eleven nearby NLs that have been observed by MeerKAT as part of its Large Survey Project (LSP) for explosive transients: ThunderKAT (The Hunt For Dynamic and Explosive Radio Transients with MeerKAT).

In **Chapter 2** and **Chapter 3** I discuss the necessary background regarding cataclysmic variables and disc-jet coupling, respectively. In **Chapter 4** I give an overview of radio interferometry and aperture synthesis imaging. The survey of NLs, including a brief overview of each target and details of the observations and data calibration, is discussed in **Chapter 5**. The results of the MeerKAT radio observations and time-resolved optical spectroscopy of a select few systems are presented and discussed in **Chapter 6**. **Chapter 7** summarises the findings of this research. Finally, in **Chapter 8** I look forward, discussing how the research I present here can be be expanded, and also what work needs to be done in future to make advances in the field.

Chapter 2

Cataclysmic Variables

The timescales associated with astrophysical events are typically enormous and nigh incomprehensible, but exceptions to the norm do exist. One specific type of astrophysical object displays variability on humanly observable timescales and magnificently explosive phenomena that have astounded earthly onlookers for centuries: the *cataclysmic variable*. Cataclysmic variables (CVs) are semidetached binary star systems in which a white dwarf (WD) accretes mass from a late type main sequence star (usually a K or M type red dwarf) via Roche lobe overflow (comprehensive reviews are given by Warner (1995) and Hellier (2001), which are also the main sources for this chapter). Stars are born in massive interstellar clouds of dust and gas, seldom forming alone and usually gravitationally bound to other nearby stars. Of particular interest to this dissertation are the binary systems with an orbital period of $\sim$10 years, with one star more massive than the sun and one less massive. These systems are the progenitors of cataclysmic variables.

In the accepted scenario (Warner 1995) for CV formation, the more massive star evolves to become a red giant, which engulfs the less massive secondary companion during a *common envelope phase* (Paczynski 1976). Consequently, the system experiences significant drag and the orbital separation reduces to a few solar radii. Eventually, this envelope is ejected, carrying away a large amount of angular momentum which reduces the orbital separation even more, resulting in a detached binary system with a WD primary companion. For mass transfer to commence (and a CV to be born), the secondary star either needs to expand sufficiently during its evolution, or the orbit needs to shrink even further through some angular momentum loss mechanism.

2.1 Roche Geometry

To understand the mechanism of mass transfer in CVs, a discussion of Roche geometry is needed. Consider a short period binary system consisting of a more massive primary star with a mass M_1 and a less massive secondary donor star with a mass M_2. The stars are following circular orbits around the center of mass of the system (the orbits are circular because of strong tidal interaction).

Stars consist mostly of hydrogen, and so the flow of the gas can be described by the Euler equation (as for any other fluid)

$$\rho\left(\frac{\partial \vec{v}}{\partial t} + \vec{v} \cdot \boldsymbol{\nabla} \cdot (\vec{v})\right) = -\boldsymbol{\nabla} \cdot p + f_{ext}\rho \tag{2.1}$$

where $\rho, \vec{v}$ and p are the density, velocity and pressure of the fluid respectively, and f_{ext} is the external force per unit mass that the fluid is subjected to.

At any given point within the system a gas particle will be subjected to a potential – the Roche potential Φ, which is the sum of the gravitational and centrifugal forces on the particle. The mass ratio of the stars, $q = M_2/M_1$, will govern the shape of the equipotential surfaces of the Roche potential. The intersection of a few equipotential surfaces with the orbital plane is shown in Figure 2.1. A special equipotential forms a figure eight shape, and the corresponding teardrop-shaped surfaces are called the *Roche lobes* of the stars. They define the critical equipotential beyond which mass loss will occur, because they are the largest close equipotentials that can contain the masses of the stars.

The overall size of the lobes are set by the binary separation. Lagrangian points are equilibrium points of the equipotential. The inner Lagrangian point L_1, is a saddle point where forces effectively cancel one another ($\Delta\Phi = 0$) and thus the most effective means of mass transfer from one star to the other is through L_1 when a Roche lobe is overfilled.

A binary system is called *detached* when both stars lie within their respective Roche lobes, *semi-detached* if a single Roche lobe is filled or a *contact binary* if both Roche lobes are filled. Roche lobe overflow (and consequent mass transfer) naturally requires a semi-detached system which can occur either when the secondary expands and fills its Roche lobe during the late stages of its life, or as the orbital separation shrinks and the Roche lobes consequently fills, as a result of angular momentum loss in the secular evolution of cataclysmic variables.

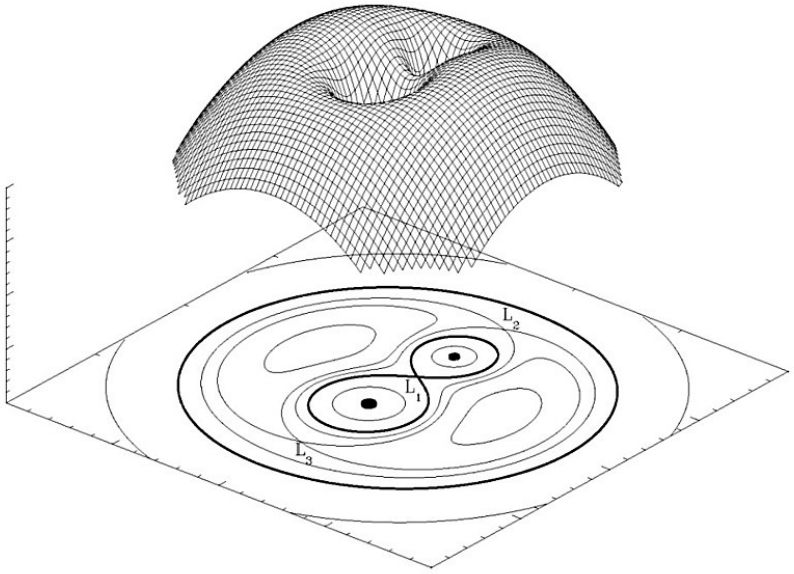

Figure 2.1: An illustration of the Roche potential of a binary system. The larger Roche lobe belongs to the more massive WD. L_1, L_2 and L_3 are Lagrangian points. L_4 and L_5 are not indicated on this illustration.
Source: Marc van der Sluys, URL: http://hemel.waarnemen.com/Informatie/Sterren/hoofdstuk6.html#h6.2

2.2 Accretion Flow Geometry

The geometry of the accretion flow onto the primary in cataclysmic variables is largely governed by the magnetic field strength of the primary. In non-magnetic CVs (non-magnetic meaning that the WD magnetic field strength $B \lesssim 10^5$ G, e.g. Coppejans & Knigge 2020), the ram pressure of the gas is greater than the magnetic field pressure and accretion occurs via an accretion disc. For WDs with magnetic field strengths of $B \gtrsim 10^7$ G, matter attaches directly to the field lines of the WD and accretes to the poles, since the magnetic field pressure exceeds the ram pressure of the incoming material. These CVs are called *polars* (or AM Her stars after the defining class member; Tapia 1977), derived from the polarised light that they produce as a result of their strong magnetic fields. In an intermediate case, WDs with magnetic field strengths 10^5 G $\lesssim B \lesssim 10^7$ G, an accretion disc forms, but the inner disc is truncated at the Alfv́en radius and channelled to the poles – these CVs are known as *intermediate polars* (or sometimes DQ Her stars; Patterson 1994).*

*Direct measurements of the primary WD magnetic field strength have only been made for a minority of systems, and mostly only for the most strongly magnetic ones. Our classification of systems into non-magnetic, polar, or IP is based on other phenomenology, mainly the photometric behaviour.

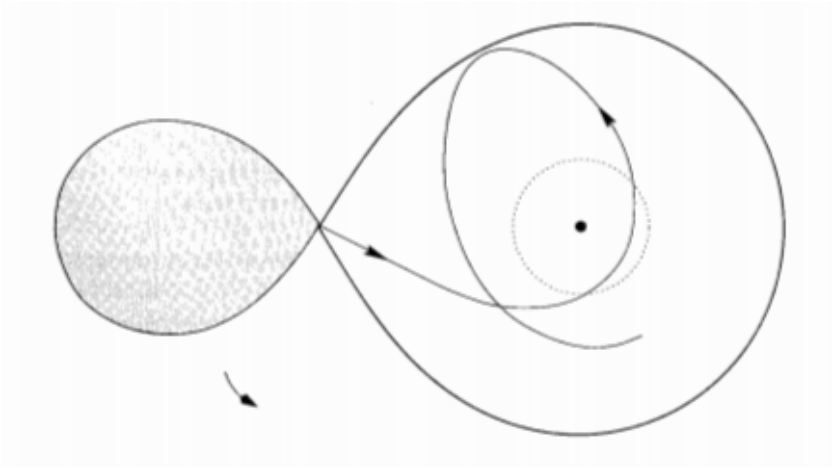

Figure 2.2: The trajectory of the stream (the solid line with arrows) as it is injected from the secondary's Roche lobe (the grey lobe on the left) into the primary's lobe. The dotted ring represents the circularisation radius. This trajectory is as seen from a rotating reference frame. Source: Hellier, C. (2001). Cataclysmic variable stars. London: Springer, p.25.

2.2.1 Non-magnetic CVs

For non-magnetic CVs, when the secondary overfills its Roche lobe, the material is injected into the empty space of the primary's Roche lobe and is accelerated towards the WD. The velocity of the material changes as it approaches the WD due to the gravitational force acting on it, but the angular momentum of the material remains the same as at the L_1 point. Consequently the material does not fall directly to the surface of the WD, but forms a thin stream that starts to orbit the WD due to the Coriolis force (e.g. Flannery 1975; Lubow & Shu 1975). The stream then follows a trajectory moving close by the WD, curving and slamming back into itself, eventually settling into an orbit at a radius which has the same angular momentum as the L_1 point – *the circularisation radius* (see Figure 2.2).

Keplerian motion dictates that the material in the inner annulus will move faster than material with a slightly bigger orbit, but also have lower angular momentum. This implies relative motion between material in slightly smaller and larger orbits. The viscosity of this material is a key ingredient for disc formation (and thus ultimately accretion onto the primary and the outward transportation of angular momentum). This viscosity does not originate from molecular interactions, but is the result of magnetorotational, or Balbus-Hawley instabilities (Hawley & Balbus 1991; Balbus & Hawley 1991, 1998, see Section 3.1 for a discussion). The viscous interactions of the material at different radii result in friction which liberates gravitational potential

energy and heats up the gas, but also shrinks the inner orbit. To conserve angular momentum, the material on the outer edges also spreads out to larger radii and a thin disc forms. Eventually the spreading of the disc will stop as inner regions come into contact with a boundary layer and outer regions lose angular momentum to tidal reactions from the secondary (Harrop-Allin & Warner 1996). The interaction at the boundary layer liberates large quantities of kinetic energy, either as soft X-ray and EUV emission, or hard X-ray emission, depending on accretion rate and optical depth (e.g. Patterson & Raymond 1985a,b). More mass is continually transferred from the L_1 point to the disc and inward, while angular momentum is transferred outward, sustaining the disc. From this point onward, the stream of material coming from the L_1 point will hit the disc edge-on. This interaction is turbulent and highly energetic, resulting in a bright spot at the collision zone which can account for a large fraction of the optical emission in a CV.

2.2.2 Polars

In the case where the WD has a strong magnetic field ($B \gtrsim 10^7$ G), its spin period and the system's orbital period synchronise (e.g. Cropper 1990). It is worth mentioning that the orbital separation also plays a role in synchronisation. In this case, the stream of material entering through the L_1 point will initially follow the same trajectory as the non-magnetic case until it reaches the WD's *magnetosphere*. The magnetosphere is the zone surrounding the WD where the magnetic field dominates and other forces are mostly insignificant. The magnetic field strength drops rapidly with increasing distance from the WD (inverse square relation), and at the magnetospheric boundary the field induces electric currents in the plasma which effectively act as a screen, counteracting the effect of the field on material outside the magnetosphere. There is also the possibility of the WD magnetosphere being sufficiently large that it reaches the donor or already dominates at the L_1 point (e.g. Schmidt et al. 1999). In this case the incoming stream from the $L1$ point immediately follows the field lines to the WD magnetic poles.

Once the stream is sufficiently close to the WD, the nature of the matter starts to change due to the magnetic pressure. The stream fragments into smaller globules and some of the material diffuses into a misty haze. The plasma accumulates in a region called the *threading region* which extends over a range of radii ascribed to the difference in densities of the captured material (Liebert & Stockman 1985; Hameury et al. 1986). From different radii in the threading region, different densities of material will follow the field lines to the accretion region. The magnetically controlled plasma spirals around the field lines, resulting in polarised cyclotron

emission (Chanmugam & Dulk 1981). The accretion region is necessarily also elongated into an arc close to the magnetic pole. The more dense globules of material have enough momentum to hurl into the WD; their energy being absorbed and then emitted as black body radiation in the soft X-ray regime. The finer haze impacts the WD where it forms a mound-like accretion column. New incoming material hurling into the accretion column creates a violent accretion shock, resulting in bright hard X-ray bremsstrahlung emission.

2.2.3 Intermediate Polars

WDs with a magnetic field strength of $10^5\,\mathrm{G} \lesssim B \lesssim 10^7\,\mathrm{G}$ present an intermediate case where an accretion disc is permitted to form, but the inner disc is truncated and fed to the poles via magnetic field lines. These are asynchronous systems where the WD spin period is typically much shorter than the orbital period. Similar to polars, the light curves of IPs exhibit very stable optical and X-ray pulsations. Observationally, they are distinguished from polars by the aforementioned asynchronism and the absence of strong circular polarisation, explained by weaker magnetic fields and larger accretion rates and orbital separations (Patterson 1994). In the case where the magnetic field strength is weak enough that the radius of the magnetosphere is smaller than the stream's closest initial approach, an accretion disc forms normally and is disrupted at the magnetospheric boundary from where field lines will govern the accretion flow (resulting in an inner flow called *accretion curtains*, as in Figure 2.3). If the magnetic field strength is large enough to manifest a magnetospheric radius greater than the circularisation radius, no accretion disc will form (e.g. Hellier & Beardmore 2002). An intermediate field strength will result in denser globules of material being allowed to ignore the field, aided by the screening effect of the induced currents. Eventually an accretion disc forms when enough dense material has gathered at the circularisation radius (e.g. King & Wynn 1999).

2.3 Outbursts and Eruptions

The mass transfer rate ($\dot{M}$) regulates the stability of the accretion disc in non-magnetic CVs. If $\dot{M} \lesssim 10^{-9}\ \mathrm{M}_\odot\,\mathrm{yr}^{-1}$[†], the accretion disc is unstable and thermal-viscous instabilities can cause the disc to switch between a faint, low-$\dot{M}$ and bright, high-$\dot{M}$ state (the disc instability model; Osaki 1974; Hoshi 1979; Lasota 2001). These episodic outbursts are termed *dwarf nova outbursts* and CVs that exhibit this phenomenon are called *dwarf novae* (DNe). A mass transfer

[†]The exact mass transfer rate is dependent on the disc size and hence orbital period.

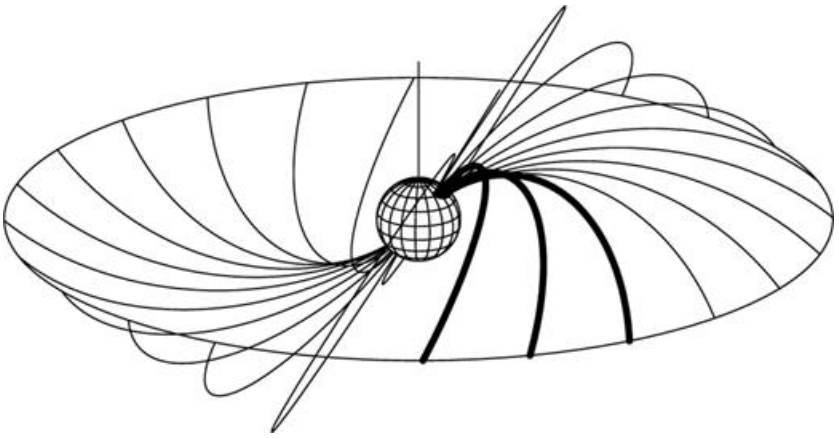

Figure 2.3: The field lines pattern showing how one side of the inner edge of the accretion disc in an IP is fed to the upper pole, while the other side is fed to the lower pole. Here, a system is shown with misaligned magnetic and spin axes. This is the result of complicated interactions between the magnetosphere and an accretion disc that is tilted with respect to the WD orbital plane.
Source: Andrew Beardmore in Hellier, C. (2001). Cataclysmic variable stars. London: Springer, p.136.

rate $\gtrsim 10^{-9}\mathrm{M}_{\odot}\,\mathrm{yr}^{-1}$ is sufficient to ensure that the accretion disc is in a perpetual high-$\dot{M}$ state and stable against outbursts (Osaki 1996; Dubus et al. 2018). Systems in which DN outbursts have not been observed are termed *novalikes* (NLs). NLs can have brightenings of up to a few magnitudes, as well as deep low states, associated with the accretion disc. All non-magnetic CVs are divided into either the DN or NL class, dependent on the presence or absence of DN outbursts: non-magnetic systems that show these oubursts are DNe, those that do not are NLs.

Extremely energetic transient events that give rise to an even greater magnitude increase (usually more than 8 magnitudes) are also observed, although these events are not linked to the accretion disc. One type of these events is the *nova eruption*.

2.3.1 Dwarf Novae

DNe are a subclass of CVs that show repeating outbursts during which the system's optical brightness increases by approximately 2 to 8 magnitudes within approximately a day and remains in this state for a few days or weeks, before declining to its fainter quiescent state again. These outbursts recur on timescales of days to decades (but more typically weeks to years for the observed sample).

As mentioned these DN oubursts can be explained using the framework of the disc instability model (Osaki 1974; Hoshi 1979; Lasota 2001). A DN outburst is the result of a thermal-viscous

instability in the accretion disc of the WD, which switches the disc from a cool, faint, low-viscosity state to a bright, hot, high-viscosity state. A relatively constant mass transfer rate from the secondary results in a surplus of material being accumulated in the disc, as only a set amount of material can be accreted onto the WD by viscous interactions. The excess material eventually causes the viscosity of the entire disc to increase, which in turn increases angular momentum transport, accretion onto the primary and the luminosity of the system (Smak 1971; Osaki 1974). Once the disc has been "drained" (in reality only a fraction of the total disc mass is accreted) onto the WD, the disc returns to the quiescent state and starts to build-up material again, which will trigger the next outburst.

The commonly accepted origin of the viscosity in the accretion disc is explained by Balbus-Hawley instabilities (Hawley & Balbus 1991; Balbus & Hawley 1991, 1998, see Section 3.1 for a discussion). The driving mechanism of the disc is magnetic turbulence and for Balbus-Hawley instabilities to occur, strong coupling between magnetic fields and the disc matter is required, which is only possible when the material is ionised. In outburst, the disc is highly ionised and free electric charge is abundant so the Balbus-Hawley instabilities are more effective. In the cooler quiescent state this free electric charge is captured by nuclei to form neutral atoms.

The mechanism that switches the disc between its two states of equilibrium is closely linked to the opacity of the disc material. In partially ionised hydrogen gas, opacity scales with temperature to the tenth power (e.g. Faulkner et al. 1983). When hydrogen is heated to $\sim$7000 K, it becomes partially ionised and the opacity increases. Adding more heat to the system, leads to more hydrogen atoms becoming ionised rather than increasing the heat of the system. The increase in ionised hydrogen results in more heat being trapped and a runaway reaction occurs where the temperature increases until all of the hydrogen is ionised and the disc settles into a new equilibrium state at a higher viscosity and temperature due to more efficient Balbus-Hawley instabilities. Additionally, as hydrogen becomes ionised, H^- ions form which aid in the trapping of electromagnetic radiation, thereby further increasing the opacity.

This process is also well described by an s-curve (e.g. Hoshi 1979; Lasota 2001; Hellier 2001). In Figure 2.4 the equilibrium states of the disc have been plotted, mimicking an s-shape, with solid and dashed lines representing stable and unstable equilibrium, respectively. The y-axis represents the effective temperature of the disc, and the x-axis the surface density (mass per unit disc area). Consider the disc in its cool quiescent state at A. If the mass transfer rate from the secondary is greater than the flow of material inwards through the disc, then a pile-up of material will occur. Gradually the surface density of the disc increases, which also increases

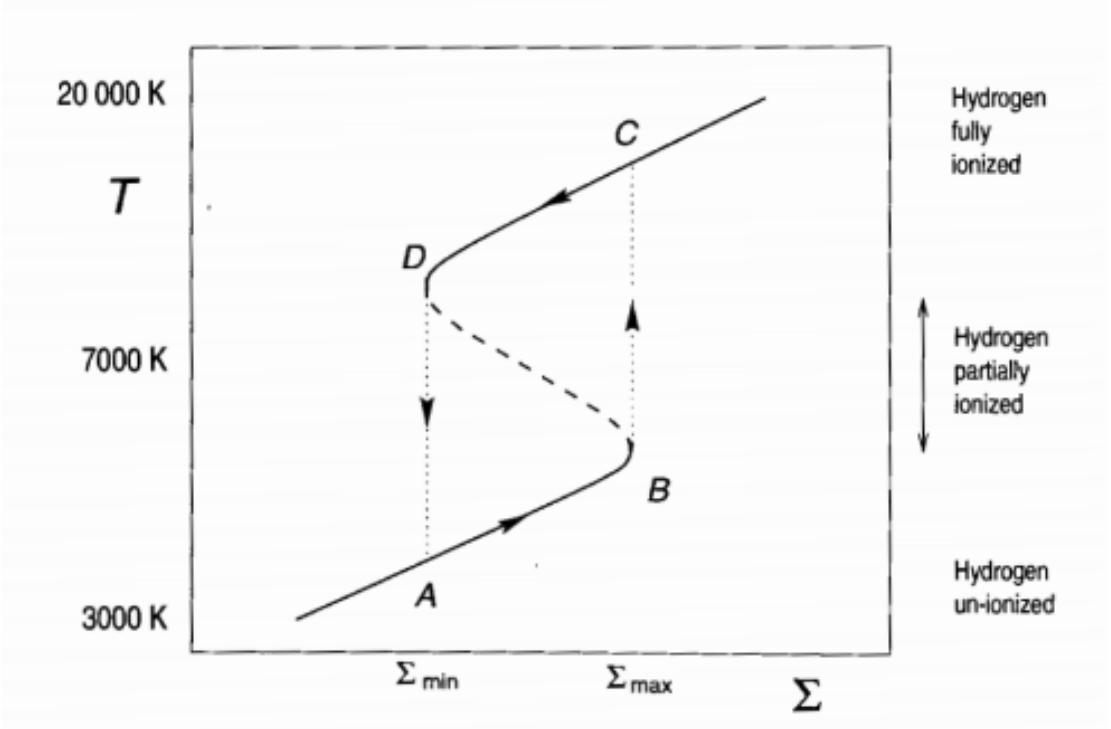

Figure 2.4: The dwarf nova outburst cycle plotted as surface density (mass per disc area) against disc temperature. Solid and dashed lines represent stable and unstable equilibrium values, respectively. A system can of course also be found off the s-curve in this space, but it would then not be in equilibrium.

Source: Hellier, C. (2001). Cataclysmic variable stars. London: Springer, p.64.

the viscosity and thus the temperature of the disc. The disc now moves towards state B where hydrogen gets partially ionised. At this stage, a further increase in surface density gives rise to a runaway increase of temperature (because of the ionisation and, hence, increased opacity). The disc moves up to state C, since the heating timescale is shorter than the viscous-interaction timescale. Here ($C \rightarrow D$) the disc settles into the new hot, high-viscosity equilibrium state. The inward flow of material is however now higher than mass transfer rate from the secondary and the disc "drains" onto the primary. This decreases the surface density of the disc, leading to lower viscosity and lower temperatures and the disc moves to D. At this lower temperature the hydrogen becomes only partially ionised again, the opacity drops and consequently the temperature decreases greatly on a very short timescale. The ions recombine and the disc returns to its quiescent equilibrium state at $A \rightarrow B$.

2.3.2 Novalike Variables

Should the mass transfer rate from the secondary be sufficiently large, the disc can be perpetually sustained in the hot, high-viscosity state. These CVs are called *nova-like variables*, or more recently simply *novalikes* (NLs; e.g. Osaki 1996; Dubus et al. 2018). Observers realised that these stars are very similar to stars that have undergone nova eruptions, hence the name. It's important to note that our classification of objects as NLs or DNe is mostly phenomenological, and due to poorly sampled light curves DNe could be misclassified as NLs for example.

Humps

Nearly all short period NLs display permanent superhumps in their light curves. These are photometric humps with a period slightly longer than the orbital period. Superhumps are explained to be the result of the precession of a large elliptical disc (Vogt 1982; Osaki 1985). This is caused by an eccentric instability which grows at the 3:1 resonance and then the disc precession is initiated by tidal interactions of the outer disc with the secondary[†] (Whitehurst 1988; Hirose & Osaki 1990; Lubow 1991).

Negative superhumps are humps with a period slightly shorter than the orbital period, best explained as retrograde nodal precession of the accretion disc (Patterson 1999).

In CVs and low mass XRBs, the presence of both suborbital and superorbital signals are commonly accepted to be the result of an accretion disc that is tilted with respect to the orbital

[†]If the mass ratio $q \gtrsim 0.33$

plane (e.g. Patterson et al. 2005).

Subclasses of NLs

There are various subclasses of NLs, including RW Tri, SW Sex, UX UMa and VY Scl stars. Systems can belong to more than one of these types.

- RW Tri types have pure emission line spectra (occasionally with deep absorption cores) and are believed to be generally higher inclination systems than UX UMa types.

- SW Sex stars are a peculiar subclass of NLs, first put forward by Thorstensen et al. (1991). These systems are usually eclipsing NLs that show single peaked Balmer emission lines, rather than double-peaked lines as one would expect from a high inclination system. These systems show peculiar absorption features in the Balmer and He I emission lines, but only surrounding a phase of 0.5. The radial velocity curves that are determined from the emission lines show a significant phase lag behind that of the WD orbital motion determined through photometric eclipses. Furthermore, these systems are found just above the period gap (see Section 2.4) with orbital periods between 3 and 4 hours. Hellier (1996) has proposed a model that explains these features by assuming very high mass transfer rates that result in disc overflow and accretion winds.

- UX UMa NLs show no low states. Their spectra exhibit permanent broad Balmer absorption lines due to optically thick geometrically thin accretions discs. They are typically low inclination systems.

- VY Scl types (sometimes referred to as 'anti-DNe') are a subclass of NLs, that on occasion enter low states, fading by a few magnitudes as a result of decreased/quenched mass transfer for a period of weeks to years. Possible explanations include star spots (e.g. Livio & Pringle 1994) and irradiation-driven mass transfer (Wu et al. 1995). In this low state, their spectra look like those of DNe, but they show no DN outbursts.

2.3.3 Novae

Nova eruptions are incredibly violent events during which a thermonuclear runaway on the surface of a WD causes the shell of the WD to explode and be expelled, leading typically to an 8 to 15 magnitude increase in the system's optical brightness (for reviews, see Shara 1989;

Warner 1995; Bode & Evans 2008). Historically this has led to observers witnessing a 'new star' or *stella nova*, hence the name.

The mass accretion in cataclysmic variables continually provides a degenerate WD with new fresh hydrogen that could potentially reignite nuclear fusion reactions. The newly acquired material on the surface of the WD is subjected to extremely high pressures and temperatures due to the star's high density. The reaction that starts this cataclysmic event involves one proton releasing a positron to become a neutron and combining with a second proton to form deuteron. The deuteron nucleus can then combine with another proton to form helium. Large amounts of energy are released during this process and in normal matter this would result in an increase in pressure which causes the matter to expand and cool down. WDs, however, consist of degenerate matter, in which the pressure is only density-dependent. Any heat that is added to the system will thus only increase the temperature, which in turn increases the reaction rate and gives rise to more energy being released – a runaway reaction ensues. Once temperatures of $\sim 2\times10^7$ K are reached, the hydrogen can burn even more efficiently making use of carbon, nitrogen and oxygen as catalysts, which absorb protons, forming radioactive nuclei. These reactions are extremely temperature dependent ($\propto T^{18}$) and at $\sim 10^8$ K the surface layer becomes fully convective, pushing the radioactive matter to the surface and siphoning down the newly accreted hydrogen as fresh fuel. When the gas pressure exceeds the degeneracy pressure the shell explodes and engulfs the binary which propels it outwards (e.g. Starrfield et al. 2000).

All CVs are expected to undergo nova eruptions at some stage with recurrence times of $10^4 - 10^6$ years (e.g. Shara et al. 1986). Systems in which only a single one of these nova eruptions has been observed are called *classical novae*. Some systems have shown multiple nova eruptions – these are classified as *recurrent novae*.

2.4 CV Evolution

Mass transfer from the less massive secondary to the more massive primary star via Roche lobe overflow, will result in the transferred material being closer to the center of mass of the system and thus losing angular momentum. In order for angular momentum to be conserved the binary separation needs to increase, which would cause mass transfer to cease. In order to ensure relatively stable mass transfer in the long term, either the secondary needs to increase in size, keeping contact with its Roche lobe, or the binary separation needs to decrease, driven by some angular momentum loss mechanism. In the former case, this is possible if the secondary evolves

into a red giant star. While valid, this still fails to explain the vast majority of cataclysmic variables where the secondary is a low mass star that simply could not have existed long enough to evolve to the red giant stage. For the latter case, two mechanisms are considered to be responsible for the gradual loss of angular momentum: magnetic braking and gravitational radiation.

2.4.1 Mechanisms for Secular Angular Momentum Loss

The red dwarf secondaries in cataclysmic variables are believed to have reasonably large magnetic fields because of their short spin periods, since the secondaries are tidally locked to the binary orbits. Wind outflows from these secondaries will result in ionised particles being trapped by the magnetic field lines and forced to co-rotate with the secondary even at relatively large distances from the surface. As these particles are dragged along, they are accelerated to high speeds and get flung away into space, taking with them a considerable amount of angular momentum. This loss of angular momentum brakes the rotation of the secondary star, but since the spin and orbit are tidally locked, the angular momentum is effectively supplied by the orbit, which shrinks in response. This process is called *magnetic braking* (Eggleton 1976; Verbunt & Zwaan 1981; Rappaport et al. 1983).

The second angular momentum-loss mechanism is *gravitational radiation* – the electromagnetic light-equivalent of gravity (Kraft et al. 1962; Paczyński 1967; Faulkner 1971; Paczynski & Sienkiewicz 1981). Massive accelerating objects curve space-time, sending out waves that warp the space-time as they propagate. In the case of a binary star system where two massive objects are persistently orbiting one another, the energy required for the gravitational waves to manifest is extracted from the orbit of the system. Consequently, as gravitational waves are radiated away, the orbit shrinks. Gravitational radiation is more significant for close orbiting binary systems.

2.4.2 Observed Orbital Period Distribution in CVs

In Figure 2.5 the observed distribution of orbital periods for cataclysmic variables is shown. There are a few interesting features. Firstly, there is a short period cut off at $\sim$80 minutes and a more gradual decline at long periods, dropping to almost zero by $\sim$ 10 hours. Very few systems are found with orbital periods outside these bounds. Additionally, there is a period gap between $\sim$ 2 and 3 hours.

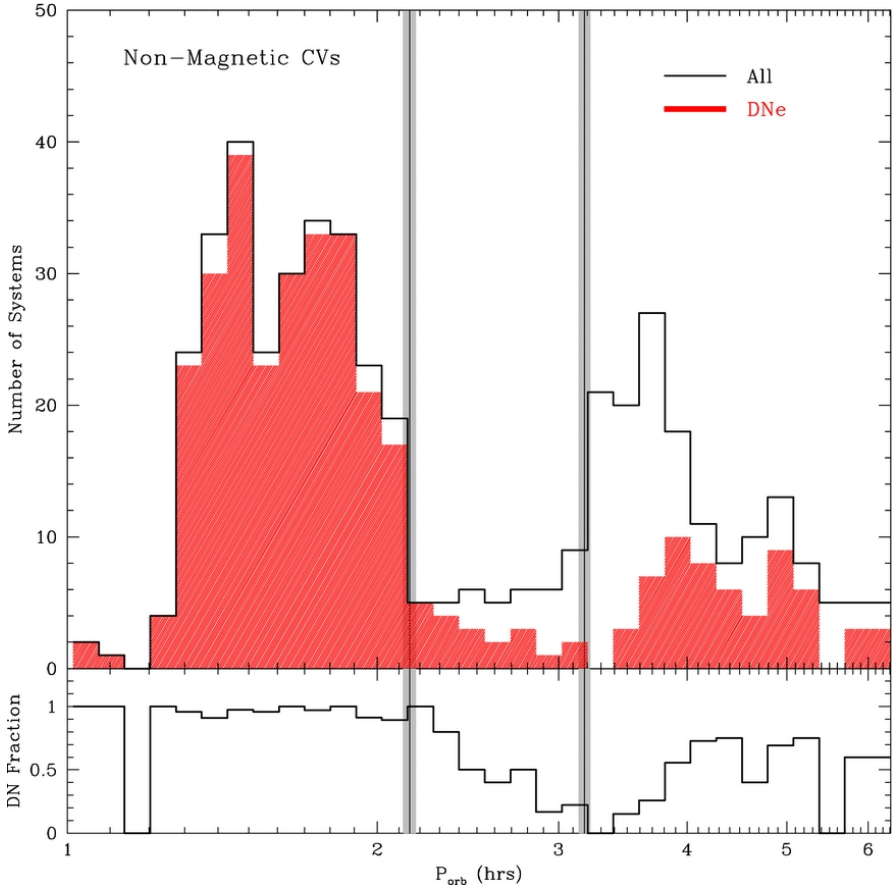

Figure 2.5: Orbital period distribution of non-magnetic CVs in the Ritter & Kolb (2003) catalogue (v7.11). The orbital period distribution of DNe are shaded in red. In the bottom panel: the DN to all non-magnetic CVs ratio is shown as a function of orbital period. The vertical black lines mark the lower and upper edges of the period gap, while the grey shading represents the errors in these limits.

Source: Knigge et al. (2011), Figure 18

The lower limit of the orbital period distribution, referred to as the *period minimum*, at ∼80 minutes is explained by the fact that an orbital period this short implies a mass so low for the secondary that it will become degenerate. Ordinarily more massive non-degenerate stars have larger radii and adding mass to such a star will cause it to expand. In the case of a degenerate star, however, a decrease in the mass of the star will result in an increase of the radius of the star (e.g. Kolb & Baraffe 1999). Therefore, at some orbital period (around 80 minutes) mass loss from the low mass degenerate secondary will cause it to expand, resulting in an increase in the orbital period, and a 'turn-around' point producing the period minimum (e.g. Paczynski & Sienkiewicz 1981; Rappaport et al. 1982). Nevertheless, a few systems are found below the period minimum: AM CVn stars (see e.g. Nelemans 2005 for a review). These systems have secondaries that consist mostly of helium, allowing for more compact stars and thus orbital periods even shorter than the period minimum.

The long period "cut-off" is a result of the Chandrasekhar limit. WDs must have a mass less than $\sim 1.4\,\mathrm{M}_\odot$ and to ensure stable, conservative mass transfer $q = M_2/M_1 \lesssim \frac{5}{6}$ [‡], implying that $M_2 \lesssim 1.2\,\mathrm{M}_\odot$ (e.g. Frank et al. 1992; Smith & Dhillon 1998). This imposes a limit on the size of a fillable secondary Roche lobe, which in turn limits the orbital period (to ~ 10 hours). Most WDs are however less massive than the Chandrasekhar limit (the mean WD mass among eclipsing CVs $\approx 0.8\,\mathrm{M}_\odot$, Knigge et al. 2011), so the number of observed CVs already starts to significantly decrease as a function of period from about 6 hours. The odd outlier system that does have a very long orbital period, achieves this by having a secondary that is evolving to become a much larger red giant, and can thus fill a larger Roche lobe at an orbital period $\gtrsim 10$ hours.

The standard model for the secular evolution of CVs, which also describes the period gap, is the one for disrupted magnetic braking (Paczynski & Sienkiewicz 1983; Rappaport et al. 1983; Spruit & Ritter 1983). The evolution of CVs above the period gap ($P_{\mathrm{orb}} > 3$ hrs) is believed to be governed by magnetic braking ($\dot{M} \sim 10^{-9} - 10^{-8}\,\mathrm{M}_\odot\mathrm{yr}^{-1}$; Townsley & Gänsicke 2009), while for those below the period gap ($P_{\mathrm{orb}} < 2$ hrs) gravitational radiation ($\dot{M} \sim 10^{-10} - 10^{-11}\,\mathrm{M}_\odot\mathrm{yr}^{-1}$; e.g. Warner 1995) seems to be responsible.

Magnetic braking will shrink the orbit of a CV until it "switches off" at an orbital period of ~ 3 hours. The exact cause for the near cessation of magnetic braking is not well understood. Previously, it was suspected that the secondary became fully convective around this point which

[‡]Systems with a larger q are thermally unstable and become other types of accreting WDs, such as supersoft sources (Kahabka & van den Heuvel 1997)

quenches the dynamo that generates magnetic fields (e.g. Copeland et al. 1970; Charbonneau & MacGregor 1997; MacGregor & Charbonneau 1997); however, this is not the generally accepted case anymore and the mechanism is likely more complicated, possibly requiring additional angular momentum loss mechanisms (see the discussion and references in Knigge et al. 2011). Nonetheless, at this stage the mass transfer has driven the secondary out of equilibrium. As the secondary loses mass, there is less matter pressing down on the core and nuclear reactions, which are responsible for the radiation pressure that is balancing out the gravity of the star, decrease. Consequently, the star contracts on the Kelvin-Helmholtz (or thermal) timescale. As the CV evolves, the Kelvin-Helmholtz timescale will eventually be larger than the (magnetic braking driven) mass transfer timescale, resulting in the star having a radius too large for its mass. When magnetic braking switches off, the mass transfer rate is greatly reduced and the secondary is able to regain thermal equilibrium by shrinking to its correct radius, which causes it to detach from its Roche lobe. During this time, the CV continues to evolve (gravitational radiation shrinking the orbit) through the period gap, but is too faint to be seen since the mass transfer is essentially non-existent. At a period ~ 2 hours the secondary regains contact with its Roche lobe and the CV becomes visible again owing to re-established mass transfer (at lower rates that before however, now driven by gravitational radiation).

A few systems can still be found within the gap. These are systems that first achieved Roche lobe contact within the gap (e.g. Davis et al. 2008; Zorotovic et al. 2016), systems with an evolved secondary (e.g. Littlefair et al. 2006; Rebassa-Mansergas et al. 2014) or where the primary has a substantial magnetic field (polars and IPs).

When CVs evolve beyond the period minimum back to longer periods, so called *post-bounce systems*, the mass of the secondary continues to decrease and the orbital period continues to increase. Only a small amount of these systems have been identified (e.g. Howell & Ciardi 2001). Gravitational radiation becomes significantly less effective, mass transfer rates consequently drop drastically and the CV becomes very faint. Eventually the secondary evolves to become a Jupiter-like object that orbits the primary.

Chapter 3

Accretion and Outflows

It has already been mentioned that there is strong observational evidence for the physics of accretion and outflow phenomena being not only coupled, but also seemingly ubiquitous across a vast range of masses of ACOs. To introduce this universality, I discuss some important aspects pertaining to accretion discs in Section 3.1, and jet formation and its link to accretion stages in Section 3.2. Disc-jet coupling across various classes of ACOs is reviewed in Section 3.3. While the association of radio emission with jets is clear in the case of accreting NSs and BHs, this has not been demonstrated for accreting WDs. Therefore, in the final section, Section 3.4, I review the various emission mechanisms that have been proposed for radio detected CVs in the past decade, and also consider some alternative mechanisms that have been put forward in the literature.

3.1 The Accretion Disc

The formation of the accretion disc has already been discussed in Section 2.2.1 and DN outbursts were discussed in Section 2.3.1, describing the mechanism responsible for switching the accretion disc between hot and cool states.

Viscosity plays a critical role in the working of the accretion disc, powering accretion onto the WD by transporting angular momentum outwards through the disc. The physical origin of the viscosity in accretion discs was a topic of debate for some time. The diffuse nature of the material that makes up the disc invalidates the more common origins of viscosity (such as

molecular attraction). Hence, the viscosity (v) has been parameterised as

$$v = \alpha c_s H \tag{3.1}$$

where α is a fraction of the limiting viscosity (a number less than 1, if to ensure subsonic motion), c_s is the speed of sound in the gas and H is the height of the accretion disc. Shakura & Sunyaev (1973) are responsible for the reasoning behind this, arguing that turbulent eddies (smaller than the disc height) are present in the disc in which material is constantly exchanged between neighbouring annuli (more or less at the speed of the constituting molecules i.e. the speed of sound). This alpha parameter can be used in combination with gas equations to construct theoretical accretion disc models, not surprisingly called *alpha-discs*. Alpha-discs are thin ($H \ll R$), have an insignificant mass compared to the WD and are somewhat concave, with the outer edges being thicker than the inner sections. The value of α in the disc of a quiescent dwarf nova is approximately $0.01 - 0.05$, and approximately $0.1 - 0.5$ during outburst.

Balbus-Hawley instabilities (Hawley & Balbus 1991; Balbus & Hawley 1991, 1998), or magnetorotational instabilities, are now the commonly accepted source of viscosity in accretion discs. These instabilities are perfectly compatible with the alpha disc formulation of Shakura & Sunyaev (1973). To establish an understanding of these instabilities, consider a magnetic field line between two masses of ionised material in an accretion disc – the one mass being at a smaller radius than the other. As Keplerian motion dictates, the inner mass will orbit faster than the outer mass, thus stretching the magnetic field line. This results in the outer mass experiencing a positive torque, gaining angular momentum and moving further outwards, while the inner mass loses this angular momentum because of a retarding torque and moves further inwards – consequently, the magnetic field line stretches out even more and the torque becomes even stronger. Consequently, small magnetic fields are greatly amplified and eddies of magnetic turbulence manifest, transporting the majority of the material inwards, but also some material, together with the angular momentum, outwards.

3.2 Jet Formation

Astrophysical jets are collimated bipolar outflows. Evidence for jet launching has been found in all ACOs. While the physics behind the formation of jets is not yet understood, some empirical patterns have emerged.

3.2.1 Radio Observations of Jets

Jets produce synchrotron emission that peak at radio wavelengths (Corbel et al. 2000; Fender 2001). In some cases the jets from XRBs and quasars can be resolved and discrete ejecta or extensions moving away from a central source can be monitored, but more often than not this is not the case. In XRBs, we typically observe two types of relativistic jets: unresolved, steady, self-absorbed, compact jets ($\alpha^* \sim 0$) and transient jets (the launching of discrete ejecta; α goes from inverted to steep). The type of jet is dependent on the system's $\dot{M}$ (Fender et al. 2004a). The steady compact jets occur at low accretion states (or in the spectrally hard state, $\dot{M} < 0.1\,L_{\rm Edd}$[†]) and can persist all the way into quiescence at $< 10^5\,L_{\rm Edd}$ (e.g. Gallo et al. 2005; Plotkin et al. 2013; Plotkin, Gallo, Markoff, Homan, Jonker, Miller-Jones, Russell & Drappeau Plotkin et al.). On the other hand, transient jets are observed when the system transitions between different accretion stages at higher $\dot{M}$'s (e.g. Mirabel & Rodríguez 1994; Hjellming & Rupen 1995; Miller-Jones et al. 2012; Tetarenko et al. 2017; Bright et al. 2020). Additionally, at these higher mass accretion rates, the steady jet can be quenched (e.g. Russell et al. 2011; Coriat et al. 2011; Rushton et al. 2016; Russell et al. 2019).

3.2.2 Accretion Stages

Low-mass XRBs (henceforth simply referred to as XRBs) are typically divided into two groups: transient and persistent sources. This division is equivalent to the split made between DNe and NLs in non-magnetic CVs. This analogy is more than just qualitative, and both the outbursts in transient XRBs and DNe can be explained using the DIM (e.g. Coriat et al. 2012).

Because of the relatively short timescales of XRB outbursts (typically weeks to months), these systems are excellent candidates for studying the relationship between accretion and jets. In depth studies of BH XRB outbursts have revealed that during the course of an outburst, the source goes through different distinguishable states. Substantial effort has been made to map the different stages of outburst in XRBs to accretion states (see Remillard & McClintock (2006) and Belloni (2010) for reviews of XRB accretion states). These states have also been mapped to NS XRBs by Migliari et al. (2004). A useful tool for visualising these states is an X-ray hardness/intensity diagram (e.g. Fender et al. 2004a). X-ray hardness refers to the ratio

[*] For flux density S_ν at some frequency ν, $S_\nu \propto \nu^\alpha$, where α is the spectral index.

[†] The Eddington Luminosity, $L_{\rm Edd}$, is the critical luminosity at which the outward radiation pressure of a celestial body is countered by the inward gravitational force. An increase in the radiation pressure, and thus $L > L_{\rm Edd}$, will result in gravity being overpowered and material being blown away.

of flux/counts in two bands (essentially the equivalent of a colour in optical astronomy). One such diagram is shown in Figure 3.1.

The emission from XRBs in a low accretion state is dominated by non-thermal emission, originating from the inner accretion flow (Yuan & Narayan 2014). A hard X-ray spectrum, that follows a power law with an upper cutoff at $\sim$100 keV, is observed. Additionally, radio emission with a flat or inverted spectral index, believed to be produced by a steady compact jet (Fender 2001), is present in this state. The radio and X-ray luminosities are strongly but non-linearly correlated (Hannikainen et al. 1998; Corbel et al. 2000, 2003; Gallo et al. 2003; Coriat et al. 2011; Corbel et al. 2013; Tetarenko et al. 2016b; Gallo et al. 2018). Strong band-limited noise is observed in this state which gives rise to rapid short-term variability (Belloni et al. 2005). This state is typically referred to as the low/hard state, and probably encompasses the quiescent state of the source. The X-ray:radio correlation has been observed, at least in some cases, in the quiescent state as well (e.g. Gallo et al. 2014; Plotkin et al. 2017; Tremou et al. 2020). In the quiescent state, a disc corona (hot, diffuse material above the plane of the accretion disc) is thought to be responsible for the majority of the luminosity (Esin et al. 1997). On the rise to outburst, the source brightens to $\sim 0.3\,L_{\rm Edd}$, basically moving vertically up the HID, before transitioning to an intermediate hard state.

In the very high/intermediate state, the X-ray spectrum softens, but the steady jet is sustained as it approached the *jet line*. The jet line represents the boundary between states where steady jet formation is present or not. The term 'jet line' can, however, be quite misleading, since there is a range of X-ray intensity and hardness values where any given system can undergo changes in jet behaviour. Nevertheless, as the source evolves towards jet line, the jet velocity greatly increases. The last jet that is launched is the most powerful and is accompanied by a bright transient radio flare. This flare is the result of a powerful transient jet being launched, which produces an internal shock that advances through the material that has previously been expelled (at lower velocities). Prior to this flare, the radio emission becomes more variable and more optically thin, whereas after the radio flare, the radio emission decreases dramatically and has a flat spectrum (Fender et al. 2004a).

After passing through intermediate states, the source enters the high/soft state, characterized by a soft X-ray spectrum that is dominated by optically thick thermal emission from a geometrically thin accretion disc (Shakura & Sunyaev 1976), with a black body temperature $\sim$1 keV. The noise in this state is weak and follows a power law (e.g. Belloni et al. 2005). During the high/soft state, radio emission, and thus likely jet formation, is quenched. Subsequently, the

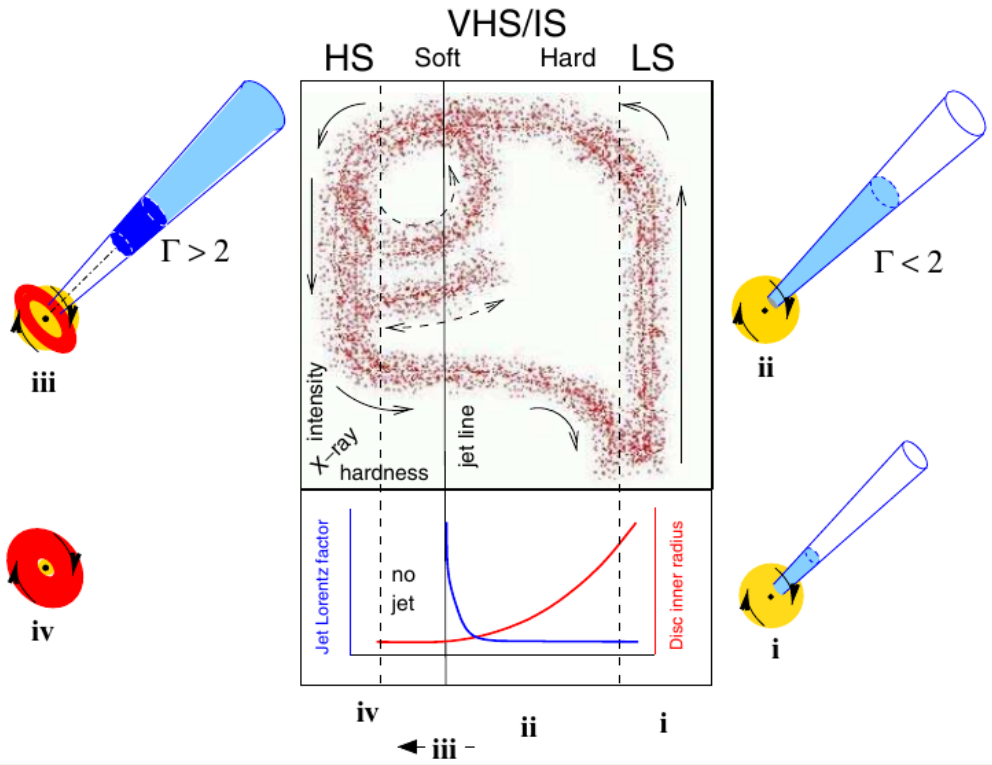

Figure 3.1: Hardness-Intensity Diagram describing a disc-jet coupling model for BH XRBs derived by Fender et al. 2004a. X-ray intensity (increasing upwards) is plotted against X-ray hardness (increasing towards the right). HS, VHS/IS and LS are high/soft state, very high/intermediate state and low/hard state respectively. As the source evolves across the jet line, an internal shock is produced in the collimated outflow and steady jet production halts. The jet is now physically decoupled from the central engine and we observe fading, optically thin radio emission. The diagrams around the plot illustrate the relative contributions of the jet (blue), disc-corona (yellow) and accretion disc (red) at these different stages. For a more in-depth discussion of details in the plot not mentioned here, refer to Fender et al. (2004a).

Source: Fender et al. 2004a, Figure 7

source abruptly returns to the low/hard state, albeit at a luminosity that is smaller than when it transitioned to the soft state ($\sim$0.02 L_{Edd} Maccarone 2003). Some sources are known to move to and fro across the jet line, producing an optically thin radio flare, and ejecta, each time it crosses the jet line from the 'harder' right handside (e.g. Mirabel & Rodríguez 1994; Hjellming & Rupen 1995; Kuulkers et al. 1999; Fender et al. 2004a).

3.3 Universality of Accretion and Jet Formation

The behaviour described in the previous section is our observational picture of accretion and jets in transient BH XRBs. However, the connection between X-ray and radio emission also spans across various classes of BHs. Merloni et al. (2003) examined BHs ranging from Galactic stellar mass BHs to supermassive AGN, and found that the radio luminosity is highly correlated with both the BH mass and X-ray luminosity. Together with the X-ray and radio luminosities, the BH mass forms what is known as *The Fundamental Plane of Black Hole Activity*. Similar work was done by Falcke et al. (2004) that reached analogous conclusions: for BHs across more than 7 orders of magnitude in mass, including XRBs (in the hard and quiescent state) and AGN (LINERS, FR I radio galaxies and BL Lac objects), the radio and X-ray emission non-linearly correlate at a significant level. Heinz & Sunyaev (2003) has derived this non-linear model-independent relation between the observed specific jet flux and BH mass: $F_\nu \sim M^{17/12}$.

Furthermore, disc-jet coupling can also be scaled down to lower mass ACOs. Migliari & Fender (2006) studied the relation between the X-ray and radio emission in NS binary systems and found that they show multiple similarities, as well as some notable differences, to their BH cousins. Qualitatively there are striking similarities: in the hard states, $< 0.01\, L_{Edd}$, steady compact jets are observed in both classes. At higher X-ray luminosities close to the Eddington limit, and specifically during accretion state transitions, transient jets are observed. Furthermore, in the hard state the X-ray and radio luminosities are correlated for both classes, albeit at different power law indices. Quantitatively, there are some significant differences though. NS XRBs are significantly less radio-loud than BH XRBs, and radio emission from NS XRBs has been detected even in the soft states, contrary to the BH systems that exhibit significant quenching of radio emission at these higher accretion rates. The differences between NS and BH XRBs could possibly be attributed to the presence of a boundary layer in NS systems. It is worth noting that the X-ray:radio correlation has only been studied in-depth in three NS

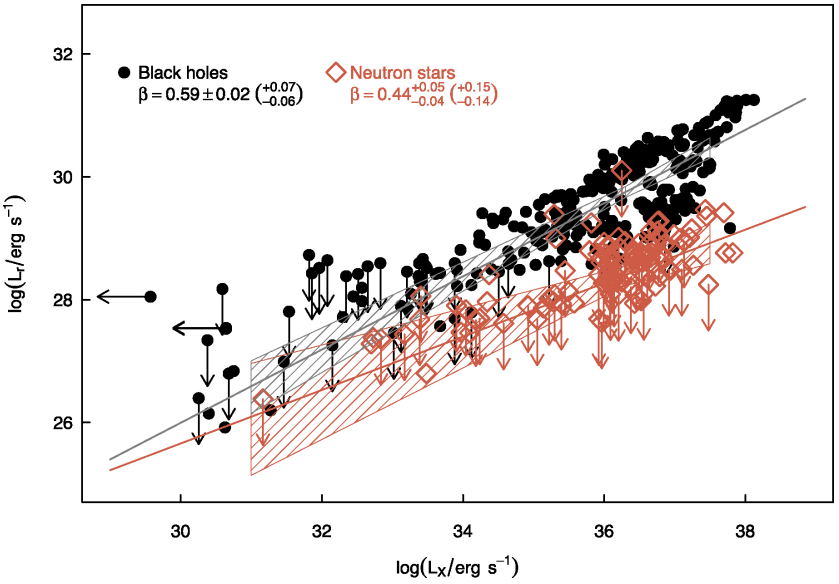

Figure 3.2: 5 GHz radio luminosity plotted against $1-10$ keV X-ray luminosity for 36 BHs (black circles) and 41 NSs (red/orange diamonds) in spectrally hard states. Solid lines represent the median of the "slope" (β, the power law index) posterior distribution, with 3σ errors indicated by the diagonally shaded areas. The values for β are shown in the top right corner, with errors at the $1(3)\sigma$ confidence level.
Source: Gallo et al. (2018), Figure 1

low-mass XRBs: Aql X-1, 4U 172834 and EXO 1745248. For Aql X-1 correlation indices[‡] of 0.40 ±0.07 (Tudose et al. 2009), $0.76^{+0.14}_{-0.15}$ (Tetarenko et al. 2016a) and $1.17^{+0.30}_{-0.21}$ (Gusinskaia et al. 2020) have been found. Migliari et al. (2003) found an index of approximately 1.5±0.2 for 4U 1728-34, while Tetarenko et al. (2016a) fit $1.68^{+0.10}_{-0.09}$ for EXO 1745-248. More recently a 'universal' NS correlation index of $0.44^{+0.05}_{-0.04}$ has been suggested (Gallo et al. 2018). In this same work the authors propose a correlation index of 0.59 ± 0.02 for BHs, which is also consistent with the NS systems within 2.5σ (see Figure 3.2). However, Tudor et al. (2017) has argued more complex behavioral patterns, with different types of NS systems exhibiting disc-jet coupling to varying degrees, and thus no single correlation. The matter is thus still unresolved.

Accreting WDs, too, launch jets. Supersoft X-ray sources (SSS) are WD binary systems with sufficiently large accretion rates to sustain steady nuclear fusion on the surface of the WD (van den Heuvel et al. 1992). SSSs have been reported to launch jets, based on the blue- and red-shifted satellite lines in their optical spectra (e.g. Southwell et al. 1996; Tomov et al. 1998;

[‡]This index refers to the power-law index β, that describes the relation between the radio and X-ray luminosity: $L_{\rm X} \propto L_{\rm R}^{\beta}$

Quaintrell & Fender 1998; Motch Motch). These satellite lines are emission line components produced in the approaching and receding parts of the jet. Jets have also been detected via radio emission (e.g. Taylor et al. 1986; Brocksopp et al. 2004), optical imaging and spectroscopy (e.g. Tomov et al. 2000) and X-ray imaging (e.g. Kellogg et al. 2001) in symbiotic systems – WD binary systems with a red giant companion. Furthermore, jets specifically related to a nova eruption have been observed in symbiotic systems (e.g. RS Ophiuchi, Sokoloski et al. 2008).

More recently, radio observations of DNe have been used to argue that these objects can also launch jets (Körding et al. 2008; Miller-Jones et al. 2011; Russell et al. 2016; Mooley et al. 2017; Fender et al. 2019) and subsequently that non-magentic CVs (i.e. DNe and NLs) are in fact notable sources of radio emission (Coppejans et al. 2015; Coppejans et al. 2016).

By substituting the X-ray intensity with $L_{\rm D}+L_{\rm PL}$ (the sum of disc luminosity and power-law component luminosity) and the X-ray hardness with $L_{\rm PL}/L_{\rm D}+L_{\rm PL}$, a disc-fraction/luminosity diagram (DFLD, Kording et al. 2006) can be plotted. A DFLD for WDs is essentially the equivalent of a HID used for XRBs. Observations of SS Cyg plotted on a DFLD (Figure 3.3) show a similar pattern as outbursts observed in NS and BH XRBs (Körding et al. 2008). One of the main differences between the DNe and BH XRBs, is that that radio emission persists into the soft state, similar to that observed in some NS XRBs. The presence of a boundary layer might have an influence, but there is still no clear understanding of the exact physics. As has been stated in Hameury et al. (2017) and Coppejans & Knigge (2020), one should not over-interpret the similarity of these figures. This is essentially because what has been plotted for SS Cyg, is relating the inner accretion flow and the outer accretion disc. The hysteresis observed here can be explained making use of the DIM alone: the mass transfer in the inner accretion flow varies on the viscous timescale, whereas optical luminosity varies on a shorter timescale. In XRBs, however, the soft and hard X-rays are both produced in the inner accretion flow, and the DIM alone can thus not explain the observed hysteresis.

Nevertheless, in addition to this accretion stage parallelism observed across various classes of ACOs, nearly all accreting jet launching objects (including YSOs, AGN and gamma-ray bursts or GRBs, *but* excluding sources such as NS Z-sources and NLs where radio emission persists into the soft state) exhibit a similar ratio ($\sim 10\%$) of jet power to power liberated by accretion – termed the *jet efficiency* (see Körding et al. 2008 and the references therein). This is highly suggestive of a universal disc-jet coupling mechanism.

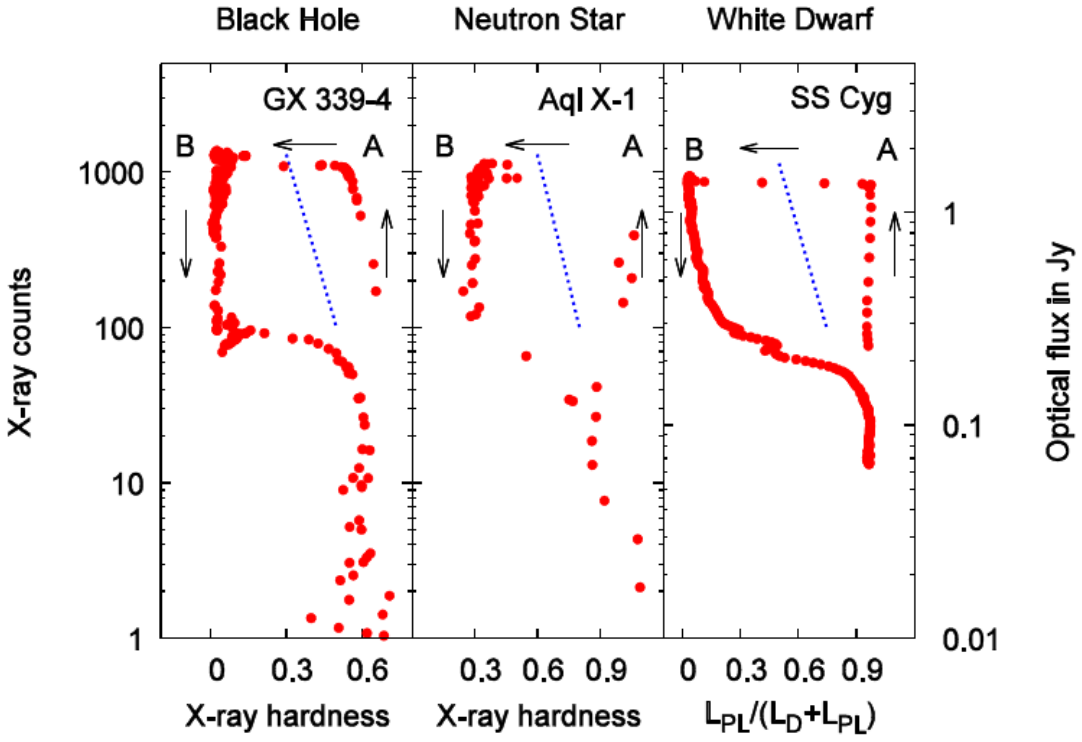

Figure 3.3: HID for a BH and NS XRB compared to the DFLD for a WD. The arrows are indicating how the systems evolves with time. The blue dotted line is the jet line. The X-ray luminosity L_{PL} for SS Cyg is in the 3-18 keV energy range, while for GX 339-4 and Aql X-1, the hardness ratio is defined as the ratio of the counts in the 6.3-10.5 keV range to 3.8–6.3 keV range, and the X-ray counts represent the 3.8–21.2 keV counts of the *Rossi X-ray Timing Explorer*.

Source: Körding et al. 2008, Figure 1

3.4 Radio Emission Mechanisms for CVs

The universality of disc-jet coupling across all classes of ACOs, is heavily reliant on the observed radio emission from non-magnetic CVs being associated with jets. SS Cyg is a DN and by far the non-magnetic CV with the most in-depth studies of radio emission. It has been concluded that said emission is best explained as the result of synchrotron emitting transient jets that launch during a DN outburst (Körding et al. 2008; Miller-Jones et al. 2011; Russell et al. 2016; Mooley et al. 2017; Fender et al. 2019). In other non-magnetic CVs, things are less clear. Coppejans et al. (2016) observed five DNe in outburst with The Karl G. Jansky Very Large Array (VLA) and found that the emission was consistent with both coherent and synchrotron emission. They favoured the latter on account of polarisation levels. For their sample, they found polarisation upper limits of approximately 10% – this is inconsistent with the high levels of polarisation observed from coherent emission. For NLs the matter is even more complicated. The properties of the radio emission observed from three NLs (RW Sex, TT Ari[§] and V603 Aql) by Coppejans et al. (2015) differed significantly between targets and even between epochs of the same target sometimes, suggesting complex or even multiple radio emission mechanism(s) for non-magnetic CVs. While the flux density observed from RW Sex did not show any variability during any epochs, for V603 Aql and TT Ari variability down to a timescale of minutes was observed. The spectral index of the radio emission from the three targets also ranged from -0.5 ± 0.7 to 1.7 ± 0.8. Furthermore, TT Ari alone showed circular polarisation, but none of the targets showed any significant linear polarisation. Coppejans et al. (2015) proposed various radio emission mechanisms, including optically thick and thin synchrotron emission, gyrosynchrotron emission or cyclotron maser emission. For RW Sex they favoured optically thin synchrotron emission (RW Sex showed low levels of circular polarisation and no variability), but all three the aforementioned mechanisms are plausible for V603 Aql. The emission from TT Ari can be explained by gyrosynchrotron emission or cyclotron maser emission (synchrotron emission is ruled out on account of very high levels of circular polarisation). One alternative emission mechanism is flaring behaviour from a secondary. The mechanism was not necessarily favoured though, because the observed radio luminosities were simply much higher than the luminosities observed from flares (e.g. TT Ari's peak luminosity is 38 times higher than the brightest flare in ultracool dwarfs observed by McLean et al. 2012).

To summarise, radio emission has been observed from numerous non-magnetic CVs (and

[§]There is a lot of speculation that TT Ari is in fact a magnetic system.

from different subclasses of non-magnetic CVs). The properties of the emission are not consistent between systems, and sometimes not even between different epochs of the same system. The radio emission is not correlated with any system parameter, subclass or emission at other wavelengths. Various emission mechanisms have been proposed, although in nearly all cases, the emission seems to be consistent with synchrotron emission that can be produced by jets. The important exception here is TT Ari, where a flare with high levels of circular polarisation was observed. This type of emission cannot be explained by a jet. I will now briefly overview the various emission mechanisms that were mentioned above, as well as alternatives that have been proposed in the literature.

3.4.1 Synchrotron Emission (non-thermal)

Synchrotron radiation is a form of magnetobremsstrahlung where the accelerated particles are relativistic (i.e. they have kinetic energies much larger than their rest mass, sometimes this is also called ultrarelativistic). An electron (or any free relativistic particle for that matter) moving in a magnetic field is subjected to the Lorentz force acting perpendicular to both the magnetic field line and the particle's motion, which results in the electron spiralling around the magnetic field line. The electron thus experiences a constant acceleration and consequently emits radiation with power P, described by Larmor's formula

$$P = \frac{2q^2\dot{v}^2}{3c^3} \tag{3.2}$$

where q is the electric charge of the particle, $\dot{v}$ is the acceleration of the particle and c is the speed of light. In Figure 3.4 the orientation of the different force components is illustrated in the left panel, and the resulting spiral motion and synchrotron emission in the right panel.

Synchrotron radio flares can be produced by transient jets. For astrophysical compact jets in XRBs, linear polarisation levels tend to be a few percent (e.g. 2% for GX 339-4, Corbel et al. 2000), although theoretically higher levels are attainable. Additionally, the levels of circular polarisation are usually lower than linear polarisation for synchrotron emission. The spectral index of synchrotron emission varies between $-1.5 \leq \alpha \leq 2.5$, and the emission can thus be optically thin or thick.

The acceleration of non-relativistic charged particles gives rise to either gyro radiation, if $v \ll c$, or cyclotron radiation, if their kinetic energies are comparable to their rest masses. Both types of emission are associated with high levels of circular polarisation (higher than for

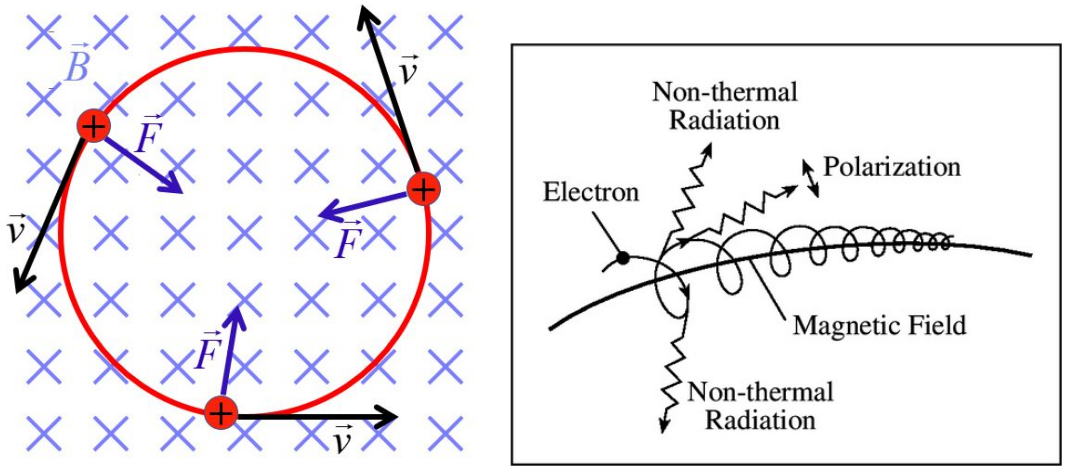

Figure 3.4: **Left:** Three vectors are represented: the magnetic field $\vec{B}$ pointing into the page (light blue crosses), a positively charged red particle with a velocity $\vec{v}$ (in black) perpendicular to $\vec{B}$, and the Lorentz force $\vec{F}$ (in dark blue) pointing radially inward (perpendicular to both $\vec{B}$ and $\vec{v}$), causing the spiral motion. **Right:** As relativistic electrons spiral around magnetic field lines, they emit non-thermal synchrotron radiation. The emission is termed non-thermal because the electron speeds are considered to be too high to be associated with thermal motion at reasonable temperatures.

Source: **Left:** Kathryn Hadley, University of Oregon PHY213 notes **Right:** Professor Kenneth R. Lang, Tufts University, NASA's Cosmos, 2010

synchrotron emission).

3.4.2 Coherent Emission (non-thermal)

In coherent emission, electrons do not radiate independently, instead groups of n electrons (with total group sizes less than a wavelength) act together to emit photons with the same frequency and in phase. The resultant emission can reach extremely high brightness temperatures, with intensities n times higher than incoherent emission. This is because the power radiated by a charge q ($q = ne$ in this case) is proportional to q^2 (see Equation 3.2).

Coherent emission is associated with magnetic interactions close to the WD surface, disc or magnetosphere. It can take the form of line emission, such as with masers, or continuum emission with a steep spectrum, such as observed in pulsars. The model proposed for coherent emission for DNe by Benz & Guedel (1989) predicts high levels of polarisation and irregular outbursts.

3.4.3 Thermal Emission

Thermal emission refers to emission where the emitting particles are in local thermodynamic equilibrium, i.e. the underlying electrons have a Maxwellian velocity distribution. Cordova et al. (1983) has suggested that in some cases the radio emission observed from CVs could be thermal in nature, justified by UV observations of outflows from CVs (e.g. Krautter et al. 1981). Thermal emission has been ruled out in many cases because the size of an emitting region required to produce the observed brightness temperatures is simply unlikely (e.g. Körding et al. 2008; Coppejans et al. 2015). Another eliminating factor would be the observation of short term variability, such as that that has been seen in V603 Aql (Coppejans et al. 2015). The heat transfer in CVs occurs on timescales larger than the observed variability. Coppejans et al. (2015) note that if the emission observed from TT Ari had to be thermal, it would be more consistent with "a thin, dense shell (e.g. of a nova) than an extended, centrally concentrated stellar wind".

The spectral indices associated with optically thin thermal emission are generally between $-1 \leq \alpha \leq -0.5$.

3.4.4 Flaring Secondaries

The secondary stars in CVs are typically K- or M-dwarfs. Isolated low-mass dwarf stars can undergo flare events, supposedly as a result of magnetic fields interacting and recombining in the stellar atmosphere. Gudel et al. (1993) found for a sample of M-dwarf stars, these flare events can give rise to radio emission with a luminosity upper limit $\sim 10^{14}\,\mathrm{erg\,s^{-1}\,Hz^{-1}}$, and Abada-Simon & Aubier (1997) has found that these flares can be circularly polarised as much as 100%. The radio emission in type M0-M6 dwarfs saturates at some rotation rate (McLean et al. 2012), and thus the comparison between isolated M-dwarfs and the tidally locked M-dwarfs in CVs is still valid (Coppejans et al. 2015).

3.4.5 Magnetic CV Emission Mechanisms

In some cases, such as TT Ari and V603 Aql, the properties of the emission are quite similar to that seen in magnetic CVs. In the magnetic systems there is a duality observed in radio emission properties. The emission consists of one component with low levels of polarisation that varies slowly, and another component in the form of sporadic flares with high circular polarisation levels (Coppejans & Knigge 2020). The slow-varying emission has been suggested to be gyrosynchrotron emission produced by electrons in either the WD or red dwarf magnetosphere (Dulk et al. 1983; Chanmugam 1987). The flaring emission is thought to be cyclotron maser emission, originating from close to the WD or red dwarf's surface (Melrose & Dulk 1982).

3.4.6 Cyclotron Masers in the Accretion Stream

An alternative radio emission mechanism for polars has recently been suggested by Kurbatov et al. (2018, 2019). This mechanism is essentially the cyclotron radiation of thermal electrons in a magnetic field that fluctuates as a result of Alfvén wave turbulence.

The authors have noted that there is no fundamental reason why this emission mechanism should not also be valid for IPs or even non-magnetic CVs, and the reason they have pursued it specifically for polars, has to do with the simplified flow morphologies seen in these systems.

3.4.7 Magnetic Reconnections in the Accretion Disc

Finally, the last mechanism that I will mention is that which has been proposed by Meintjes (2016a,b). Magnetic reconnections in the accretion disc can generate non-thermal synchrotron emission, similar to that that has been observed in DNe for example, via the Van der Laan

process. See the works by Meintjes, as well as Coppejans & Knigge (2020) for more in-depth discussions.

Chapter 4

Radio Interferometry

Radio interferometry is a vast field with many concepts beyond the scope of this dissertation. Here I aim to provide an overview of the main concepts encountered in aperture synthesis. Thompson et al. (2017), Taylor et al. (1999) and Molenaar et al. (2017) contain a wealth of information on the subject, ranging from introductory material to some of the most advanced theory, and are the main sources for this chapter. The radio regime spans electromagnetic wavelengths from millimetres to kilometres. A wide bandwidth of the aforementioned wavelengths can penetrate the Earth's atmosphere, and as such ground-based radio astronomy is practical. Furthermore, radio emission is not strongly attenuated by interstellar gas or dust. Radio astronomy has therefore become an important field in observational astronomy.

4.1 The Need for Interferometers

The sky is littered with an abundance of compact radio sources, but due to the relatively long wavelengths, obtaining sufficient angular resolution to resolve these objects is a serious impediment to radio astronomy. The angular resolution θ of a single dish telescope is dependent on the wavelength of observations λ, and the diameter of the telescope, D.

$$\theta \sim \frac{\lambda}{D} \tag{4.1}$$

The Green Bank Telescope is the largest steerable single dish telescope in the world, with a dish diameter of 100 m. A typical observing wavelength in the radio regime is 6 cm; this results in angular resolution of about 2 arcminutes. To obtain an angular resolution of mere arcseconds

at a wavelength of 6 cm, a dish diameter of ∼12 km is required, but the construction of a dish this size is naturally not financially nor technically feasible. It is this need for better angular resolution that has driven the development of radio interferometry. By combining the signals from multiple radio telescopes, it is possible to simulate a dish with an effective radius of the maximum baseline (the distance between 2 individual elements).

4.2 Coordinate Systems

In radio astronomy there are 2 coordinate systems that are often used to simplify equations: the (u, v, w) cartesian coordinate system and the (l, m, n) direction cosine coordinate system.

The baseline components are typically given (in wavelengths) using the aforementioned right-handed (u, v, w)-cartesian coordinate system. w is chosen to be in the direction of the source, normal to the uv-plane, and u and v point towards the east and north respectively. A baseline can be defined as

$$\mathbf{b}_\lambda = \begin{pmatrix} u \\ v \\ w \end{pmatrix} = \frac{1}{\lambda} \begin{pmatrix} \sin H_0 & \cos H_0 & 0 \\ -\sin\delta_0 \cos H_0 & \sin\delta_0 \sin H_0 & \cos\delta_0 \\ \cos\delta_0 \cos H_0 & -\cos\delta_0 \sin H_0 & \sin\delta_0 \end{pmatrix} \begin{pmatrix} X \\ Y \\ Z \end{pmatrix} \tag{4.2}$$

where λ is the center wavelength of the receiving system, H_0 and δ_0 are the hour angle and declination of the phase reference position and X, Y and Z are the coordinate differences for 2 receivers.

The direction cosine coordinate system is usually used to describe positions of objects in the sky. It allows for the fundamental reference point on the celestial sphere to be redefined to some arbitrary location, typically the target being observed and referred to as the *phase center*. The three coordinates that are used are dimensionless direction cosines:

$$l = cos\alpha$$

$$m = cos\beta$$

$$n = cos\theta$$

where α, β and θ are the angles between the u, v and w axes and the vector $\mathbf{s}$ pointing towards the source, respectively.

The physical baseline, projected baseline in the (u, v, w)-space and an observation direction σ in the (l, m, n)-plane are all linked (see Figure 4.1).

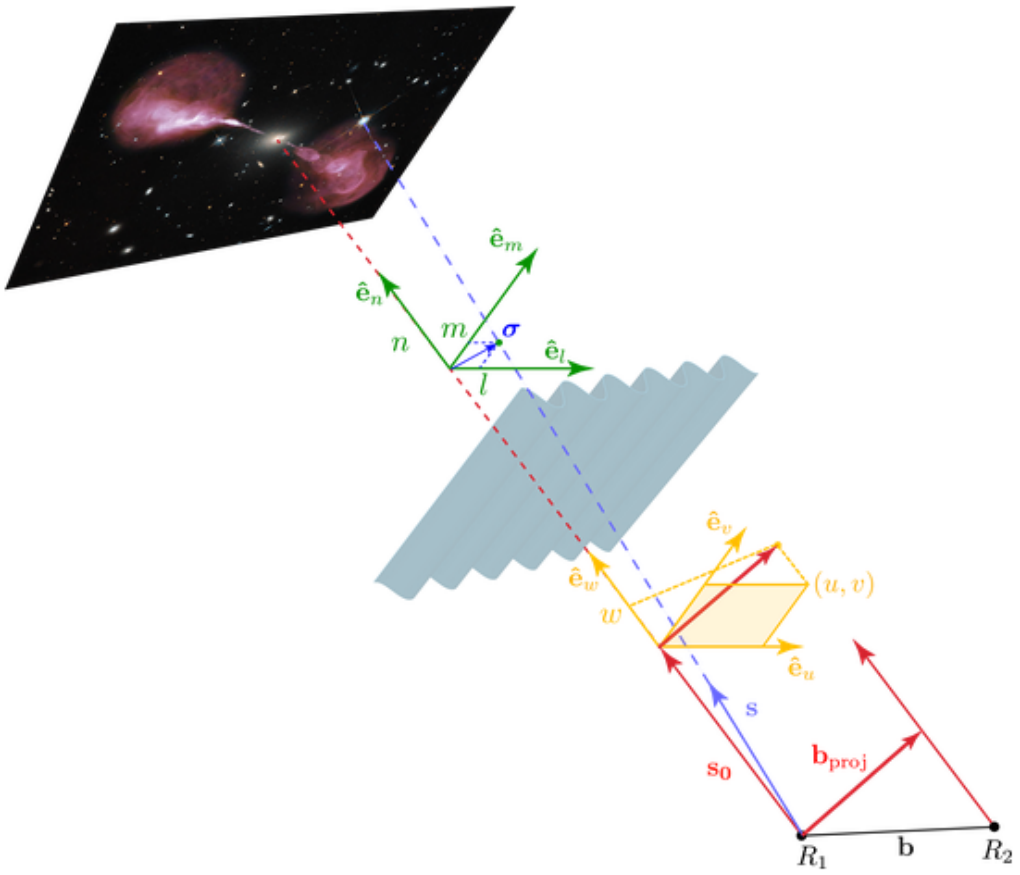

Figure 4.1: $\mathbf{b}$ is the physical baseline between two receivers, R_1 and R_2. $\mathbf{b}_{\text{proj}}$ is the projected baseline in the (u, v, w)-space. $\mathbf{s}_0$ is the phase center and $\mathbf{s}$ is pointing towards the source. σ is the direction of the observation in the (l, m, n)-space.

Source: Molenaar et al. (2017), Chapter 4.3: The Visibility Function

4.3 Interferometers

A radio interferometer typically consists of an array of radio antennas that is used to synthesise a discretely sampled single radio telescope. The different elements in an array all have receivers that convert the electromagnetic waves, originating from astronomical radio sources, into voltages with a phase and amplitude related to the original electromagnetic wave. The voltages from all the individual receivers are then passed to a correlator that multiplies the voltages and takes a time average to reduce the noise levels, essentially producing an interference pattern.

By looking at these values through a spatial filter with baseline-dependent characteristics, a new complex quantity called the *visibility* is derived. As the sky rotates, different baselines will measure different sets of visibilities, which makes up a continuous complex function: *the visibility function*. The *sky brightness distribution* refers to a continuous function that describes all the different sources that the sky consists of. The visibility function is related to the Fourier transform of the sky brightness distribution function.

The goal of interferometry is to reconstruct the sky brightness distribution by sampling the visibility function. These measurements of the visibility function are in the (u, v, w) domain, but are typically projected onto the (u, v) plane. Taking into account the geometry of the baseline and the direction of the source in the sky, a projected baseline (the baseline as seen from the source) can be defined. For every projected baseline there is an associated spatial frequency measurement of the source. As the earth slowly rotates, the projected baseline's geometry slowly changes, tracing out elliptical tracks in the uv-plane (see Figure 4.2). More array elements, and thus more baselines, mean better uv-coverage, and thus better sampling of the visibility function, which translates to more comprehensive information of the complex visibility amplitude and phase, and ultimately the flux and position of the source.

There are a number of ways to improve uv-coverage. Firstly, by increasing the number of antennas and optimising their distribution, the instantaneous snapshot uv-coverage can be improved. Secondly, due to the Earth's rotation, time integration will naturally trace uv-tracks and improve coverage. Thirdly, by making use of broadband receivers to observe in a larger bandwidth, uv-coverage can be improved radially (see Figure 4.3).

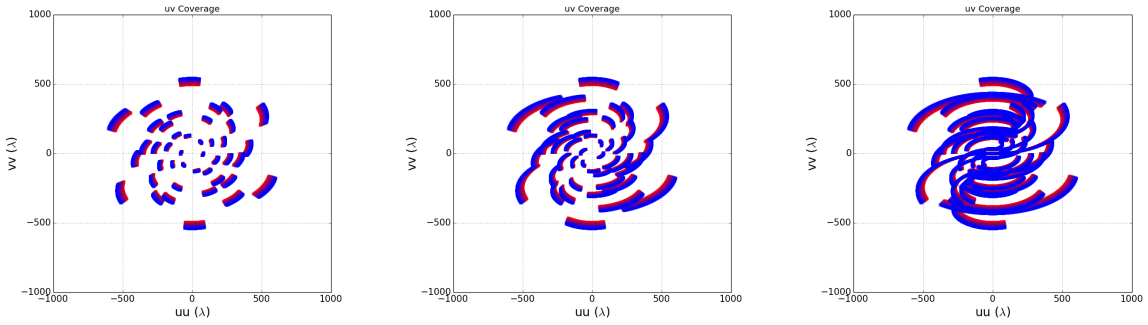

Figure 4.2: *uv*-coverage for the KAT-7 telescope with a 100 MHz bandwidth, observing a field at -30 declination for different observation periods.

Source: Molenaar et al. (2017), Chapter 5.2: Sampling and Point Spread Functions

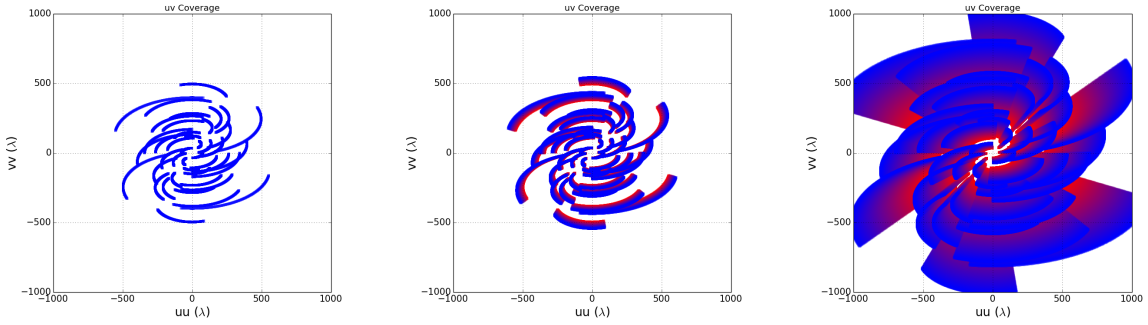

Figure 4.3: *uv*-coverage for the KAT-7 telescope observing a field at -30 declination for 6 hrs with different bandwidths.

Source: Molenaar et al. (2017), Chapter 5.2: Sampling and Point Spread Functions

4.4 The Relation between Sky Brightness and Visibility

To link the visibility function to the sky brightness distribution, the Van Cittert-Zernike Theorem is implemented. This requires a number of Fourier approximations to be made, listed below.

- Different parts of the sky are assumed to be mutually incoherent, or in other words statistically independent of one another.
- Sources are assumed to be infinitely far away.
- The propagation medium of the observed signal is assumed to be homogeneous so that no propagation effects can occur.
- A relatively small field of view is assumed, since in practice antennas are not isotropic.
- As a result of previous approximations, incoherent emission is received close to the phase center. This allows for the w term to be ignored and the baselines to be approximated as coplanar.
- The correlator is assumed to make use of a narrow bandwidth for the correlation operations.
- The sampling of the visibility function is assumed to be continuous.

The above approximations permit the Van Cittert-Zernike Theorem to be invoked. This theorem states that the visibility function with a baseline ab is the 2-dimensional Fourier transform of the sky brightness intensity distribution, given a monochromatic and incoherent intensity distribution I_V. Or in mathematical terms:

$$V_{ab}(u,v,0) = \int_{-\infty}^{\infty}\int_{-\infty}^{\infty} I_V e^{-2i\pi(ul+vm)} dldm \tag{4.3}$$

4.5 The Sampling and Point Spread Functions

Having established this, aperture synthesis can now be discussed. This is the process whereby an image is produced from the measured visibilities. One way of interpreting the above relation is to imagine the sky distribution as being made up of numerous unresolved delta functions (radio 'point sources'). Each delta function in the image domain is a complex sinusoidal wave in the

visibility domain. Consequently a point source in the image domain can be detected even if the visibility domain is not fully sampled.

The visibility space is sampled by a function which is dependent on the interferometric array configuration. The Fourier transform of this visibility sampling function is the *Point Spread Function* (PSF). The PSF (previously referred to as the synthesised beam and sometimes called the dirty beam) describes the response of a measurement to an ideal point source. The signal that is observed by an interferometer is thus the convolution of the true signal with the PSF. The PSF of a circular sampling function is an Airy disc. The central spot is referred to as the PSF primary lobe and the concentric rings are the PSF sidelobes.

4.6 Gridding

In practice the sampling function is not continuous and the visibility domain is irregularly sampled, as a result of baselines being sampled temporally rather than spatially. A standard Direct Fourier Transform (DFT) can be used to construct an image from these non-uniform samples, but this is computationally expensive. Instead the visibility samples are resampled onto a grid during a process called *gridding*, in which case a Fast Fourier Transform (FFT) can then be utilised to construct an image from the uniform samples. Given N^2 pixels and M (where $M \approx N^2$) visibilities, an FFT takes $\sim 2N^2\log(\mathrm{N})$ computational steps, compared to MN^2 steps required for a DFT.

The inverse of the gridding process is called *degridding* in which regularly sampled visibilities are interpolated back to the *uv*-plane. This is necessary because some deconvolution algorithms (e.g. Cotton-Schwab) require the non-uniform irregular samples.

4.7 The Dirty Image

All the necessary background information has now been given to understand the production of the initial image, called the *dirty image*. The dirty image is approximately (since the Van Cittert-Zernike Theorem has been used to convert the 3-dimensional visibility domain to a 2-dimensional domain) described as

$$I^D(l,m) \approx \int_{-\infty}^{\infty}\int_{-\infty}^{\infty} S(u,v)V_{obs}(u,v)e^{-2\pi i(ul+vm)}dudv \tag{4.4}$$

where I^D is the dirty image, $S(u,v)$ is the sampling function and V_{obs} is the observed visibilities. The sampling function consists largely of the uv-track coverage, but also contains the gridding operator and some weighting function. The above equation can be rewritten to show that the dirty image is the Fourier transform of the sampled visibilities, which by Fourier theory is the convolution of the Fourier transform of the sampling function (or the PSF) with the Fourier transform of the observed visibilities (which is the true image).

$$I^{\mathrm{D}} = \mathscr{F}\{SV_{\mathrm{obs}}\} = \mathscr{F}\{S\} \circ \mathscr{F}\{V_{\mathrm{obs}}\} = PSF \circ I^{\mathrm{true}} \tag{4.5}$$

4.8 Image Weighting

The sampling function is not necessarily a binary function where a visibility pixel is assigned a value of 1 or 0 based on whether a baseline trajectory measured that specific location or not. In some cases a pixel might have been measured by multiple baselines and/or multiple times, resulting in better sensitivity than a pixel that merely has one measurement. It is also possible that some baselines have better sensitivity than others, e.g. in Very Long Baseline Interferometry (VLBI). In such cases, the former pixel would have to be given a larger weight than the latter. This is incorporated through the use of a weighting function. The weighting function W is a product of a measurement reliability function R, a taper weight function T, a density weight function D and the sampling function S.

$$W = R \cdot T \cdot D \cdot S \tag{4.6}$$

The density weighting function (often what is simply referred to as the weighting function) assigns weights to individual pixels based on the number of times it was sampled. *Natural weighting* (essentially a Gaussian weighting function) maximises sensitivity at the cost of angular resolution. *Uniform weighting* (essentially a boxcar weighting function) produces a higher resolution image, with decreased sensitivity. A third possible weighting scheme (and probably the most used) was developed by Daniel Briggs (Briggs 1995) and is hence called *Briggs weighting* (or robust weighting). Briggs represented the aforementioned two weighting schemes as the ends of a spectrum (with uniform weighting at -2 and natural weighting at 2), with a robustness

parameter $\mathcal{R}$ (not to be confused with the measurement reliability function) controlling the balance between sensitivity and resolution. Thus if the value is more negative the weighting is more uniform, and if the value is more positive then the weighting is more natural. Depending on the scientific goal, a value for $\mathcal{R}$ can be chosen to either increase the sensitivity or the resolution (at the cost of the other).

A taper function is the 3-dimensional equivalent of a window function. It is used to filter out a specific range of spatial frequency scales. The signal to noise can be maximised by implementing a taper function if the size of a source is already known.

The measurement reliability function is used to factor in the differences between individual array elements (e.g. the different system temperatures or sensitivities of antennas) during the course of an observation. A priori array-intrinsic information such as expected technical figures can also be included into this function.

4.9 Deconvolution

Irregular sampling of the visibilities leads to bright sources in a dirty image having PSF-sidelobes that might be masking fainter sources. Deconvolution is the process of deconvolving the PSF from the dirty image, to recover the true sky. Or in other words removing the instrumental effects from the dirty image to obtain an image that more accurately represents the true sky flux.

Deconvolution requires a sky model. The sky model is built iteratively by subtracting sources from the dirty image and then adding them to the model. The signal that remains in the dirty image after subtraction of the sources is the residual flux. The sky model is convolved with an ideal PSF, and then the residuals are added to create a restored image.

The standard deconvolution algorithm used in radio interferometry is CLEAN, and a simple version of CLEAN is the Högbom-method (Högbom 1974). The first step is to make a copy of the dirty image, called the residual image. The algorithm then finds the position and value of the pixel with the maximum flux in the residual image, and subtracts the product of some gain factor, the PSF and the peak pixel value from the residual image at the relevant position. The value and position of this source is then added to an empty image to build up the sky model. This procedure is repeated either for a set number of iterations or until some defined threshold (such as a noise-limit) is attained. The built-up sky model is convolved with the PSF (the restoring beam) and finally the residuals are added to this newly constructed image again

to produce the final CLEAN image.

The Högbom method is an image domain implementation of CLEAN. A gridded visibility domain implementation of CLEAN has been developed, and is called Clark's method (Clark 1980). The dominant method used today however, is the Cotton-Schwab method (Schwab 1984). It is based on Clark's method, but can perform the convolution on ungridded visibilities at the cost of being more computationally expensive.

4.10 The RIME

The RIME (Radio Interferometric Measurement Equation; Hamaker et al. 1996; Hamaker 2000) models all the propagation and instrumental effects using Jones matrices, to describe the changes that the original electromagnetic signal undergoes to become the measured signal. Jones matrices are functions of time and frequency.

The analogue electronic components are responsible for the majority of direction independent effects (DIE). These are all absorbed into the instrumental gain matrix, **G**-Jones matrix. This describes the complex gain of a dual element receiver and contains both a frequency- and time-dependent component. Intrinsically, gain refers to the time-variable, frequency-independent component. The **B**-Jones matrix describes the bandpass gain which is the frequency dependent component of the complex gain that only varies very slowly with time and is also a DIE. The signal from antenna-feeds that measure radiation components in different polarisation states, can leak from one feed to another. Yet again, this is a DIE, called polarisation leakage, and is represented by the **D**-Jones Matrix.

The most important direction dependent effect (DDE) is the primary beam of an antenna, i.e. the direction dependent gain of the antenna corresponding to the $\mathbf{E}_{\mathrm{PB}}$-Jones matrix. The **P**-Jones matrix is used to incorporate direction dependent parallactic angle effects. The parallactic angle is the spherical angle between the greater circle going through the source and the zenith, and the greater circle going through the source and north celestial pole.

4.11 Calibration

A series of calibration efforts need to be employed to radio observations in order to achieve data that are of scientific value. Calibration procedures can involve first, second and third generation calibration (1GC, 2GC and 3GC).

First generation calibration is performed by utilising observations of well-studied calibrator objects. These calibrators are observed in between observations of a target to record any parametric changes over the course of the observation. Through interpolation and solving gain solutions, major visibility errors are rectified. Usually two calibrators (a primary bandpass/flux calibrator and a secondary amplitude/phase calibrator) are used to calibrate four quantities: absolute flux (to calculate true fluxes), the bandpass (to rectify frequency axis errors), phase delays and the complex gains. A typical observation scheme would observe the primary calibrator at the beginning of the observation and then alternate between the secondary calibrator and the target field. Generally the primary calibrator, which is a very bright, invariant, point-like source, is used to calibrate the first three quantities mentioned. The secondary calibrator needs to be as close as possible to the source, so that it will be subjected to the same local effects, and is used to determine the last mentioned quantity. Calibration can either be treated as a least squares problem or by calculating closure quantities. The method of calculating closure quantities makes use of a triple interferometer system to calculate the phase and amplitude of small angle visibilities (Jennison 1958). Solutions are transferred to the target via interpolation or curve fitting.

Second generation calibration constitutes direction-independent self calibration. In self calibration an incomplete sky model is used to calibrate the observed visibilities, which are then deconvolved to create an image. The sky model is improved by using a source finder on the constructed image, and this improved sky model is then again employed for calibration. The procedure is repeated until some threshold is reached or the improvement is insignificant.

Advances in radio telescopes have made improved specifications such as a larger field of view possible, greatly contributing to scientific efficiency but introducing more errors as well — hence the need for third generation (direction dependent self) calibration. DDEs can be modelled by adding a priori information on the source to the primary beam Jones matrix, or if this knowledge is not available, by adding source-dependent differential gain factors.

4.12 Sensitivity and Noise

In radio astronomy it is common to use a temperature (T) to express the noise power of radio elements

$$T = \frac{P}{k_B \Delta\nu} \tag{4.7}$$

where P is the signal power, k_B is the Boltzmann constant and $\Delta\nu$ is the bandwidth of the signal. The *system temperature* (T_{sys}) defines the total noise. It consists of multiple components such as the random sky noise (which includes the Cosmic Microwave Background), noise from the atmosphere (mostly the ionosphere), spillover noise resulting from the black body radiation of the earth if the telescope is pointed close to the horison (and thus a DDE) and the receiver noise.

The *System Equivalent Flux Density* (SEFD) is a commonly used measurement of the sensitivity of a radio telescope. It is defined as the ratio of the system temperature to the effective gain.

4.13 Radio Frequency Interference

Radio Frequency Interference (RFI) refers to artificial radio signals that degrade the measured sky signal. RFI is classified as either narrow-band or broadband, depending on whether the interference stretches over only a few frequency channels or the majority of the spectral window being observed, respectively. Standard sources of RFI include FM (frequency modulation) radio (89-110 MHz) and GSM (Global System for Mobile Communications) at around 850 MHz and 1.9 GHz. Frequencies of paramount importance to astronomy, such as 1.4 GHz, are protected by regulation. Methods of dealing with RFI include introducing notch filters, employing RFI flagging software and establishing a radio quiet zone in the vicinity of the radio observatory.

Most radio telescopes and interferometers produce data sets that contain at least some data that needs to be flagged – faulty electronics and antennas and RFI being the major culprits. Flagging is an important step of the reduction process where data that are corrupted are marked and essentially excluded from further processing. While it is possible (albeit tedious and time-consuming) to manually flag a radio data set, for interferometers the size of MeerKAT tackling this process manually becomes unrealistic. Instead algorithms that automatically detect and flag data are employed.

Chapter 5

A Survey of Nearby Novalikes

The targets for this radio survey of accreting white dwarfs are eleven nearby, southern NLs with measured orbital periods. Each system was observed with MeerKAT, as part of ThunderKAT (The Hunt for Dynamic and Explosive Radio Transients with MeerKAT; Fender et al. 2017). ThunderKAT is MeerKAT's LSP (large survey project) to discover and image explosive radio transients in the image domain. Within ThunderKAT there are various subgroups: Commensal Searches, Cosmic Explosions, CVs and XRBs. This work forms part of the CV subgroup. Based on the outcome of this initial census of NLs, decisions regarding future directives for ThunderKAT will made, possibly to push the distance limit further with the eye on radio data on a comprehensive sample of nearby DNe and NLs. This goal is beyond the scope of this dissertation, however.

Additionally, after the initial snapshot survey of eleven NLs to determine which systems can be detected, plans were made to do follow-up observations of the two systems that showed the largest signal-to-noise ratio. These follow-up observations would be concurrent with optical, UV, X-ray, and (for V603 Aql) higher-frequency radio observations.

Furthermore, there is some uncertainty regarding the orbital period of V5662 Sgr, as will be mentioned in Section 5.2.4. Time-resolved spectroscopic observations of this system, as well another little-studied system LSIV -08 3, were obtained making use of the SAAO 1.9 m telescope in Sutherland, South Africa.

In Section 5.1 I describe how this sample has been defined. In Section 5.2, I briefly overview each system, in order of increasing distance, focusing on the most important features and most relevant history. All MeerKAT observations are discussed and presented in Section 5.3.1. The

details with regard to the follow-up multi-wavelength observations are discussed in Section 5.3.2. The time-resolved optical spectroscopy is presented in Section 5.3.3.

5.1 Defining the Sample

The original catalogue consisted of $\sim$ 8000 objects (as of April 2018), including both known CVs, as well as CV candidates, compiled from various sources, including transient surveys and ATels *. This catalogue was made available by E. Breedt, through private communication. Four selection criteria were implemented for the sample: systems classified as NLs, systems with known orbital periods, systems with *Gaia* DR2 distance < 350 pc and systems with declinations $< +10°$.

The most restricting selection criterion was the confirmed novalike classification (2.7% of the catalogue). For these NLs, the most restricting criterion was the distance-limit (14.6% of the NLs), followed by the declination constraint (51.9% of the nearby NLs). Finally, 78.6% of the nearby, southern NLs had measured orbital periods. Applying these criteria resulted in eleven systems. In Table 5.1 the optical coordinates, distance estimates, orbital periods and detected V-band magnitude ranges of the targets are given. This sample includes a few systems that have not been very well studied. It is possible that, with long-term photometric monitoring, one or two may turn out to be DNe.

5.2 Properties of the Targets

Brief overviews of each of the eleven targets of this NL survey follow, with an emphasis on systems parameters, previous radio observations and any unique or unusual features. The sample contains various subclasses of NL, including UX UMa and SW Sex types, but none are known to be VY Scl stars that show deep low-states ('anti-DN outbursts').

5.2.1 IX Vel

IX Vel is the brightest CV in the night sky. It was discovered during a survey of OB stars, designated CPD -48 1577 (Garrison et al. 1977), but only later on properly classified as a CV (Garrison et al. 1982). An extensive study (Beuermann & Thomas 1990) yielded numerous system parameters, including $M_1 = 0.80^{+0.16}_{-0.11}\,\mathrm{M}_\odot$ and $M_2 = 0.52^{+0.10}_{-0.07}\,\mathrm{M}_\odot$. Masses were derived

*Astronomer's Telegram: http://www.astronomerstelegram.org

Table 5.1: Optical coordinates, distances, orbital periods, and observed V-band magnitude ranges for the NLs in this sample. The coordinates and distance measurements are from *Gaia* DR2 (Gaia Collaboration et al. 2016, 2018; Luri et al. 2018), and the magnitude ranges from The International Variable Star Index (VSX).

Target name	RA (J2000)	Dec (J2000)	Distance (pc)	Orbital period (days)	V-band magnitude range	Absolute magnitude range	Orbital period reference
IX Vel	$08^h15^m19.0^s$	-49°13′20.7″	90.6 ± 0.2	0.193929(2)	9.1 – 10.0	4.3 – 5.2	Beuermann & Thomas (1990)
V3885 Sgr	$19^h47^m40.5^s$	-42°00′26.4″	132.7 ± 1.4	0.20716071(22)	10.3 – 10.5	4.7 – 4.9	Ribeiro & Diaz (2007)
V341 Ara	$16^h57^m41.5^s$	-63°12′38.4″	156.1 ± 2.0	0.15216(2)	10.4 – 12.5	4.4 – 6.5	Bond & Miszalski (2018)
V5662 Sgr	$20^h05^m51.2^s$	-29°34′58.0″	168.6 ± 5.2	0.062887(37)	15.4 – 18.0	9.3 – 11.9	Tappert et al. (2004)
IM Eri	$04^h24^m41.1^s$	-20°07′11.8″	191.2 ± 1.4	0.1456348(4)	11.1 – 13.3	4.7 – 6.9	Armstrong et al. (2013)
LS IV -08 3	$16^h56^m29.6^s$	-08°34′38.7″	211.0 ± 2.8	0.1952894(10)	11.3 – 11.6	4.7 – 5.0	Stark et al. (2008)
RW Sex	$10^h19^m56.4^s$	-08°41′56.1″	236.5 ± 5.0	0.24507(20)	10.4 – 10.8	3.5 – 3.9	Beuermann et al. (1992)
UU Aqr	$22^h09^m05.8^s$	-03°46′17.7″	255.9 ± 5.1	0.1638049430	12.9 – 15.5	5.9 – 8.5	Baptista & Bortoletto (2008)
V347 Pup	$06^h10^m33.7^s$	-48°44′25.4″	295.8 ± 1.4	0.231936060(6)	13.4 – 15.8	6.0 – 8.4	Thoroughgood et al. (2005)
V603 Aql	$18^h48^m54.6^s$	00°35′02.9″	313.4 ± 6.7	0.1382009(4)	-0.5* – 12.7	-8.0* – 5.2	Peters & Thorstensen (2006)
CM Phe	$00^h21^m33.2^s$	-51°42′34.6″	315.1 ± 3.8	0.2689(7)	14.8 – 15.8	7.3 – 8.3	Hoard et al. (2001)

Notes: *The nova eruption of 1918

making use of a geometric and kinematic model of the spectral lines that are created as a result of irradiation. Linnell et al. (2007) derived a mass transfer rate of $\dot{M} = 5 \times 10^{-9}\,\mathrm{M}_{\odot}\,\mathrm{yr}^{-1}$ and an inclination of $i = 57^{\circ} \pm 2^{\circ}$. Ultraviolet spectra of IX Vel show a P Cygni profile features associated with wind outflows of $3000\,\mathrm{km\,s}^{-1}$(e.g. Sion 1985).

IX Vel was observed in 2008 in the radio regime, using the Australian Telescope Compact Array (ATCA) in its 6A configuration, with a maximum baseline of 6 km. Due to a nearby bright and confusing source, noise levels were too high to yield anything other than an upper limit of 0.6 mJy (Körding et al. 2011).

5.2.2 V3885 Sgr

V3885 Sgr is the first NL in which spiral structure in the accretion disc was detected via Doppler tomography (Hartley et al. 2005). Hartley et al. also constrained the mass ratio to $q = M_2/M1 \gtrsim 0.7$, proposing mass limits for the primary $0.55\,\mathrm{M}_{\odot} < M_1 < 0.80\,\mathrm{M}_{\odot}$ and an inclination $i > 65^{\circ}$. These mass constraints are confirmed by Ribeiro & Diaz (2007), who also estimated the inclination to be within the interval $45^{\circ} < i < 75^{\circ}$. A mass transfer rate of $\dot{M} = (5.0 \pm 2.0) \times 10^{-9}\mathrm{M}_{\odot}\,\mathrm{yr}^{-1}$ in combination with parameter values that fall within the above mentioned ranges can reproduce the observed spectrum of V3885 Sgr (Linnell et al. 2009).

V3885 Sgr has been observed using ATCA in 2008 and again in 2010 (Körding et al. 2011). In 2008 it was detected at 4.4σ with a flux density of $0.12 \pm 0.03\,\mathrm{mJy\,beam}^{-1}$ at 4.8 GHz and 4.9 GHz. The 2010 observations detected the source at 5.5 GHz (17σ with a primary beam size $3.14'' \times 2.32''$) and 9 GHz (7σ with a primary beam size $2.1'' \times 1.4''$) with flux densities of $0.16 \pm 0.01\,\mathrm{mJy\,beam}^{-1}$ and $0.11 \pm 0.02\,\mathrm{mJy\,beam}^{-1}$ respectively.

5.2.3 V341 Ara

The relatively poorly studied V341 Ara is a NL system surrounded by both a faint Hα nebula, designated Fr 2-11 (Frew 2008), as well as a bow shock nebula (Bond & Miszalski 2018). Originally identified as CPD -69°4037 (and then HV 2969), V341 Ara was discovered by Henrietta Leavitt at the Harvard College Observatory (Pickering 1907). Follow-up studies led astronomers to believe the object is Cepheid variable (e.g. Hoffmeister 1956). Kiraga (2012) suggested that the system is in fact a cataclysmic variable. D. Frew discovered the Hα nebula during a search for planetary nebulae. In addition to the larger Hα emission nebula, follow-up observations showed a bow shock nebula surrounding the star and yielded a period of 0.15216(2) days (Bond

& Miszalski 2018) – making this system remarkably similar to BZ Cam, another CV inside a bow shock nebula with a very similar period. A recent multi-wavelength campaign has established various fundamental properties (Castro-Segura et al., in preparation), amongst others adopting a relatively low inclination ($i \approx 30°$) based on absorption features in previously observed spectra. There are no reported radio observations of V341 Ara in the literature.

5.2.4 V5662 Sgr

V5662 Sgr is the least studied object in this list of targets. It was discovered in the Calán-Tololo Survey, identified as a candidate CV and confirmed as a definite CV by follow-up observations (Tappert et al. 2002). The most probable orbital period of the system (designated CTCV J2005-2934) is 0.062887(37) days (Tappert et al. 2004) based on photometric data, but the authors note that additional observations are required to confirm this very short orbital period. The light curve obtained by Tappert et al. (2004) for this object displayed one small and one large hump and spectroscopic observations showed an unusually strong Hα emission line. These authors also suggested that this system may be a DN in which outbursts have been missed. V5662 Sgr was designated its name in The 80th Name-List of Variable Stars (Kazarovets et al. 2013). No observations of V5662 Sgr at radio wavelengths have been reported.

5.2.5 IM Eri

IM Eri was one of fifteen cataclysmic variables discovered by Chen et al. (2001) in the Edinburgh-Cape Blue Object Survey. The system (referred to as EC 04224-2014) was classified as a non-eclipsing NL system, showing spectral features that changed from broad emission features in a faint state to broad absorption features when in a bright state. Blue-shifted absorption of He I 5876, commonly associated with strong wind outflows, has been detected by Armstrong et al. (2013). Armstrong et al. additionally identified an orbital frequency at 6.86649(2) c day^{-1}, a negative superhump frequency at 7.226(1) c day^{-1} and superorbital frequency at 0.354(7) c day^{-1}. The presence of both super- and sub-orbital frequencies suggests an accretion disc tilted with respect to the orbital plane.

There are no accounts of radio observations of IM Eri in the literature up to date.

5.2.6 LS IV -08 3

LS IV-08°3 is a bright system, initially misclassified, first as an OB star (Nassau & Stephenson 1963) and then as a hot subdwarf (Kilkenny & Busse 1992). Stark et al. (2008) gives substantial spectroscopic evidence for the system's reclassification as a UX UMa type NL.

There have been no reported observations of LS IV -08 3 in the radio regime.

5.2.7 RW Sex

RW Sex is a well-studied non-eclipsing NL and one of the brightest CVs in the night sky. A mass ratio of $q = 0.74 \pm 0.10$ and a system inclination between $28° < i < 40°$ has been derived by Beuermann et al. (1992). Linnell et al. (2010) estimated a mass transfer rate of $\dot{M} \sim 5 \times 10^{-9}\,\mathrm{M_\odot\,yr^{-1}}$.

Making use of a skew mapping technique, the spectrum of the secondary star is best fitted by that of a K5 dwarf (Vande Putte et al. 2003). No optical features associated with collimated outflows have been found down to an equivalent width of $\sim 0.015\,$Å (Hillwig et al. 2004), but there is evidence for a significant disc wind ($\sim$4550 $\mathrm{km\,s^{-1}}$) in the system (e.g. Prinja & Rosen 1995).

RW Sex has previously been observed at radio wavelengths by Cordova et al. (1983) and Coppejans et al. (2015). Cordova et al. observed, but did not detect, RW Sex with the VLA at 4.885 GHz with a 50 MHz bandwidth. An upper-limit of 0.15 mJy is given. Coppejans et al. observed RW Sex in two epochs in the C-band, with the pre-upgrade VLA in the A configuration and with a 4 GHz bandwidth. They detected RW Sex in both epochs with peak flux densities of 33.6 $\mu\mathrm{Jy\,beam^{-1}}$ (RMS 3.7 $\mu\mathrm{Jy\,beam^{-1}}$) and 26.8 $\mu\mathrm{Jy\,beam^{-1}}$ (RMS 3.3 $\mu\mathrm{Jy\,beam^{-1}}$) and beam sizes of $0.58'' \times 0.33''$ and $0.56'' \times 0.33''$ respectively. A spectral index $\alpha = -0.5 \pm 0.7$ was derived and no variability was observed over the $\sim$ 20 min observation. They propose gyrosynchrotron emission, cyclotron maser emission and optically thin synchrotron emission as possible emission mechanisms, favouring the last.

5.2.8 UU Aqr

UU Aqr is an eclipsing system, first correctly classified as a CV by Volkov et al. (1986). A thorough study by Baptista et al. (1994) yielded many system parameters, including a mass ratio $q = 0.30 \pm 0.07$, $M_1 = 0.67 \pm 0.14\,\mathrm{M_\odot}$, $M_2 = 0.20 \pm 0.07\,\mathrm{M_\odot}$, an inclination $i = 78° \pm 2°$ and a K7-M0 spectral type for the secondary. Baptista et al. (1996) estimate $\dot{M} = 10^{-9.0 \pm 0.2}\,\mathrm{M_\odot\,yr^{-1}}$.

UU Aqr displays various forms of variability, ranging from flickering and 'stunted' DN oubursts that cause short-term variability (of up to a magnitude) on a timescale of days (Honeycutt et al. 1998) to long-term variability (≈0.3 mag) on a timescale of years (Baptista et al. 1994). Additionally, bright flares (that can constitute up to a quarter of the total system brightness) were reported by Baptista et al. (1994). The principal source of flickering in UU Aqr is explained as spiral shocks in the outer accretion disc induced by tidal interactions from the secondary (Baptista & Bortoletto 2008).

No observations of UU Aqr in the radio regime have been reported.

5.2.9 V347 Pup

Originally referred to as LB 1800, V347 Puppis was classified as an eclipsing NL system by Buckley et al. (1990). Buckley et al. noted that this system might be an intermediate polar, partly due to the large $L_{\mathrm{X}}/L_{\mathrm{opt}}$ ratio, and that this will have to be resolved by searching for coherent optical pulsations. None have been found to date, and there is no strong evidence in the literature that this system is magnetic. Multiple system parameters for V347 Pup were obtained by Thoroughgood et al. (2005): a mass ratio $q = 0.83 \pm 0.05$, $M_1 = 0.63 \pm 0.04\,\mathrm{M}_\odot$, $M_2 = 0.52 \pm 0.06\,\mathrm{M}_\odot$, inclination $i = 84°.0 \pm 2°.3$ and a M0.5V spectral type for the secondary. Thoroughgood et al. also confirmed the presence of spiral structure in the accretion disc first reported by Still et al. (1998). The literature contains no reports of radio observations of V347 Pup to date.

5.2.10 V603 Aql

In 1918 V603 Aql (or Nova Aquilae 1918) rose to a magnitude of -0.5 during a nova eruption, making it the brightest nova of the 20th century (e.g. Payne-Gaposchkin 1964; Johnson et al. 2014). A mass ratio of $q = 0.24 \pm 0.05$, stellar masses of $M_1 = 1.2 \pm 0.2\,\mathrm{M}_\odot$ and $M_2 = 0.29 \pm 0.04\,\mathrm{M}_\odot$ and an inclination of $i = 13° \pm 2°$ have been estimated by Arenas et al. (2000). Retter & Naylor (2000) estimated $\dot{M}$ between $9.2 \times 10^{-9}\,\mathrm{M}_\odot\,\mathrm{yr}^{-1}$ and $9.47 \times 10^{-8}\,\mathrm{M}_\odot\,\mathrm{yr}^{-1}$. Arenas et al. (2000) found both super- and sub-orbital frequencies, as with IM Eri.

V603 Aql has previously been observed in the radio regime by Coppejans et al. (2015), as well as Barrett et al. (2017). The first authors took two observations in the $4 - 8\,\mathrm{GHz}$-band with the VLA in the A configuration during April 2014. In the first epoch, the emission displayed a spectral index of $\alpha = 0.54 \pm 0.05$ and a peak flux density of $178.2\,\mu\mathrm{Jy\,beam}^{-1}$

(RMS $4.3\,\mu$Jy beam^{-1}) and in the second, a week later, $\alpha = 0.16 \pm 0.08$ with a peak flux density $190.5\,\mu$Jy beam^{-1} (RMS $3.9\,\mu$Jy beam^{-1}). The beam sizes of these observations where $0.40'' \times 0.38''$ and $0.46'' \times 0.33''$ respectively. During the first observation, short term variability down to a time scale of 217 s was found, but V603 Aql was not variable in the second observation. The peak amplitude of the variability was $61\,\mu$Jy beam^{-1}. The authors note that the radio emission observed is consistent with gyrosynchrotron emission, cyclotron maser emission and optically thick synchrotron emission.

V603 Aql was also observed twice in 2013 with the VLA in the $4-6$, $8-10$ and $18-22$ GHz-bands (Barrett et al. 2017). The authors note that the measured flux densities may be in error, because 3C295 (a radio source that is spatially resolved at high frequencies, and with no calibration models) was used as a flux standard. It was detected once in the $4-6$ GHz-band ($24\pm8\,\mu$Jy), twice in the $8-10$ GHz-band ($51\pm20\,\mu$Jy and $79\pm14\,\mu$Jy), and not at all in the $18-22$ GHz-band. Following the discussion in Barrett et al. (2017), should the source not be detected, 3σ-upper limits for the $4-6$, $8-10$ and $18-22$ GHz-bands are 75, 75 and $99\,\mu$Jy, respectively.

5.2.11 CM Phe

CM Phe (designated Phoenix 1 by Downes et al. (1997)) is a 15th magnitude object, one of the faintest targets of this study. Historically, CM Phe has proven to be notoriously difficult to locate. Jaidee & Lyngå (1969) correctly identified it while observing a fainter star located a few arcminutes away from L218-28 (the object mistaken for CM Phe for many years). Based on, amongst other things, the presence of TiO bands in the spectrum of the secondary, the spectral type is estimated to be M2-5 (Hoard et al. 2001). CM Phe has a poorly sampled long-term optical light curve, and is likely a DN. There are no reports of radio observations of CM Phe in the literature.

5.3 Observations

5.3.1 MeerKAT Observations: NL Snapshot Survey

The targets were observed for approximately 2 hours with the MeerKAT radio interferometer. Typically the primary calibrator was observed at the start of the observing run and then the secondary calibrator and target were observed, alternating between them for the remainder of the

observation. The observations were taken in the L -band (centered at 1284 MHz) with a bandwidth of 856 MHz, consisting of 4096 channels. Visibilities were recorded every 8 seconds and on average between 60 and 62 of the 64 MeerKAT antennas were utilised. Table 5.2 summarises the details of these MeerKAT observations.

MeerKAT Data Reduction

The majority of the data reduction makes use of CASA (Common Astronomy Software Applications; McMullin et al. 2007). The first step of the date reduction involves unflagging the data making use of the CASA task `unflag`. Sometimes automatic flagging routines are implemented by SARAO and the data received are not in the raw form. Unflagging the data is a precaution that ensures that no data are unnecessarily flagged and consequently maximises the S/N ratio.

In the second step the data are flagged making use of AOFlagger version 2.9.0 (Offringa 2010). AOFlagger is an automatic flagging algorithm written in C++ and thoroughly tested with LOFAR. It employs a one-dimensional mathematical morphological technique called the scale-invariant rank (SIR) operator (Offringa, van de Gronde & Roerdink Offringa et al.). This SIR operator is capable of finding data that are likely RFI-corrupted in frequency or time domains.

The data are then averaged by a factor of 8 in frequency, resulting in 512 channels, each with a bandwith of 1.67 MHz. The CASA task `mstransform` is used to perform the averaging.

Data reduction and first generation calibration were done in CASA v5.1.1, using standard procedures set out in the CASA cookbook[†]. The 1GC reduction process involved multiple steps. CASA algorithms compare data from the observation with the Fourier transform of model visibilities from a well-known calibrator model. This calibrator model is defined using the task `setjy`. Initial phase-only correction and antenna-based delays are solved using the task `gaincal` which solves for complex gains and delay calibrations, while `bandpass` is used to calculate a bandpass correction of the relative system gain over the frequency range of the observation. Thereafter, `setjy` is used to define model data based on the secondary calibrator. Complex gains are solved using `gaincal`, applying the bandpass and delay solutions on the fly. Using the known flux of the primary calibrator, the secondary calibrator gain corrections are then scaled accordingly with `fluxscale`. Finally these calibrations are applied using `applycal`. After 1GC a small amount of data are flagged using the CASA `flagdata` task in rflag and tfcrop mode. RFlag and TFCrop are algorithms that automatically detects and flag data. RFlag implements a sliding window

[†]See `https://casa.nrao.edu/casa_cookbook.pdf` and `http://casaguides.nrao.edu/`

Table 5.2: Radio observations log

Name	Start Date and Time (UTC)	Primary Calibrator	Secondary Calibrator	Integrated Time on Target (seconds)	Number of antennas
IX Vel	31/10/18 00:44:37.1	J0408-6545	J0825-5010	6246	61
V3885 Sgr	30/10/18 18:28:54.6	J1939-6342	J1937-3958	6253	61
V341 Ara	29/03/19 00:13:21.9	J1939-6342	J1726-5529	7183	60
V5662 Sgr	01/04/19 03:18:49.0	J1939-6342	J1924-2914	8069	60
IM Eri	30/03/19 10:20:54.6	J0408-6545	J0409-1757	8084	60
LS IV -08 3	29/03/19 00:30:25.5	J1939-6342	J1733-1304	6294	60
RW Sex	31/03/19 22:46:05.9	J1331+3030	J1058+0133	6293	60
UU Aqr	28/06/19 23:06:45.8	J1939-6342	J2225-0457	7180	62
V347 Pup	27/06/19 09:06:10.7	J0408-6545	J0538-4405	6285	60
V603 Aql	26/02/19 03:10:14.2	J1939-6342	J1911-2006	5367	61
CM Phe	29/06/19 01:29:22.1	J1939-6342	J2357-5311	7198	62

Table 5.3: Follow-up radio observations log

Name	Start Date and Time (UTC)	Primary Calibrator	Secondary Calibrator	Integrated Time on Target (seconds)	Number of antennas
V3885 Sgr	06/11/19 17:15:10.4	J1939-6342	J1924-2914	10732	61
V603 Aql	26/10/19 16:00:41.1	J1939-6342	J1911-2006	9835	60

statistical filter. TFCrop detects and flags outliers in the two-dimensional time-frequency plane. The primary and secondary calibrators that have been used in the steps described above are listed in Table 5.2.

Imaging was done with DDFacet, is a multi-facet-based radio imaging package (Tasse et al. 2018). Briggs weighting with a robust parameter of -0.5 and the SSD deconvolution algorithm were chosen. Self-calibration is implemented making use of killMS software and using the CohJones solver (complex half-Jacobian optimization for n-directional estimation; see Smirnov & Tasse (2015) and the reference therein for more details). Noise was measured in the local area surrounding the source and upper limits are defined as three times the noise.

5.3.2 MeerKAT Observations: Further NL Follow-up

Given the strong detections ($> 11\sigma$) of V3885 Sgr and V603 Aql, follow-up observations were focused on these two targets. The follow-up observations were twice as long as the initial survey observations to give a track length of ~ 4 hours. The goal of these observations was to analyse the time variability and the spectral shape of the observed radio emission. Table 5.3 gives the details of the follow-up observations.

The follow-up radio observations were also simultaneous with optical (MeerLICHT) and UV/X-ray (*Swift*) coverage. Additionally, for V603 Aql, higher-frequency radio data from the Arcminute Microkelvin Imager (AMI) were planned to be obtained. This was not possible for the follow-up observation of V3885 Sgr because of the southern declination.

Unfortunately the challenges of obtaining truly simultaneous multi-wavelength coverage presented themselves during these follow-up observations. MeerLICHT optical observations of V3885 Sgr were not possible because the radio observations commenced before sunset. With the help of Julian Osborne from the University of Leicester, both *Swift* UltraViolet and Optical Telescope (UVOT) and X-Ray Telescope (XRT) observations were scheduled for both V3885 Sgr and V603 Aql. Unfortunately, V3885 Sgr was too bright and *Swift* rejected it during the XRT observations. The UVOT data for V3885 Sgr was also contaminated to such a degree that

Table 5.4: SAAO 1.9 m Telescope observations

Start Date and Time (UT)	Target	Exposure time	Number of spectra
02/08/2019 01:33:28	V5662 Sgr	900	6
02/08/2019 23:51:00	V5662 Sgr	900	9
04/08/2019 02:44:05	V5662 Sgr	900	11
13/08/2019 17:32:31	LSIV -08 3	900	19

nothing significant could be recovered due to an eruption of a recurrent nova in M31. V603 Aql has an almost equatorial declination and can thus be observed by AMI in the northern hemisphere as well, but high wind speeds prevented this on the day of observation. As with V3885 Sgr, MeerKAT observations for V603 Aql were scheduled to commence before sunset and thus ruling out MeerLICHT observations. *Swift* UVOT rejected V603 Aql because of its high brightness, but fortunately XRT observations were successful.

V603 Aql was observed 3 times by *Swift* XRT with the UVM2 filter. The exposure time of each observation was 1800 s and the time between observations was 1.5 hours. Observations were conducted with UVOT event mode, to see if minute timescale variability can be observed. V603 Aql has previously been observed by *Swift* once, briefly in 2012 and detected at about 0.5 counts/second.

5.3.3 Time-Resolved Optical Spectroscopic Observations

Spectroscopic observations of V5662 Sgr and LSIV -08 3 were conducted making use of the SAAO 1.9 m telescope at the South African Astronomical Observatory site near Sutherland and the long slit spectrograph (SpUpNIC; Crause et al. 2016). On 1–3 August 2019, V5662 Sgr was observed by myself and TS Lambert and on 13 August 2019, TS Lambert observed LSIV -08 3. The spectrograph configuration made use of grating number 6, covering a 2780 Å-range. The slit width was 1.05″and 1×2 binning was used, resulting in resolving power ($\lambda/\delta\lambda$) of $R \simeq 2000$. Copper-Argon arc lamp spectra were taken to bracket each target exposure. A summary of the observations are given in Table 5.4.

Data Reduction

The spectra were extracted using standard routines in IRAF[‡]. Wavelength calibration was done using Copper-Argon arc lamps and cosmic ray cleaning was done using the lacosmic routine (van Dokkum 2001).

Cross correlation of individual spectra with a high S/N template was attempted (by making use of the IRAF function, `xcsao` in the RVSAO package (Kurtz & Mink 1998)); however, this method did not produce good results, therefore I fitted Gaussians to the Hα emission lines to calculate the Doppler shift and obtain the radial velocities. The Gaussian function were fit making use of the features in a python package called Lmfit (Non-Linear Least-Squares Minimization and Curve-Fitting for Python). A python function to calculate a Lomb-Scargle periodogram (Vanderplas et al. 2012; Vanderplas & Ivezić 2015) was then used to identify the periodic signals.

[‡] `http://iraf.noao.edu`

Chapter 6

Results and Discussion

The ThunderKAT NL survey is the largest survey of NL CVs in the radio band conducted to date. I will now present all the MeerKAT results in Section 6.1. This includes results from both the initial snapshot survey of eleven NLs, as well as the follow-up radio observations of V3885 Sgr and V603 Aql. Section 6.2 is where I discuss the results of the X-ray observations obtained simultaneously with the radio follow-up of V603 Aql. In Section 6.3 I construct broad spectral energy distributions (SEDs) for the sample from published multi-wavelength data, and use them to place constraints on the mass transfer rates of these eleven NL systems. I then search for correlations between radio emission and binary system parameters, as well as emission in other wave bands in Section 6.4. Finally, I present the results of the time-resolved optical spectroscopy in Section 6.5.

6.1 MeerKAT Observations

The results of all the MeerKAT radio observations are presented in Table 6.1. Four out of the eleven NLs were detected: V3885 Sgr, IM Eri, RW Sex and V603 Aql. This was the first time that IM Eri has been detected in the radio regime. In Figure 6.1 colour maps with contours overlayed are presented for the four detected systems. Analysis of the first year of ThunderKAT data revealed an epoch-to-epoch drift in the flux scale of up to ± 10 per cent, which has since been tracked down to the reference calibration method that was used. Hence the estimates may include a few percent of calibration error, though this is not the dominant source of error. The specific radio luminosities ($L_\nu = 4\pi d^2 F_\nu$ where F_ν is measured flux density) of these detected

NLs range from $4.3 \pm 1.1 \times 10^{15}$ to $27 \pm 4 \times 10^{15}$ erg s^{-1} Hz^{-1}.

In the case of three systems, V347 Pup, IX Vel, and LSIV -08 3, radio signals that are not considered to be significant detections are seen. For the observation of V347 Pup, a weak signal with an integrated flux density of 28 $\pm$ 14 μJy was present, but this does not satisfy the 5σ detection threshold. Furthermore, the offset from the optical position was $\sim 2''$, the signal shape is not consistent with the shape of the beam, and other similar signals are also found surrounding the expected position of V347 Pup. This is not considered a detection, but the radio flux is reported here, in case a detection at a similar flux and with reduced noise levels is made in future. Radio emission just above 3σ, but considerably smaller than the beam size, is also seen $\sim 2''$ and $\sim 6''$ from the optical coordinates of IX Vel and LSIV 08 3, respectively. Again, these are not considered detections.

The remaining systems were also not detected, typically with 3σ upper limits of $\sim 33\,\mu$Jy beam^{-1}. The upper limits on the specific luminosities of the non-detected NLs range between $0.41 \pm 0.02 \times 10^{15}$ erg s^{-1} Hz^{-1} (for IX Vel) and $4.63 \pm 0.36 \times 10^{15}$ erg s^{-1} Hz^{-1} for (CM Phe). The upper limit for IX Vel is a factor of ~ 14 deeper than the previous upper limit of 5.89×10^{15}erg s^{-1} Hz^{-1} for IX Vel by Körding et al. (2011). However, I note that the measurement is at a lower frequency. Radio maps for all the non-detected NLs are presented in Figure 6.2 and 6.3.

Körding et al. (2011) detected V3885 Sgr, but not AC Cnc or IX Vel. Coppejans et al. (2015) detected 75% (3 out of 4) of their sample of NLs in the radio regime. The detection rate for this MeerKAT survey is considerably lower ($\approx$ 36%). Coppejans et al. did however, select the four brightest and nearest NLs (and the most optically luminous) from the Ritter and Kolb catalogue (Ritter & Kolb 2003) as their targets.

In the follow-up observations of V3885 Sgr and V603 Aql, both were detected again, unsurprisingly (see Figure 6.4). The radio flux density for V603 Aql was more or less consistent with that measured in the previous observation eight months earlier, while the radio flux density of V3885 Sgr in the second epoch (385 $\pm$ 20 μJy) was considerably higher than in the first epoch (256 $\pm$ 25 μJy), approximately one year earlier.

Given the lack of polarisation data, it is not possible to eliminate (or favour) any previously suggested radio emission mechanisms. The presence of significant short term variability in V603 Aql (as will be discussed soon), does however allow me to eliminate thermal emission from a large gas cloud as the source of the radio emission, for the reasons mentioned in Section 3.4.3 and discussed in Coppejans et al. (2015).

Table 6.1: Results from radio observations. The beam dimensions of each observation is given in the second and third columns. The fourth column gives the integrated radio flux density of detected sources and the 3σ upper limit for non-detections. The specific radio luminosity, or upper limit, calculated using the *Gaia* distances is presented in fifth column and RMS noise of the image surrounding the expected source position in the sixth. The last column gives inband spectral indices for detected sources. The first eleven rows are the initial snapshot survey observations, while the final two rows below the lines are the longer follow-up observations.

Name	Beam size (")	Beam position angle (°)	Integrated Radio Flux (μJy)	Radio Luminosity ($\times 10^{15}$erg s^{-1} Hz^{-1})	RMS (μJy beam^{-1})	Spectral Index
IX Vel	5.9 × 4.1	-50.3	<42	<0.4	14	
V3885 Sgr	6.6 × 5.2	38.6	256 ± 25	5.4 ± 0.5	13	-0.6 ± 0.7
V341 Ara	5.9 × 4.6	-15.1	<27	<0.8	9	
V5662 Sgr	5.3 × 4.5	-25.7	<24	<0.8	8	
IM Eri	5.7 × 5.3	-73.9	99 ± 26	4.3 ± 1.1	11	1.2 ± 1.6
LS IV -08 3	5.8 × 4.7	-8.1	<33	<1.8	11	
RW Sex	6.4 × 5.0	-55.0	82 ± 23	5.5 ± 1.6	11	-1.5 ± 1.0
UU Aqr	6.1 × 5.5	9.0	<39	<3.1	13	
V347 Pup	5.7 × 4.5	-6.8	<30	<3.1	10	
V603 Aql	6.9 × 5.3	42.4	233 ± 36	27 ± 4	20	0.2 ± 1.1
CM Phe	6.2 × 4.5	-39.2	<30	<4.6	10	
V3885 Sgr	6.2 × 5.1	74.5	385 ± 20	8.1 ± 0.5	11	-0.2 ± 0.4
V603 Aql	7.2 × 5.1	-32.9	211 ± 23	24.8 ± 2.7	12	-1.5 ± 0.8

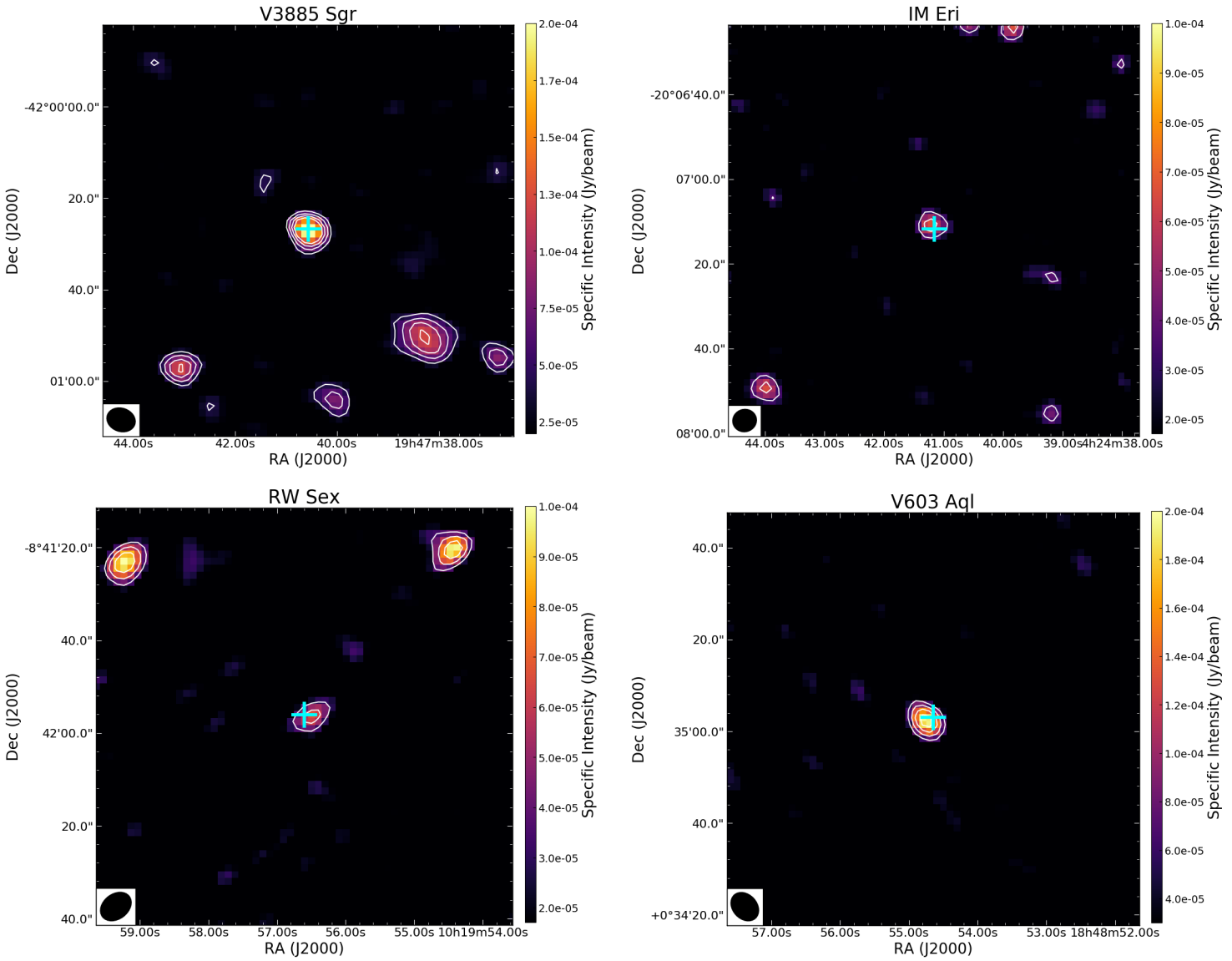

Figure 6.1: Radio colour maps and contours of the four NLs that were detected. In these images, as well as those in Figure 6.2 and 6.3 contour levels are at 3-, 5-, 7- and 9σ levels. The cyan plus indicates the position of the optical coordinates and does not correspond to error bars. These images are $1.5' \times 1.5'$ in size and the beam shape is shown in the bottom left corner. Refer to Table 6.1 for the beam dimensions. North is up and east to the left.

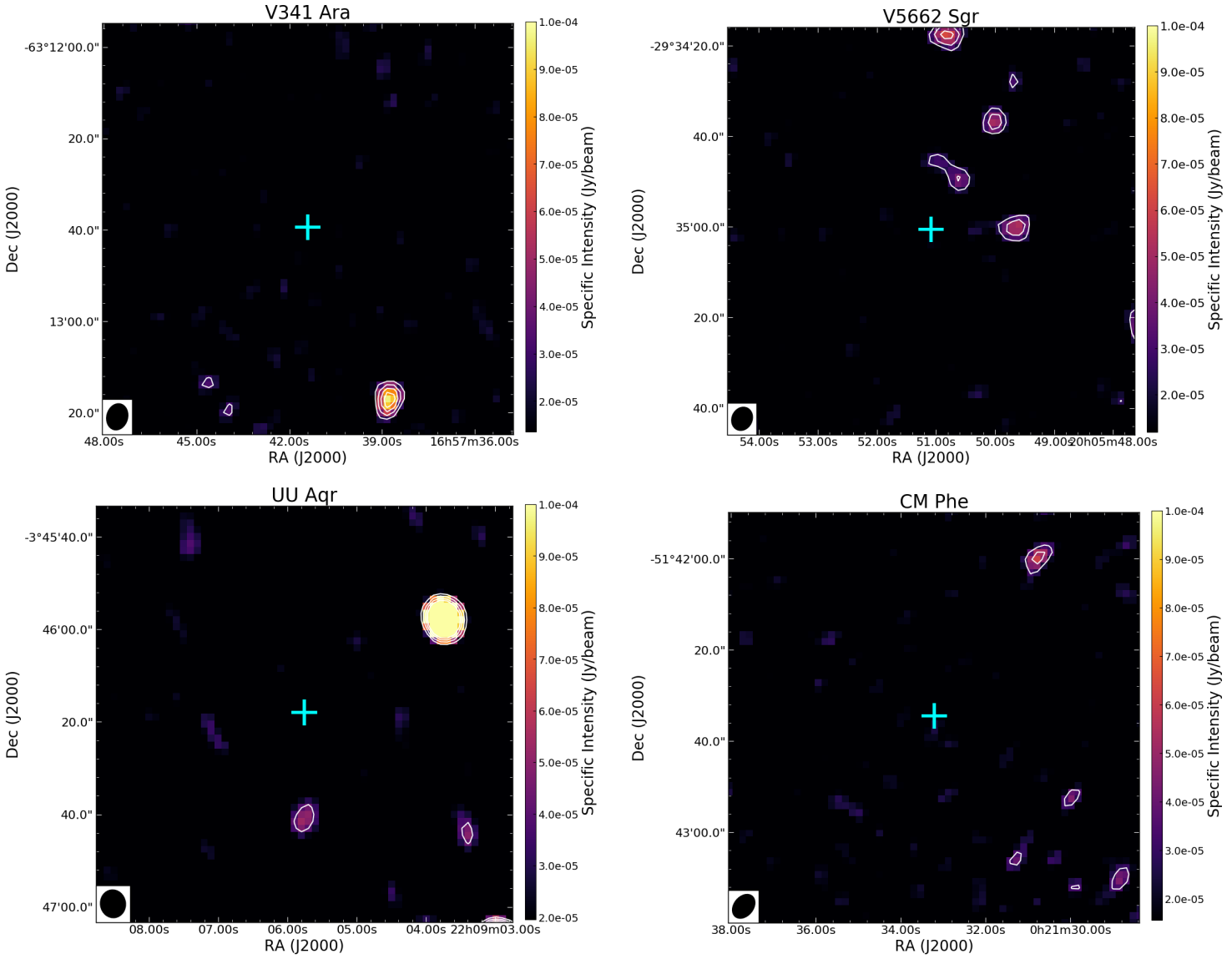

Figure 6.2: Radio colour maps and contours of the four NLs that were not detected. Refer to the caption of Figure 6.1 for more information pertaining to these plots.

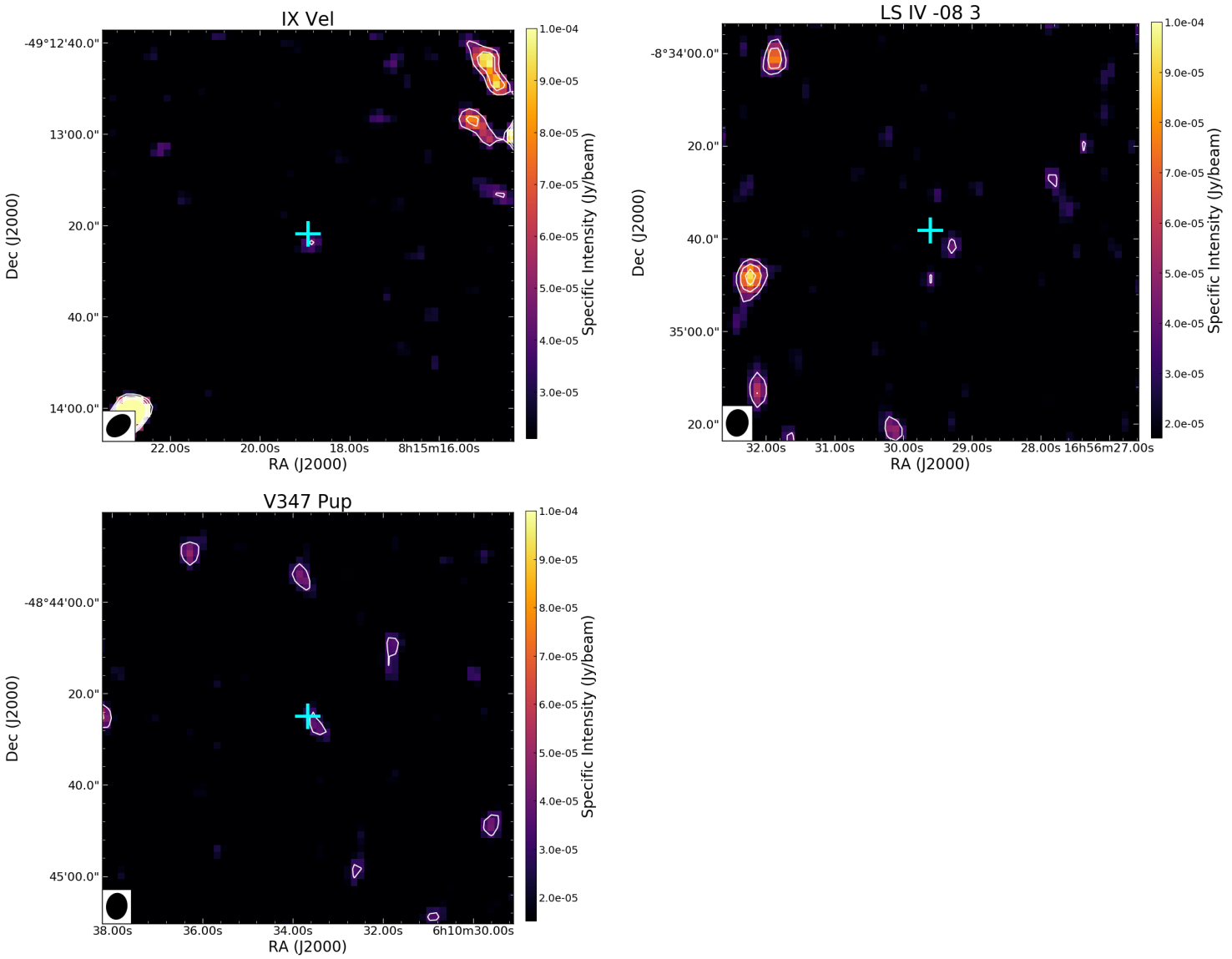

Figure 6.3: Radio colour maps of the remaining three non-detected NLs. Radio emission just above 3σ was present $2''$ and $6''$ away from the expected position for IX Vel and LSIV -08 3 respectively. A 3.6σ signal was present centered $2''$ away from the optical coordinates of V347 Pup. These systems are not considered to be detected. See the text for a discussion. Refer to the caption of Figure 6.1 for more information pertaining to these plots.

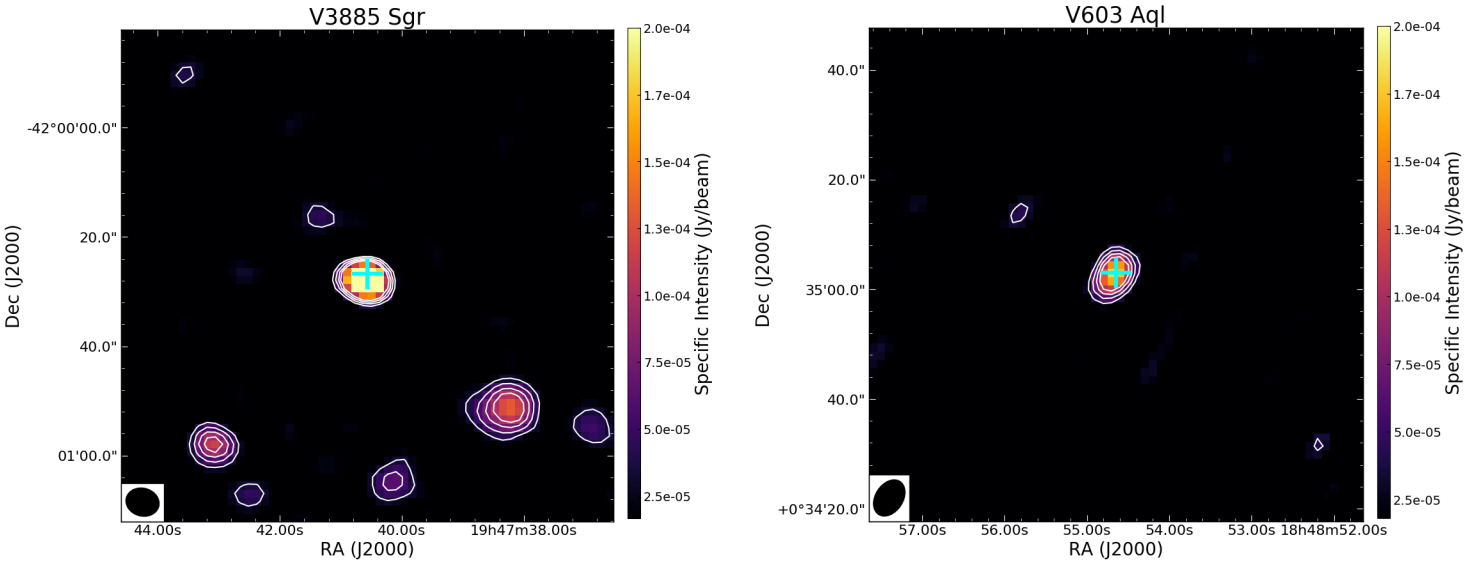

Figure 6.4: Radio colour maps of the follow-up observations of V3885 Sgr and V603 Aql. Refer to the caption of Figure 6.1 for more information pertaining to these plots.

6.1.1 Spectral Indices

The spectral indices ranged from -1.5 ± 1.0 to 1.2 ± 1.6 (see Table 6.1). These indices were calculated by first splitting the 865 MHz bandwidth into two frequency sub-bands, one centered at 1070 MHz and the other at 1498 MHz, and then imaging these frequency sub-bands to obtain a flux measurement in each. Errors are calculated using the same method as Espinasse & Fender (2018). V3885 Sgr, RW Sex and V603 Aql have previously been detected in the radio regime. V3885 Sgr showed a spectral index of $\alpha = -0.75 \pm 0.35$ when observed by Körding et al. (2011) at 5.5 GHz and 9 GHz, compared to the in-band value of $\alpha = -0.6 \pm 0.7$ at 1.3 GHz, that I calculate. Coppejans et al. (2015), observing at 4.9 GHz, found $\alpha = -0.5 \pm 0.7$ for RW Sex, and for V603 Aql $\alpha = 0.54 \pm 0.05$ during one epoch and $\alpha = 0.16 \pm 0.08$ in another. I measure $\alpha = -1.5 \pm 1.0$ for RW Sex, $\alpha = 0.2 \pm 1.1$ for V603 Aql and $\alpha = 1.2 \pm 1.6$ for IM Eri from the in-band measurement at 1.3 GHz. The spectral indices measured from these observations are thus consistent, within the large errors, with values previously reported for the same objects using higher-frequency data.

For the follow-up observations, spectral indices of -0.2 ± 0.4 and -1.5 ± 0.8, were calculated for V3885 Sgr and V603 Aql, respectively. The uncertainty on these indices are very large, so while the spectral indices differ for both targets between epochs (more so for V603 Aql than for

V3885 Sgr), they can still be reconciled with those of previous observations.

Unfortunately, due to the large uncertainties on the spectral indices and the relatively large range of spectral indices, it is not possible to eliminate any radio emission mechanisms.

6.1.2 Time Variability

V3885 Sgr and V603 Aql were detected at high enough flux density to split the observations up into multiple, shorter epochs of $\sim$ 15 minutes (the length of one on-target scan) with the aim of looking for shorter timescale variability. Each of these shorter epochs were imaged separately and then a flux measurement was taken. However, the universal variability across these sub-epochs (and thus the underlying calibration and imaging statistics of these sub-epochs) has not yet been properly evaluated. The techniques used to calibrate these data are now known to give rise to a flux scale drift of up to $\sim$ 10%, and image quality and noise levels across sub-epochs are not consistent. Therefore, all flux measurements in this subsection probably include an additional few percent of error (albeit not the primary source of error) that has not been accounted for. The integrated radio flux density has been plotted as a function of time for both epochs of both systems in Figure 6.5.

V3885 Sgr showed sinusoidal-type time variability in both epochs, although in the second epoch V3885 Sgr was more radio bright. The amplitude of this variability was approximately $50\,\mu$Jy in the first epoch, and between 50 and $100\,\mu$Jy in the second.

V603 Aql showed no variability within the first epoch, but during the second epoch very interesting flare-type behaviour was observed. Four 'flares' were detected, all separated by irregular intervals from one another, and in between these flares V603 Aql fell to below the detection threshold (for these periods 3σ upper limits have been plotted in Figure 6.5). The brightest flare peaked at 412 ± 146 μJy. The 3σ-upper limits are around $150\,\mu$Jy. All the flares were restricted to one on-target scan (approximately 15 minutes). This is remarkably similar to the behaviour that was observed by Coppejans et al. (2015). In their first epoch that they observed V603 Aql, it peaked at 260.5 ± 12.5 μJy beam^{-1} in the first half of the observation, before subsequently dropping to approximately $170\,\mu$Jy beam^{-1} for the rest of the observation (a $\sim 90\,\mu$Jy drop, or in other words, it reduced to $\sim$ 65% of its peak flux). The flare occurred within about 20 to 30 minutes. They also found that the emission was time-variable down to 217 seconds. When they observed again, about a week later, V603 Aql did not show any time variability during the $\sim$ 38 minute observation.

Given this peculiar flaring behaviour, it was considered that other non-detected NLs in this survey might have exhibited one or two flares that were smeared out over the 2 hour course of observations, hence producing a non-detection when the entire 2 hour observation was averaged to create an image. All the observations (i.e. of all eleven NLs) were consequently split up into shorter time intervals of $\sim$ 15 minutes, as was done with the observations of V3885 Sgr and V603 Aql, and reanalysed for any potential flares. No such flares were found in any of the other data. In other words, the non-detected NLs remain non-detected, and no radio emission above the detection threshold was found for any of the non-detected NLs during any $\sim$ 15 minute period, throughout the observations.

6.2 Follow-up X-ray Observations

The *Swift* XRT observations for V603 Aql showed interesting, rapid variability. On average 0.438 counts/second were detected. Unfortunately, the MeerKAT radio observations could not be imaged at the same high time resolution, hence it is not possible to use these two datasets to investigate correlations between the variability in the different wavebands. In Figure 6.6 the simultaneous *Swift* XRT observations and follow-up MeerKAT radio observations of V603 Aql are presented together.

6.3 Estimating $\dot{M}$ from Broadband SEDs

6.3.1 Constructing the SEDs

In Figure 6.7 I have construct broadband spectral energy distributions (SEDs) of the NL sample, making use of published multi-wavelength data. As expected, each broad SED shows, in the UV to IR wavebands, a component that appears consistent with black body emission from an accretion disc. Lower and higher energy emission, belonging to other components, can also be seen. Warner (2006) gives an overview of the emission observed in CVs across the whole electromagnetic spectrum.

All three systems with multiple detections at different radio wavelengths (i.e. the three previously detected systems that were detected in this survey as well: V3885 Sgr, RW Sex and V603 Aql) exhibit a radio flux that is decreasing with increasing frequency, i.e. a negative spectral index α. In Section 6.1.1 above, both positive and negative in-band spectral indices were reported. The broader frequency coverage of the combined MeerKAT and VLA/ATCA

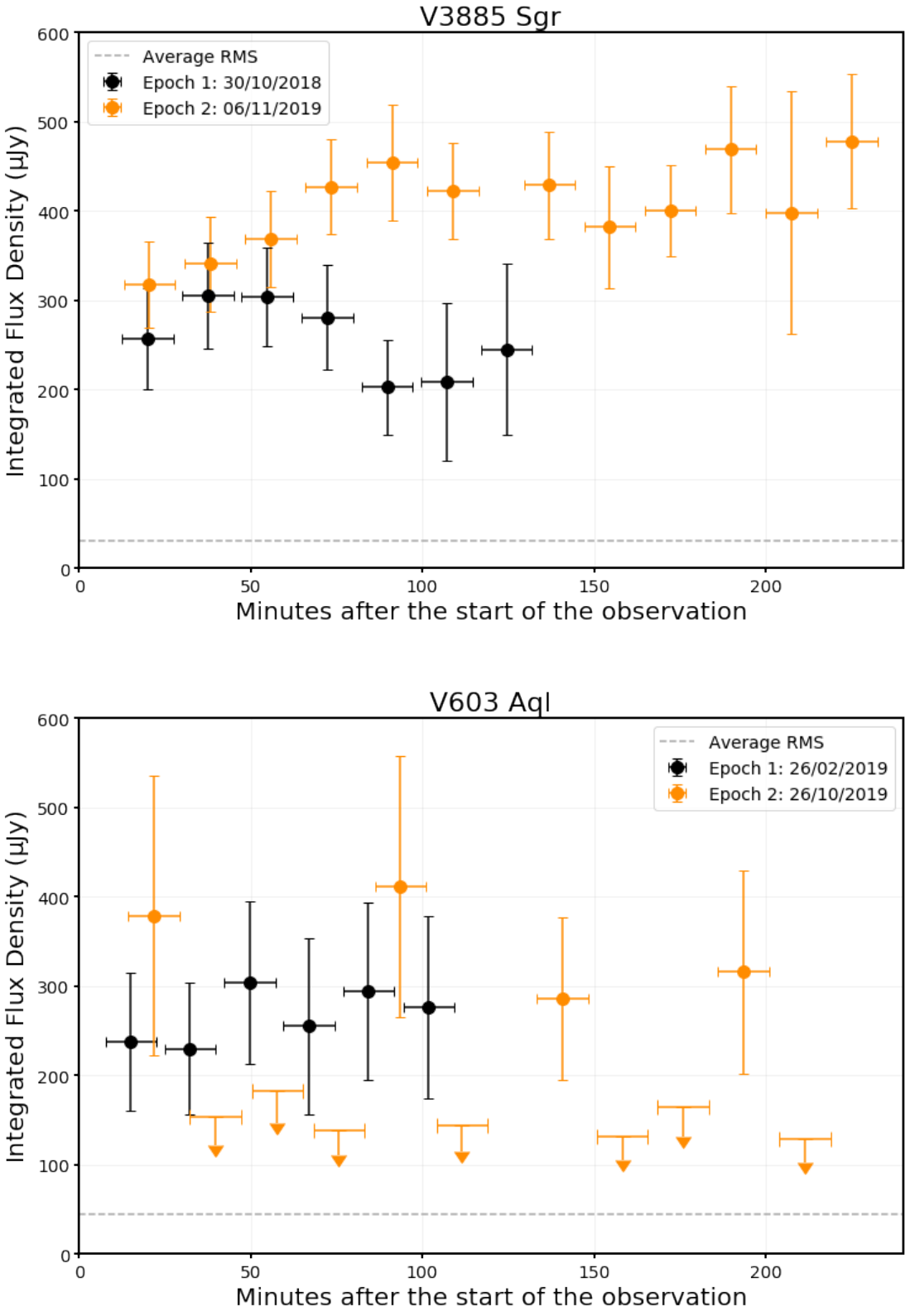

Figure 6.5: The initial 2-hour snapshot survey observations of V3885 Sgr and V603 Aql are shown in black, where radio flux density has been plotted as a function of time. The orange datapoints represent the 4-hour follow-up radio observations of both systems.

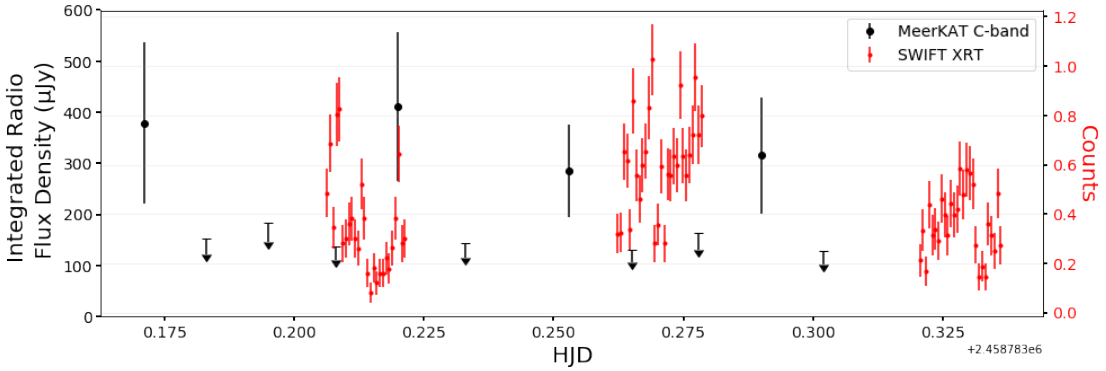

Figure 6.6: *Swift* XRT counts observed for V603 Aql displaying significant variability on a timescale of minutes. During the MeerKAT observation, interesting flaring activity was also observed. The time resolution of these two datasets is, however, too different to investigate possible correlations.

data should be a more reliable indication of α, but this discrepancy may also be caused by variability on both long and short timescales. Coppejans et al. (2015) observed that the spectral index of V603 Aql differed in two different epochs of observation, a week apart, and that the spectral index of TT Ari changed during a flare.

6.3.2 The Black Body Accretion Disc Model

A black body model of an accretion disc has been overplotted on these SEDs, using input system parameters summarized in Table 6.3.2, many of which are taken from the literature and mentioned in the relevant subsections of Section 5.2. The curves shown in Figure 6.7 are not fits to the SEDs, and do not include any contribution from the WD or donor star. I simply varied the input $\dot{M}$ of the disc model, and selected the value which produces the black body disc spectrum that most resembles the observed SED. Those accretion rates are given in Table 6.3.2 for each system. The black body model calculates the shape of a black body for a range of temperatures dependent on the viscous dissipation rate D of an optically thick Keplerian accretion disc,

$$D(R) = \frac{3GM\dot{M}}{4\pi R^3}\left[1 - \left(\frac{R_*}{R}\right)^{1/2}\right] \tag{6.1}$$

where G is the gravitational constant, R is the radius of the disc, M is the WD mass, $\dot{M}$ is the accretion rate and R_* is the WD radius.

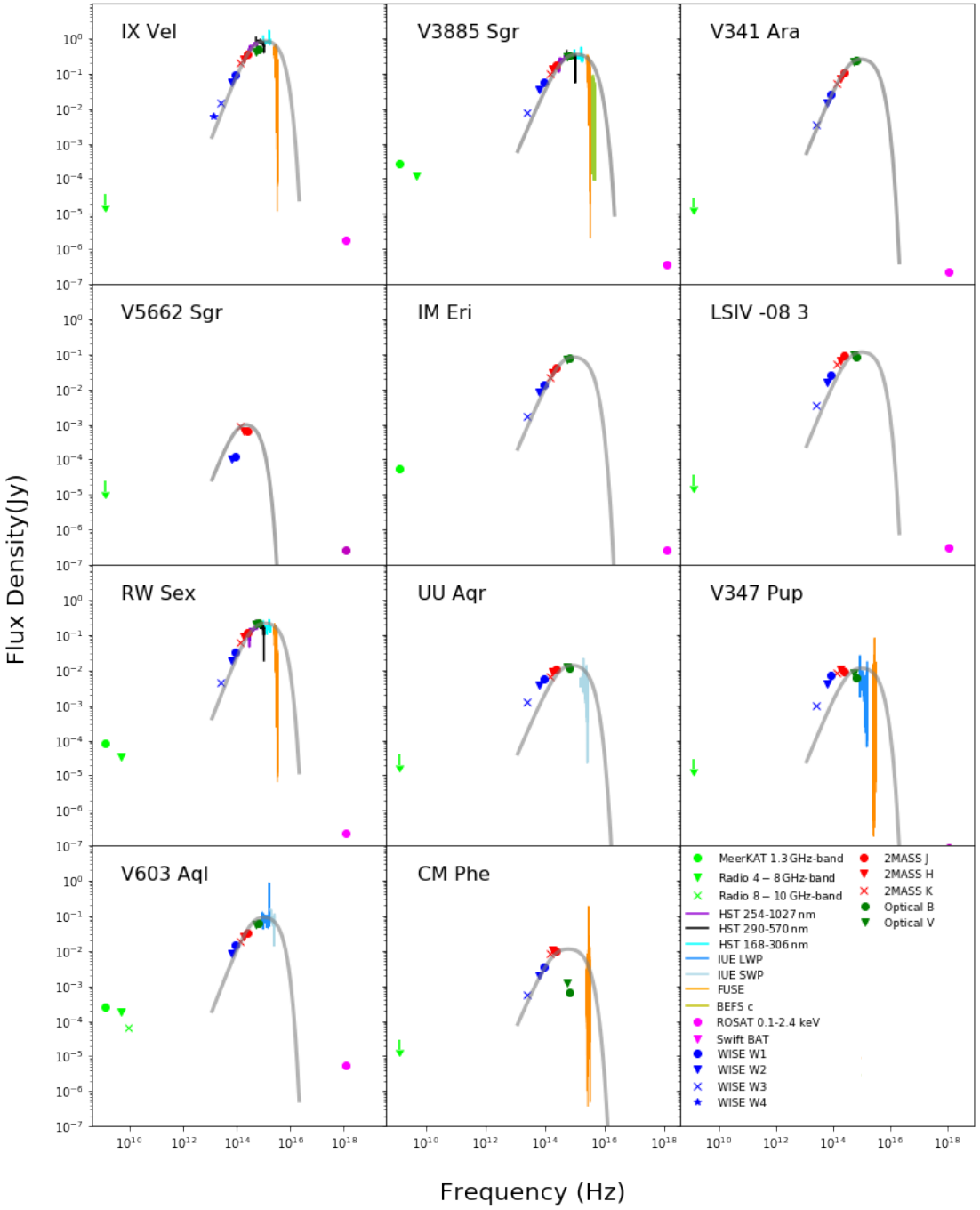

Figure 6.7: SEDs for the NL sample, constructed using the MeerKAT radio observations as well as published data from a large collection of earlier observations. A black body disc model with appropriate system parameters where possible, and the mass accretion rate which gives rise to a curve that best resembles the data, is overplotted. Refer to Table 6.3.2 for the system parameters and the text for more detail.

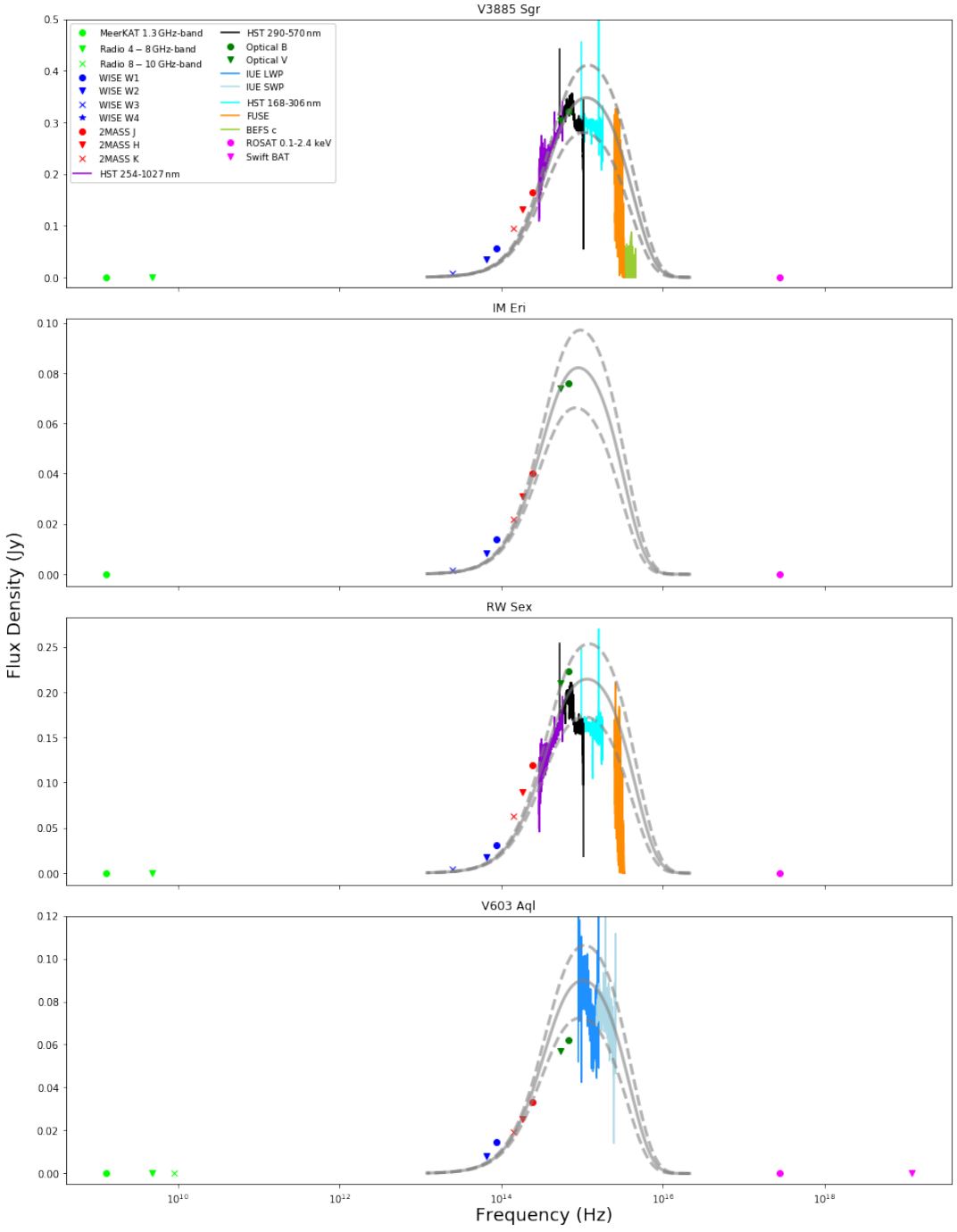

Figure 6.8: SEDs for the detected NLs in the sample. A black body disc model is overplotted, with the optimal accretion rate to resemble the data as a solid grey line, and accretion rates 25% greater and smaller as dashed grey lines. Note that the $\dot{M}$ derived for IM Eri is particularly uncertain, since there are no UV data available (see Fig 6.7), and since the binary parameters relevant to the black body model include an assumed typical inclination and WD mass. Nonetheless, IM Eri is the least optically luminous system detected in the radio.

Table 6.2: The system parameters used for the black body disc models shown in Figure 6.7. References for the values that are available in the literature may be found in Section 5.2

Name	$M_1(\mathrm{M}_\odot)$	$M_2(\mathrm{M}_\odot)$	$i(^\circ)$	$\dot{M}(\times 10^{-9}\,\mathrm{M}_\odot\,\mathrm{yr}^{-1})$
IX Vel	0.8	0.52	57	7
V3885 Sgr	0.675	0.473	60	8
V341 Ara	0.75*	0.27*	30	3.5
V5662 Sgr	0.75*	0.09*	57*	0.005
IM Eri	0.75*	0.24*	57*	2.5
LS IV -08 3	0.75*	0.45*	57*	5
RW Sex	0.84	0.62	34	8
UU Aqr	0.67	0.2	78	2
V347 Pup	0.63	0.52	84	6
V603 Aql	1.2	0.29	13	3
CM Phe	0.75*	0.5**	57*	0.7

* Value not known and estimated from Knigge et al. (2011) or Warner (1995). See the text for more detail.

** See the discussion in Section 6.3.

In the case where system parameters were not known (and thus not mentioned in Section 5.2) I selected an inclination of $i = 57°$ (Warner 1995), $M_1 = 0.75\,\mathrm{M}_\odot$ and estimated M_2 using the binary and evolution parameters along the revised model track of Knigge et al. (2011). CM Phe has an orbital period above 6 hours, implying that it likely has a secondary star that has evolved off the main sequence. The calculated black body is not very sensitive to M_2, and so for CM Phe, I make the assumption that $M_2 = 0.5\,\mathrm{M}_\odot$. This corresponds roughly to an M0 dwarf; see Hoard et al. (2001) for a more complete discussion.

The inner radius of the disc is set to be 7000 km (the approximate radius for an average WD) and the outer radius is defined as $0.7R_{L1}$ where R_{L1} is the Roche lobe radius of the primary (Harrop-Allin & Warner 1996). The Roche lobe radius of the primary was calculated using Equation 6.2 (Silber 1992).

$$\frac{R_{L1}}{a} = \left(1.0015 + q^{0.4056}\right)^{-1} \tag{6.2}$$

where a is the period-dependent orbital separation and $q = M_2/M_1$. This equation is valid for $0.04 \leq q \leq 1$ with an error $< 1\%$.

For V347 Pup and UU Aqr, the black body model clearly does not resemble the observed SED. Both of these systems have high inclinations ($i > 75$), and it is thus possible that the disc is occulted to some degree, or that the disc rim is being observed. In both these cases the observed emission would not be consistent with that of a black body.

Figure 6.8 shows the black body component of the detected subsample with the most suitable accretion rate as a solid grey line, and accretion rates 25% greater and smaller, respectively, as dashed grey lines overplotted on the SEDs. This plot serves to show that the way in which $\dot{M}$'s have been inferred is fairly constraining.

6.3.3 Comparing $\dot{M}$ to Previous Estimates

For IX Vel $\dot{M} \approx 7 \times 10^{-9}\,\mathrm{M}_\odot\,\mathrm{yr}^{-1}$ shows good agreement with the observed SED. This is closer to the value of $(7.9 \pm 1.0) \times 10^{-9}\,\mathrm{M}_\odot\,\mathrm{yr}^{-1}$ which was proposed by Beuermann & Thomas (1990) than to $5 \times 10^{-9}\,\mathrm{M}_\odot\,\mathrm{yr}^{-1}$ which was proposed by Linnell et al. (2007), however, they noted that their model only excludes estimates above $8 \times 10^{-9}\,\mathrm{M}_\odot\,\mathrm{yr}^{-1}$, in which case the first mentioned value is still consistent.

For V3885 Sgr, $(5 \pm 2) \times 10^{-9}\,\mathrm{M}_\odot\,\mathrm{yr}^{-1}$ is proposed by Linnell et al. (2009). The SED agrees better with a slightly higher value of $8 \times 10^{-9}\,\mathrm{M}_\odot\,\mathrm{yr}^{-1}$, but Figure 6.8 shows that a value of 6

$\times 10^{-9}\,\mathrm{M}_\odot\,\mathrm{yr}^{-1}$ is still reasonable.

According to models by Linnell et al. (2010) the optimal $\dot{M}$ for RW Sex is $5.75\times 10^{-9}\,\mathrm{M}_\odot\,\mathrm{yr}^{-1}$. They made use of a *Hipparcos* parallax to obtain a distance of 289 pc (now known to be ≈22% too large). Other estimates are as high as $1\times 10^{-8}\,\mathrm{M}_\odot\,\mathrm{yr}^{-1}$ (Greenstein & Oke 1982). Making use of this black body model, $\dot{M}\approx 8\times 10^{-9}\,\mathrm{M}_\odot\,\mathrm{yr}^{-1}$ best suits the SED.

For UU Aqr $\dot{M}=1.0^{+0.6}_{-0.4}\times 10^{-9}\,\mathrm{M}_\odot\,\mathrm{yr}^{-1}$ has been proposed (Baptista et al. 1996). From our model we find $\dot{M}\approx 2\times 10^{-9}\,\mathrm{M}_\odot\,\mathrm{yr}^{-1}$.

V603 Aql has been estimated to have $\dot{M}$ ranging from $9.2\times 10^{-9}\,\mathrm{M}_\odot\,\mathrm{yr}^{-1}$ to $9.47\times 10^{-8}\,\mathrm{M}_\odot\,\mathrm{yr}^{-1}$ (Retter & Naylor 2000). The black body disc modelled, that best resembles the SED of V603 Aql has a $\dot{M}\approx 3\times 10^{-9}\,\mathrm{M}_\odot\,\mathrm{yr}^{-1}$ – significantly lower than Retter & Naylor, but still of the same order of magnitude.

In general, the accretion rates suggested by the observed SEDs and this simple black body disc model are slightly higher than what has previously been suggested by other authors, and this model tends to marginally underestimate the higher energy side of the disc component. Here is where I need to point out that UV extinction has not been incorporated into the black body disc models. Furthermore, at wavelengths were the accretion disc emission dominates (UV to IR), contributions from the WD and donor have also not been taken into consideration. In NLs the disc is usually considerably brighter than the stellar components, but the contributions are likely not non-significant. These missing components in the model might explain the discrepancy.

6.4 Radio Emission Correlations

In Figure 6.9 I plot radio luminosity as a function of absolute magnitude (Ritter & Kolb 2003, or VSX*) for this sample of eleven NLs, as well as for all the previous detections of non-magnetic CVs (DNe in grey and NLs in black). Note that the radio luminosities of this sample are not at the same frequency as that of previous detections. While there is no statistically significant correlation between the specific radio and optical luminosities for the existing sample, this plot does, however, show that all the NLs that were detected by MeerKAT (and all previous detections) displayed a relatively high specific optical luminosity $\gtrsim 2.2\times 10^{18}$ erg/s/Hz (corresponding to $M_V\lesssim 6.0$). Yet, not all the optically luminous NLs were detected at radio wavelengths – notably IX Vel, LSIV -08 3 and V341 Ara. These three systems do not share any common attributes (such as winds or spiral shocks), that are also not associated with some of the detected

*The International Variable Star Index; https://www.aavso.org/vsx/

NLs.

V5662 Sgr and CM Phe have optical luminosities significantly below those of the rest of the sample, and although they are currently classified as NLs, they are likely DNe in which outbursts have thus far been missed (see also Thorstensen 2020). Both have poorly sampled long-term light curves, and absolute magnitudes that are consistent with those of quiescent DN at their respective periods (e.g. Warner 1987).

In Figure 6.10 radio luminosity is plotted as a function of orbital period for this sample of eleven NLs, as well as for all the previous detected non-magnetic CVs. The MeerKAT survey has evidently been effective at sampling the entire orbital period parameter space. Throughout the range of orbital periods, radio luminosities and upper limits remain comparable.

Radio luminosities have been plotted as a function of X-ray luminosities for a number of black holes (BHs), neutron stars (NSs), transitional millisecond pulsars (tMSPs), a few CVs[†] and this sample of eleven NLs in Figure 6.11. These data are obtained from a database compiled by Bahramian et al. (2018) (see Figure 6.11 for references). The famous X-ray:radio correlation for BHs ($L_X \propto L_R^{\sim 0.6}$; Gallo et al. 2003, 2006, 2012, 2018) is plotted as a black line, and the correlations for non-pulsating ($L_X \propto L_R^{\sim 0.7}$) and hard-state NSs ($L_X \propto L_R^{\sim 1.4}$; Migliari & Fender 2006) are also plotted as blue dot-dashed and dashed lines, respectively. The detected NLs from the ThunderKAT survey are plotted in red, and the non-detected NLs in pink. The uncertainties on the x-axis correspond to *ROSAT* X-ray luminosities (Voges et al. 1999) assuming thermal bremsstrahlung with kT ranging from $5 - 20\,\mathrm{keV}$ (Pretorius & Knigge 2011), while the uncertainties on the y-axis correspond to the MeerKAT radio luminosities of the NLs scaled from 1.3 GHz to 5 GHz, using spectral indices in the range $-1 < \alpha < 1$. Take note that, unlike the other points on this plot, the radio and X-ray observations are of course not even quasi-simultaneous; however, none of the these NLs are known to display changes in their accretion state. The four NLs that have been detected are surprisingly well described by the non-pulsating NS correlation. The remainder of the sample does however fall below this correlation line, possibly by as much as an order of magnitude in radio luminosity, or even more, but might well still follow other NS X-ray:radio relations that have been proposed.

Russell et al. (2016) already noted that even during the plateau and decay phase SS Cyg is bright enough to fall close to the $L_X \propto L_R^{\sim 0.7}$ neutron star relation (this can be seen in Figure 6.11). During a flare, SS Cyg was above the NS relation, but not quite as bright as the

[†]These systems all belong to other classes of CVs than NLs. SS Cyg is a DN, AE Aqr is a probable magnetic propeller (Wynn et al. 1997) and AR Sco is interpreted to be a WD pulsar (Marsh et al. 2016).

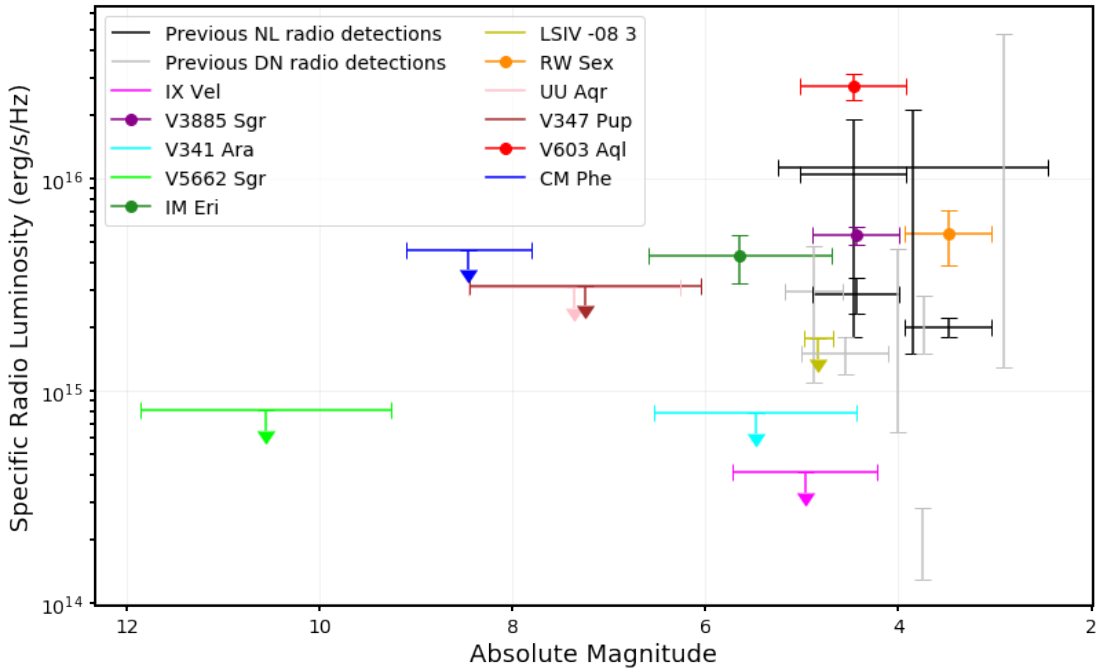

Figure 6.9: Specific radio luminosities plotted versus the absolute magnitudes for this sample of eleven NLs, with the y-error bars corresponding to the radio luminosity uncertainty and x-error bars to the magnitude range obtained from the Ritter-Kolb catalogue (Ritter & Kolb 2003), or VSX if not available from the former. All previous radio defections of DNe and NLs have also been plotted in grey and black, respectively (Körding et al. 2008; Miller-Jones et al. 2011; Coppejans et al. 2015, 2016; Russell et al. 2016; Barrett et al. 2017; Pala 2019; Coppejans & Knigge 2020). For these data points the y-error bars represent the minimum and maximum luminosities at which these sources have been detected in the radio regime, while the x-error bars represent the normal magnitude range for NLs and maximum magnitude during outburst/superoutburst for DNe. Note that the radio luminosities of this sample are not at the same frequency as that of previous detections.

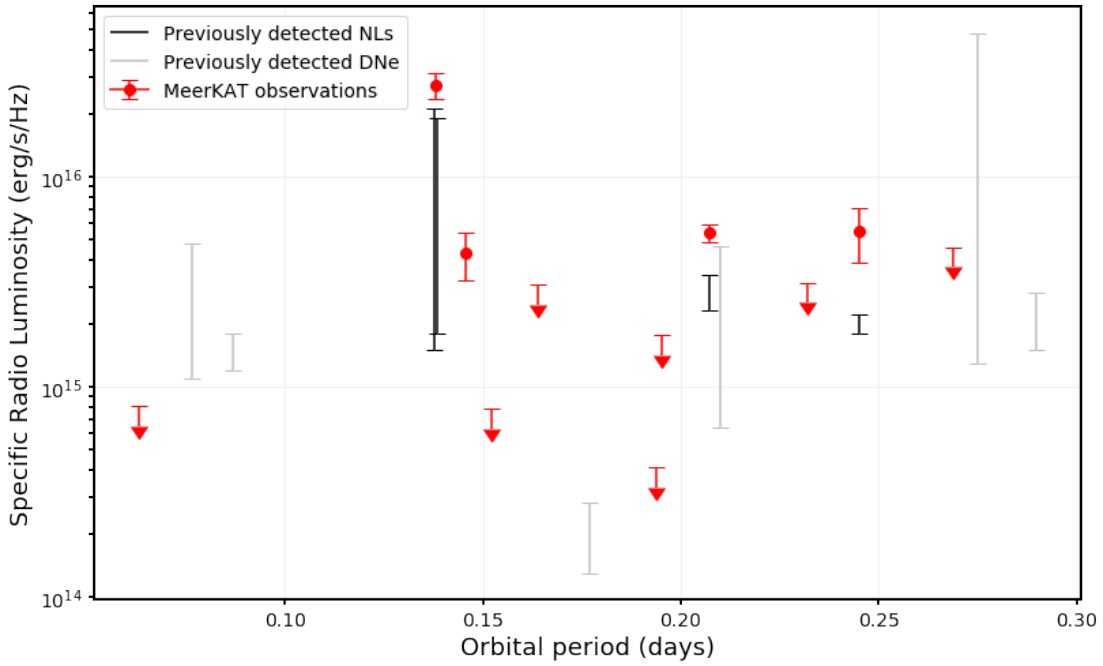

Figure 6.10: Specific radio luminosities of non-magnetic CVs as a function of orbital periods. Red symbols are for this sample of eleven NLs, with the y-error bars corresponding to the radio luminosity uncertainty. Previously reported data are shown for DNe (grey symbols) and NLs (black), where again the bars represent a range of measured radio luminosities (Körding et al. 2008; Miller-Jones et al. 2011; Coppejans et al. 2015, 2016; Russell et al. 2016; Barrett et al. 2017; Pala 2019; Coppejans & Knigge 2020). As with Figure 6.9, note that the radio luminosities of the NL sample are not at the same frequency as that of previous detections.

BH relation (a factor of $\sim$4 lower). The position of SS Cyg in this X-ray:radio space is also consistent with the NLs, however, it remains to be seen if this is true for other members of the non-magnetic CVs class.

While the correlation between the X-ray and radio emission is certainly significant (see e.g. Tremou et al. (2020) for a recent discussion), the picture is more complicated in the case of NS systems. The correlation has been studied in depth in only a few systems (Migliari et al. 2003; Tudose et al. 2009; Tetarenko et al. 2016a; Gusinskaia et al. 2020), with different values of power-law index proposed by different groups. More recently a 'universal' NS correlation index of 0.44 has been suggested (Gallo et al. 2018, but see also Tudor et al. 2017).

In BH XRBs, the X-ray emission generally serves as a reliable proxy for the accretion rate, with non-thermal emission from the inner accretion flow dominating during low states (Yuan & Narayan 2014). It is during these low states that synchrotron emitting jets are observed at radio wavelengths (e.g. Corbel et al. 2000; Fender 2001). For CVs, the accretion light peaks in the UV, rather than X-ray, band. This data of course also do not allow me to demonstrate that jets are responsible for the radio emission in NLs. Given this, together with the on-going debate surrounding the X-ray:radio correlation for NS systems, and the fact that the NL radio and X-ray observations are not contemporaneous, caution should be taken against over-interpreting the position of the NLs in Figure 6.11. Nevertheless, Figure 6.11 serves to show, at the very least, that NLs can introduce confusion when classifying very low luminosity NS XRBs using their X-ray:radio properties.

As illustrated in Figure 6.12, no correlation between the rough accretion rate estimates and measured radio flux for this sample are found.

I have calculated Spearman rank correlation coefficient between various wavebands and system parameters for the sample. These are the MeerKAT specific radio luminosity of *detected* NLs in this sample, their optical and ROSAT X-ray luminosities, the mass accretion rates deduced from the SEDs and the inclination (only for those not assumed to be 57°). Figure 6.13 illustrates the results of these correlation tests. For different correlation tests, different subsets of data were used, dependent on which variables are known. No correlation test could be performed between radio luminosity and inclination, since there are only 3 targets with both variables known (V3885 Sgr, RW Sex and V603 Aql). The correlation coefficients suggest a high correlation between optical luminosity and mass accretion rate and a moderate correlation between radio and X-ray luminosity. Including TT Ari, strengthens the correlation between radio and X-ray luminosities. Furthermore, while there are not enough data to test the correlation between radio luminosities

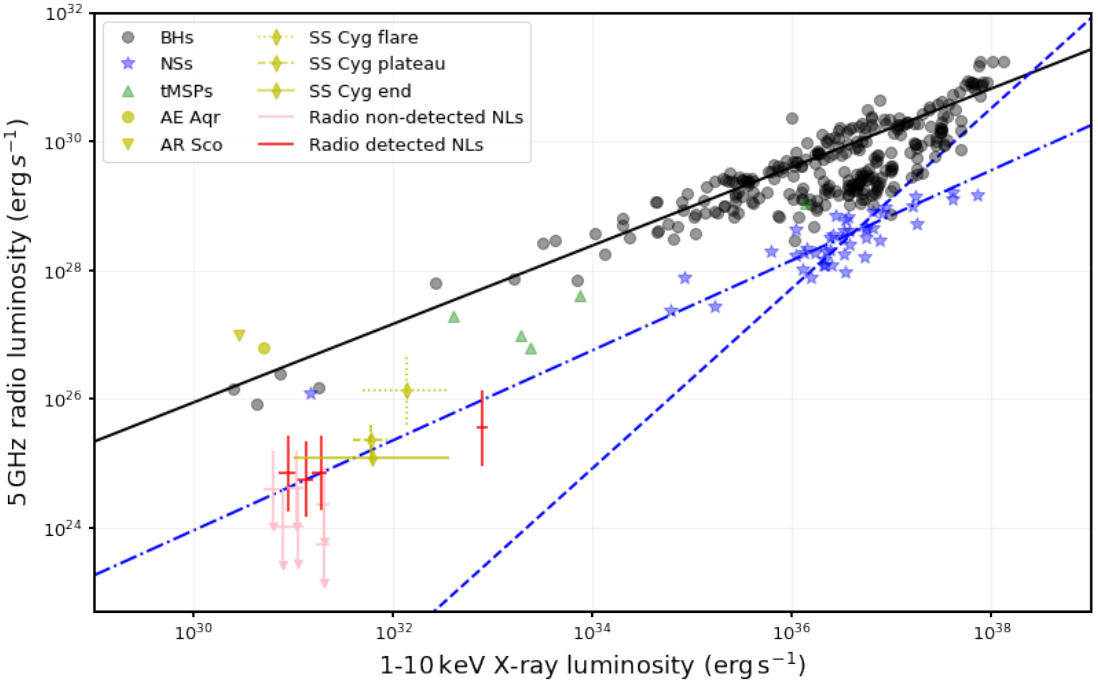

Figure 6.11: The logarithm of specific radio luminosities plotted versus the logarithm of specific X-ray luminosities for a number of black holes (as black circles), neutron stars (as blue stars), transitional millisecond pulsars (as green triangles), the sample of detected NLs (in red) and non-detected NLs (in pink) and a few other CVs (in yellow). SS Cyg has been plotted during various phases of its outburst. The X-ray:radio correlation for BHs ($L_X \propto L_R^{\sim 0.6}$; Gallo et al. 2003, 2006, 2012, 2018) is plotted as a black line, and the original correlations for non-pulsating ($L_X \propto L_R^{\sim 0.7}$) and hard-state NSs ($L_X \propto L_R^{\sim 1.4}$; Migliari & Fender 2006) are also plotted as blue dot-dashed and dashed lines, respectively. Aside from the ThunderKAT NL sample, these data were obtained from a database by Bahramian et al. (2018). Sources include: Gallo et al. (2003, 2006); Corbel et al. (2008); Coriat et al. (2011); Migliari et al. (2011); Corbel et al. (2013); Gallo et al. (2014); Russell et al. (2016); Tetarenko et al. (2016b,a); Gusinskaia et al. (2017); Plotkin et al. (2017); Tudor et al. (2017); Dinçer et al. (2018).

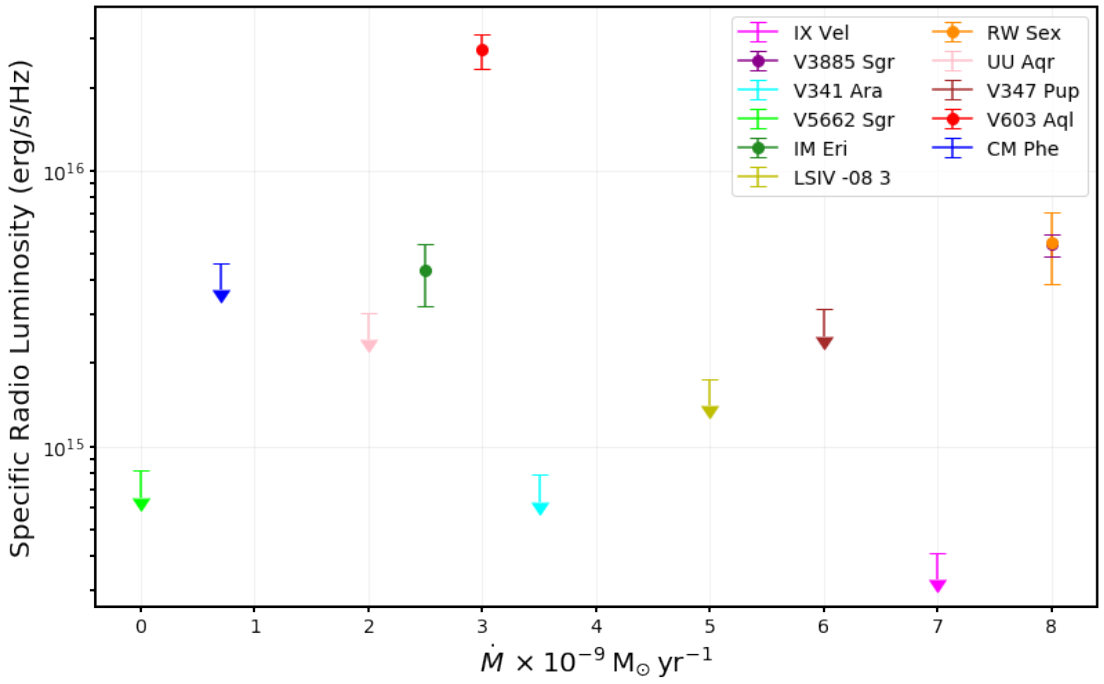

Figure 6.12: The logarithm of specific radio luminosities plotted versus $\dot{M}$ suggested by the observed SEDs and the black body disc model for the sample of NLs. The symbols for RW Sex and V3885 Sgr overlap, so only error bars for the latter can be seen.

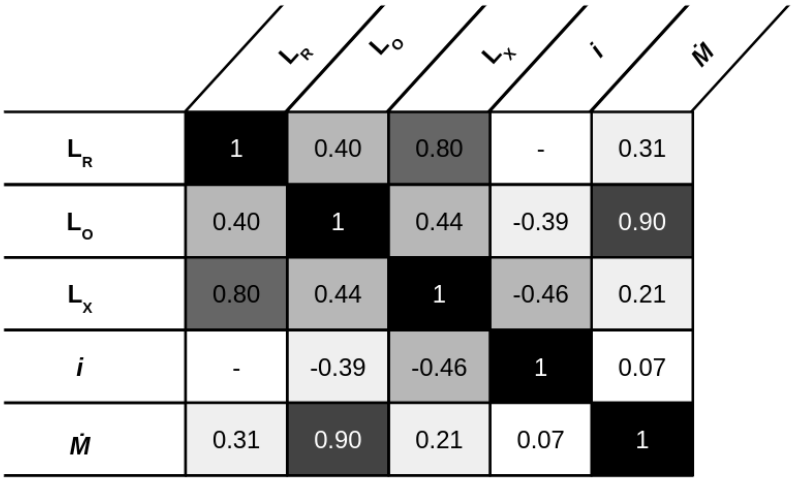

Figure 6.13: Spearman correlation coefficients between various luminosities and systems parameters. These variables are the MeerKAT radio luminosity ($L_{\rm R}$), VSX optical luminosity ($L_{\rm O}$), ROSAT X-ray luminosity ($L_{\rm X}$), inclination (i) and mass accretion rate ($\dot{M}$). There is a strong statistically significant correlation between $L_{\rm O}$ and $\dot{M}$, and a moderate correlation between $L_{\rm X}$ and $L_{\rm R}$.

and the inclinations of the sample, including TT Ari allows for such a test and results in a very strong correlation. One has to note, that TT Ari was observed a different wavelength and that the inclinations are typically not well constrained. Nevertheless, these (limited) data imply that lower inclination systems are likely brighter in the radio, suggesting that the system geometry is noteworthy and that radio emission mechanism might not be isotropic.

In Figure 6.14 the long term ASAS-SN optical light curves of these eleven NLs are shown (Shappee et al. 2014; Kochanek et al. 2017). None of the NLs in the sample are known to be a VY Scl star that would exhibit significant low states ('anti-DN outbursts') and from these light curves it is evident that none of the NLs were observed during a time of anomalous optical activity. There is thus no easy explanation as to why the three previously mentioned optically bright systems (IX Vel, LSIV -08 3 and V341 Ara) are radio faint, while the other optically bright systems are detected.

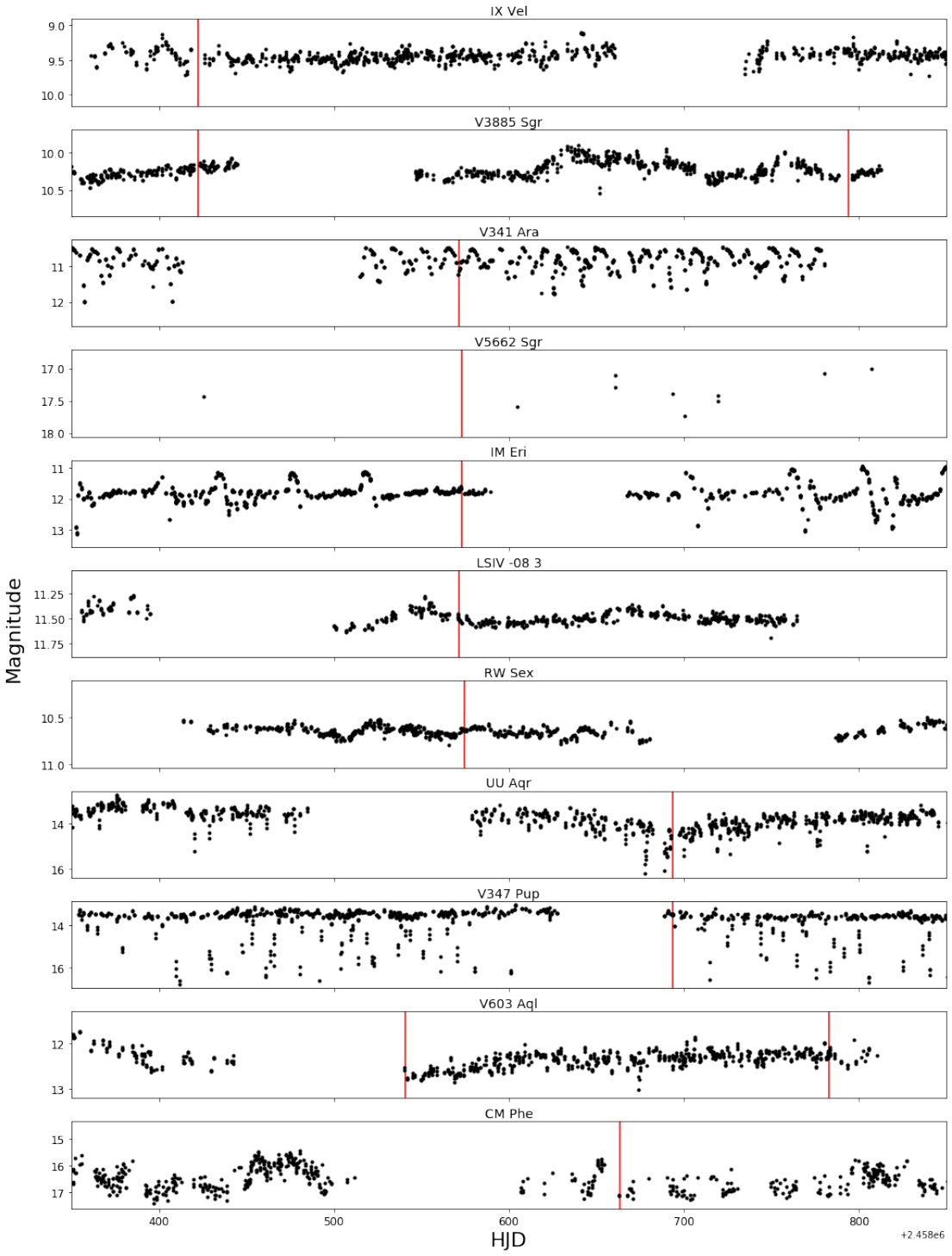

Figure 6.14: Optical light curves of the sample, covering 500 days, from the ASAS-SN variable star database (Shappee et al. 2014; Kochanek et al. 2017). The vertical red lines indicate the epochs of radio observation reported here. With the exception of V5662 Sgr, the optical light curves are well enough sampled to show that none of the targets were in a low state during the MeerKAT radio observations. Note the IW And-type photometric behaviour discussed by Kato et al. (2020) in the light curve of IM Eri.

6.5 Determining $P_{\rm orb}$ for V5662 Sgr and LSIV -08 3

Both V5662 Sgr and LSIV -08 3 are relatively poorly studied systems and although there are orbital period measurements in the literature, at least in the case of V5662 Sgr, these are periods that need confirmation. The reported period for V5662 Sgr is a photometric one, based on only two nights' data with no observed eclipses. Although a photometric signal is often present at the orbital period, with very limited phase-resolved photometry available, only the detection of eclipses allows one to be absolutely confident that a photometric period is caused by orbital variation.

The wavelength calibrated averaged spectra for V5662 Sgr and LSIV -08 3 are shown in Figure 6.15. In both systems a strong Hα emission line is one of the most prominent spectroscopic features. For V5662 Sgr, this emission line was double peaked, implying a high orbital inclination (refer to Figure 6.16 for an illustration of this). For LSIV -08 3, a broad telluric absorption line can also been seen at $\sim 6860 - 6890$ Å. All spectra were shifted to the rest wavelength before averaging, to prevent the lines from smearing out.

The radial velocity curves deduced from these spectra are presented in Fig 6.17. Radial velocity measurements that were obvious outliers, and that were consequently excluded from calculations, are indicated as crosses. These are typically data points with high a radial velocity error. For better comparison, γ (center of mass) velocities have been subtracted.

Finally the Lomb-Scargle periodograms are shown in Figure 6.18. These were calculated making use of the astropy function LombScargle (Vanderplas et al. 2012; Vanderplas & Ivezić 2015). For V5662 Sgr the first night's data only resulted in four usable spectra, which were insufficient to determine the orbital phase and hence data from this night were excluded when calculating the Lomb-Scargle periodogram. The vertical red line represents my measured orbital frequency ν_o, while lime and blue vertical lines show orbital frequencies from other literature. There are subplots embedded on Figure 6.18, zooming in on the area where the expected and observed orbital frequencies are.

From the observations taken with the SAAO 1.9 m telescope, I find orbital periods of 0.06248(96) days and 0.199(92) days for V5662 Sgr and LSIV -08 3, respectively. The false alarm probabilities for these signals are 0.3% for V5662 Sgr and 0.001% for LSIV -08 3. Tappert et al. (2004) report 0.062887(37) days as the most probable period for V5662 Sgr, based on photometric light curves obtained on 2 nights using the 0.9 m Dutch ESO telescope. The authors do note that there is still an important alias at 0.060972(14) days, and that additional observations are required to

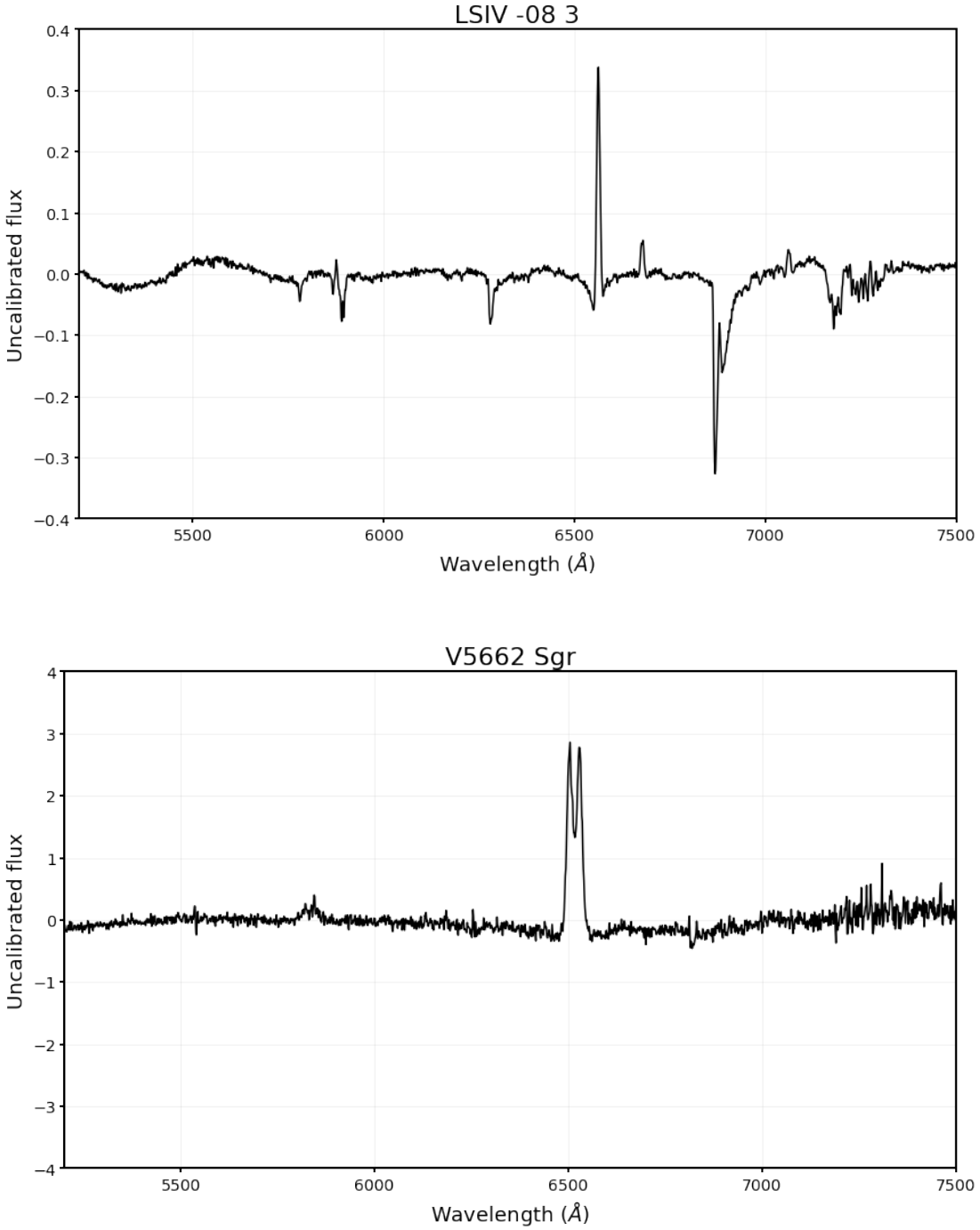

Figure 6.15: Wavelength calibrated averaged spectra for V5662 Sgr and LSIV -08 3. In both cases a strong Hα emission line, associated with the accretion disc, is one of the most prominent spectroscopic features.

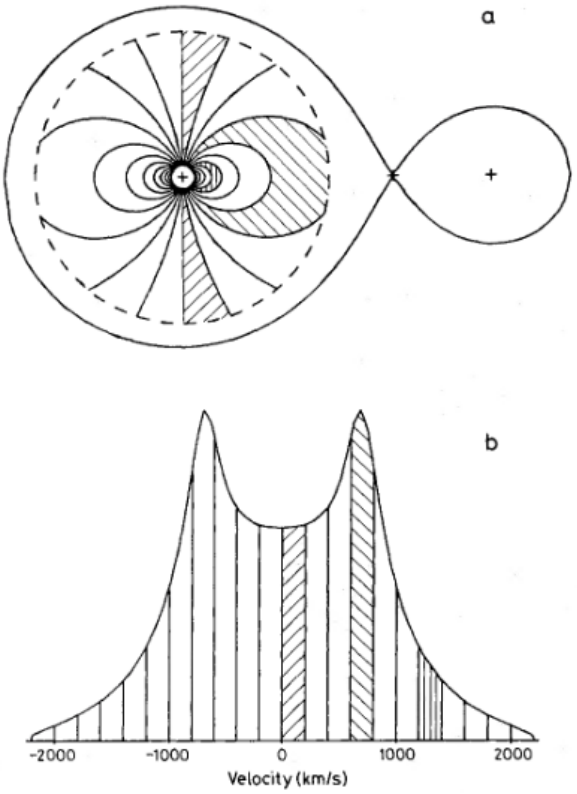

Figure 6.16: a) A Keplerian accretion disc viewed at 0° inclination. Areas of constant radial velocity have been shaded appropriately, forming a dipole field pattern. b) When observed at higher inclinations a double peaked emission line profile is observed. The shaded bins of emission are from the corresponding shaded regions in the accretion disc.

Source: Hellier, C. (2001). Cataclysmic variable stars. London: Springer, p.42. Hellier (2001)

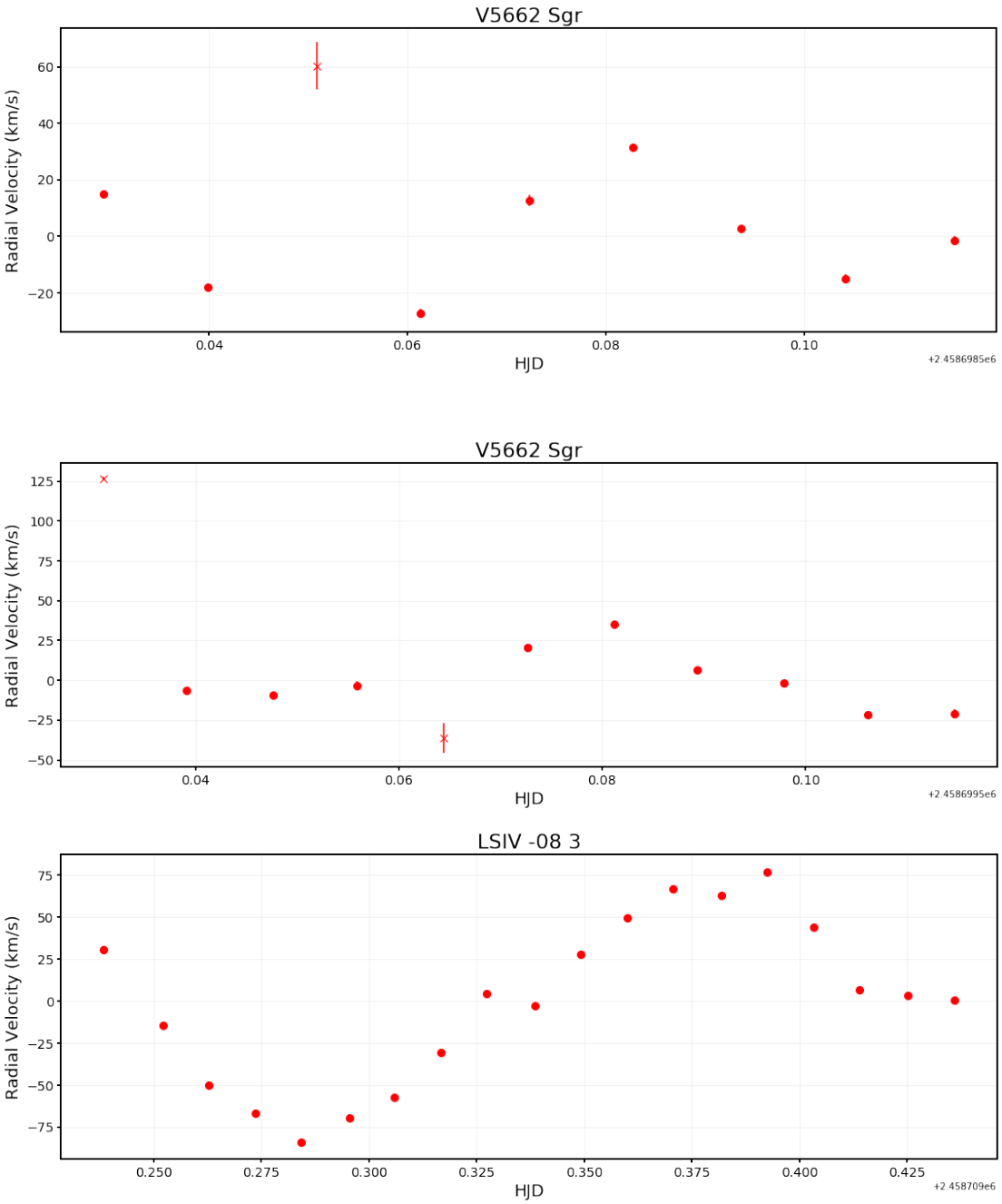

Figure 6.17: Radial velocity curves deduced from the spectra taken with the SAAO 1.9 m. telescope. The data points represented with x's (as well as the entire first night's data of V5662 Sgr; see the text for more detail) were excluded when calculating the Lomb-Scargle periodograms. In most cases the radial velocity error-bars are too small to be seen here, and so the formal error is probably underestimated.

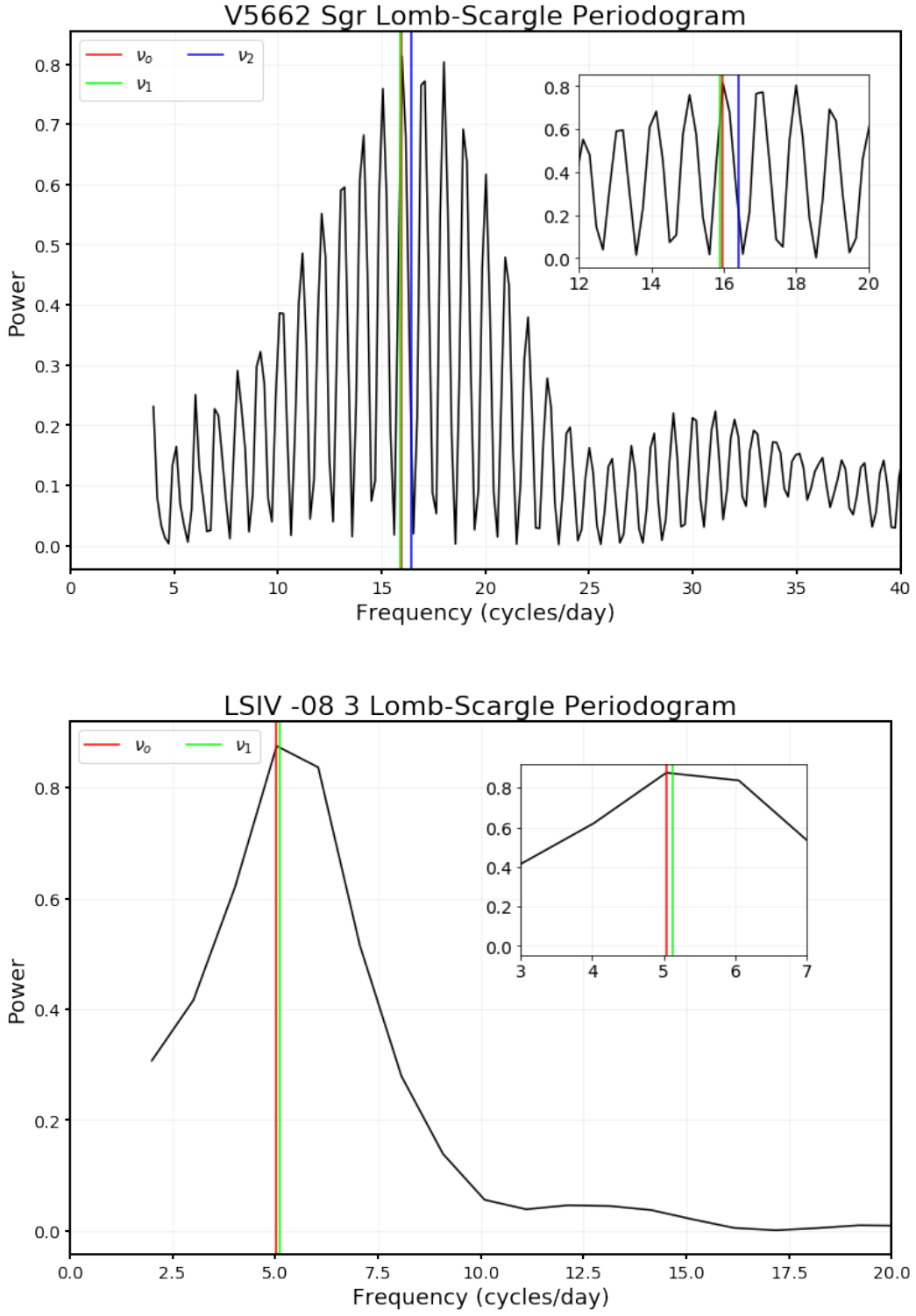

Figure 6.18: The Lomb-Scargle periodograms for V5662 Sgr and LSIV -08 3. These were calculated making use of the astropy function LombScargle (Vanderplas et al. 2012; Vanderplas & Ivezić 2015). The embedded subplots show zoomed in versions of the area where the expected and observed orbital frequencies are. The red vertical lines represent the measured (ν_o) frequency (both V5662 Sgr and LSIV -08 3). The lime and blue vertical lines (ν_1 and ν_2) represent the most probable orbital frequency, and most import alias proposed by Tappert et al. (2004) for V5662 Sgr respectively. In the case of LSIV -08 3, the vertical lime line indicates the orbital frequency measured by Stark et al. (2008).

confirm the orbital period. My measured value supports the same orbital frequency the aforementioned authors favoured. LSIV -08 3 has an orbital period of 0.1952894(10) days obtained from radial velocity studies (Stark et al. 2008). They observed LSIV -08 3 at the Kitt Peak National Observatory (KPNO) 2.1 m telescope using the GoldCam spectrograph. The orbital frequency I measure is consistent with this value.

Chapter 7

Summary

In this research dissertation I have discussed the essential background regarding cataclysmic variables (CVs), accretion and jet formation and radio interferometry. I defined a sample of eleven nearby, southern novalike (NL) CVs with measured periods, which were then observed with the MeerKAT radio interferometer as part of its ThunderKAT large survey project. I presented the results of this survey – the largest of its kind to date.

Radio emission was detected from four out of the eleven systems. These systems are: IM Eri, RW Sex, V3885 Sgr and V603 Aql. The 1.3 GHz-specific radio luminosities of these systems are between $4.3 \pm 1.2 \times 10^{15}$ and $27 \pm 4 \times 10^{15}\,\mathrm{erg\,s^{-1}\,Hz^{-1}}$. Upper limits on the specific radio luminosities of NLs not detected in the survey are between $0.4 \times 10^{15}\,\mathrm{erg\,s^{-1}\,Hz^{-1}}$ for IX Vel and $4.6 \times 10^{15}\,\mathrm{erg\,s^{-1}\,Hz^{-1}}$ for CM Phe. These non-detections are not explained by a deep low optical state. The spectral indices of the radio emission from the detected NLs ranged from -1.5 $\pm$ 1.0 to 1.2 $\pm$ 1.6, but a trend $\alpha < 0$ is observed when including data from the VLA or ATCA.

I have found no correlation between radio luminosity and binary system parameters; however, there are indications that radio emission correlates with with emission in the X-ray band and is dependent on emission in the optical band. Radio emission is only observed in systems with a high specific optical luminosity ($\gtrsim 2.2 \times 10^{18}\,\mathrm{erg\,s^{-1}\,Hz^{-1}}$ in V, at these radio detection limits; corresponding to $M_V \lesssim 6.0$). The X-ray and radio emission of the detected NLs lie on the same power law that has previously been proposed for non-pulsating NS low-mass XRBs ($L_X \propto L_R^{\sim 0.7}$).

I have plotted SEDs of the eleven NLs, overlayed with a simple $\dot{M}$-dependent black body disc model. I find that for most of the systems $\dot{M} \sim 10^{-9}\,\mathrm{M}_{\odot}\,\mathrm{yr}^{-1}$ is consistent with the apparently black body spectral component. These estimates are mostly consistent with previously proposed values. These rough $\dot{M}$-estimates do not correlate with radio emission, but do correlate with optical emission.

I obtained time-resolved optical spectroscopy of two systems, V5662 Sgr and LSIV -08 3, using the SAAO 1.9 m telescope. I used these observations to measure the orbital periods of the mentioned systems, finding values in agreement with what has previously been reported in the literature.

Prior to this work eight NLs have been observed in the radio band (V603 Aql, MV Lyr, RW Sex, TT Ari, AC Cnc, IX Vel, V3885 Sgr and V1084 Her), seven in the last decade, of which four have been detected (V3885 Sgr, RW Sex, TT Ari and V603 Aql). Seven additional NL systems (V341 Ara, V5662 Sgr, IM Eri, LSIV -08 3, UU Aqr, V347 Pup and CM Phe) have now been observed for the first time, and one novel detection (IM Eri) has been contributed.

Chapter 8

Future Prospects

The ThunderKAT NL survey has been a successful endeavour, culminating in the publication of a large amount of the research presented in this dissertation (eprint arXiv:2006.07918, accepted to MNRAS). Nevertheless, we will inevitably require a larger sample of radio observations of non-magnetic CVs to properly define the properties of the radio emission, and to investigate any possible correlations with emission at other wavelengths. In this chapter I will explore ways in which the selection criteria (presented in Section 5.1) can be adjusted to produce such a sample. I also overview observing campaigns that would be necessary to determine the physical processes responsible for radio emission in NLs.

8.1 Broadening the Horizons: The More, The Merrier

While the ThunderKAT NL survey has been successful at doubling the number of NLs with sensitive radio data, the population of radio detected NLs is still only a single digit number. More detections are crucial to identify and confirm existing correlations; particularly to delve deeper into the apparent qualitative X-ray:radio similarity that these NLs share with low-luminosity NS XRBs (see Figure 6.11). The first and most obvious means of achieving this is by adjusting the selection criteria mentioned in Section 5.1. The distance limit has been cut to 350 pc, although the strong detection of V603 Aql in multiple epochs (a NL $\approx$ 313 pc away), challenges the implementation of this distance cut. Extending the distance limit to about 500 pc, but keeping the remaining selection criteria unchanged, results in a sample of fourteen NLs, three more than were observed with the ThunderKAT survey. The additional NLs are V2214 Oph ($d \approx 464$ pc),

1SWASP J022916.91-395901.4 ($d \approx 482$ pc) and V442 Oph ($d \approx 499$ pc). This is an achievable goal for ThunderKAT, and should any of these systems be detected, the distance limit could possibly be extended even further.

Since this survey made use of MeerKAT for observations, we were limited to southern targets. The entire survey can be repeated for northern NLs, by making use of the VLA for example. Table 8.1 presents the northern NLs which satisfy the selection criteria (other than declination naturally) that were implemented in this MeerKAT NL survey; ten targets in total. V603 Aql has been excluded since it has already been observed in this MeerKAT survey. From a cursory look at literature, only two of these systems have previously been observed at radio wavelengths: TT Ari (Coppejans et al. 2015) and LS Peg (Barrett et al. 2017).

Figure 6.7 shows that the radio emission has also been detected in the 4–8 GHz and 8-10 GHz band, and also suggests that the radio emission might be brighter at even lower frequencies than 1.3 GHz. The radio emission is clearly not restricted to MeerKAT's operating frequency, and there are thus various other radio telescopes that can be used for further observations. This of course also raises the question of the broadband radio SED shape, and more specifically, the physical processes responsible for the radio emission.

8.2 Shedding the Light on What's Lighting the Shed

MeerKAT S-band (2–4 GHz) will be commissioned in the coming years. The two bright detected NLs (V3885 Sgr and V603 Aql), as well as the three optically luminous non-detected NLs (IX Vel, V341 Ara and LSIV -08 3) would be the obvious choices to observe in the S-band. It would be very interesting to see how the emission from well detected sources differs at slightly higher frequencies. Furthermore, any data that can help explain why some of the optically luminous targets have not been detected in the radio (while the vast majority have been), are invaluable. In the longer term, the SKA will be able to push the detection limits even further, and might even detect some systems that are currently not detected.

To determine/eliminate radio emission mechanisms, particularly to differentiate between synchrotron or cyclotron emission, polarisation data are crucial. Furthermore, contemporaneous multi-wavelength follow-up campaigns of the radio detected NLs are probably what would be most valuable at this stage to make advances in the field and learn more about the universality of accretion and jet formation. Particularly radio observations (to observe the possible jet emission) with simultaneous UV coverage (to monitor the accretion in CVs), as well as X-ray observations,

Table 8.1: Optical coordinates, distances, orbital periods, and observed V-band magnitude ranges for NLs in the north that satisfy the selection criteria that were implemented in this survey. The coordinates and distance measurements are from *Gaia* DR2 (Gaia Collaboration et al. 2016, 2018; Luri et al. 2018), and the magnitude ranges from The International Variable Star Index (VSX). V603 Aql has been excluded, since it has already been observed.

Target name	RA (J2000)	Dec (J2000)	Distance (pc)	Orbital period (days)	V-band magnitude range*
NSV 25966	22:50:40.0	63:28:38.3	81.0 ± 0.3	0.07134	∼16.0
TT Ari	02:06:53.1	15:17:41.8	257.5 ± 4.7	0.137551	10.2 – 16.5
V2779 Oph	18:08:35.8	10:10:29.8	285.5 ± 6.0	0.070037	16.1 – 18.5
LS Peg	21:51:57.9	14:06:53.3	287.3 ± 3.5	0.174774	11.6 – 14.3
UX UMa	13:36:41.0	51:54:49.5	297.6 ± 2.1	0.19667128	12.6 – 14.1
LY UMa	10:48:18.0	52:18:29.8	310.1 ± 4.1	0.2712788	14.3 – 15.4
RW Tri	02:25:36.2	28:05:50.9	315.0 ± 4.8	0.23188339	12.5 – 16.0
J1206+5100	12:06:15.7	51:00:47	327.9 ± 27.2	0.1366	?
FY Per	04:41:56.6	50:42:36.0	344.1 ± 7.8	0.2584	11.9 – 14.5
V1247 Her	17:11:45.1	30:13:20.1	349.3 ± 75.9	0.05579861	20.3 – ?

so that the NLs can be placed with more accuracy in the X-ray:radio luminosity plane (Figure 6.11).

So far radio detections of NLs have all been unresolved radio emission, typically a few arcseconds in diameter. Even on this scale slight extensions from the radio peak have been imaged (e.g. Körding et al. 2011). With VLBI (Very-Long-Baseline Interferometry) it is possible to obtain angular resolution on the order of milliarcseconds. Given the proximity of the NLs, it might be possible to directly image jets, assuming they do exist. Achieving this would contribute significantly to our understanding of accretion and outflow phenomena in ACOs, and undoubtedly usher in a new wave of interest in the field of cataclysmic variables.

Chapter 9

Data Acknowledgements

My research was funded by the National Research Foundation and the Newton Fund, via an NRF Competitive Support for Unrated Researchers grant and a Newton Advanced Fellowship, held by ML Pretorius.

The MeerKAT telescope is operated by the South African Radio Astronomy Observatory (SARAO), which is a facility of the National Research Foundation, an agency of the Department of Science and Innovation. I would like to thank the operators, SARAO staff and ThunderKAT Large Survey Project team.

This work has made use of data from the European Space Agency (ESA) mission *Gaia* (https://www.cosmos.esa.int/gaia), processed by the *Gaia* Data Processing and Analysis Consortium (DPAC, https://www.cosmos.esa.int/web/gaia/dpac/consortium). Funding for the DPAC has been provided by national institutions, in particular the institutions participating in the *Gaia* Multilateral Agreement.

This research has made use of the International Variable Star Index (VSX) database, operated at AAVSO, Cambridge, Massachusetts, USA.

I thank LCOGT and its staff for their continued support of ASAS-SN. ASAS-SN is supported by NSF grant AST-1515927. Development of ASAS-SN has been supported by NSF grant AST-0908816, the Center for Cosmology and AstroParticle Physics at the Ohio State University, the Mt. Cuba Astronomical Foundation and by George Skestos.

Some of the research in this paper is based on observations made with the NASA/ESA Hubble Space Telescope, and obtained from the Hubble Legacy Archive, which is a collabora-

tion between the Space Telescope Science Institute (STScI/NASA), the Space Telescope European Coordinating Facility (ST-ECF/ESAC/ESA) and the Canadian Astronomy Data Centre (CADC/NRC/CSA).

This work makes use of data products from the Two Micron All Sky Survey, which is a joint project of the University of Massachusetts and the Infrared Processing and Analysis Center/California Institute of Technology, funded by NASA and the National Science Foundation.

This research makes use of data products from the Wide-field Infrared Survey Explorer, which is a joint project of the University of California, Los Angeles and the Jet Propulsion Laboratory/California Institute of Technology, funded by NASA.

Some of the data used were obtained from the Mikulski Archive for Space Telescopes (MAST). STScI is operated by the Association of Universities for Research in Astronomy, Inc., under NASA contract NAS5-26555.

This research made use of Astropy,* a community-developed core Python package for Astronomy (Robitaille et al. 2013; Price-Whelan et al. 2018). This research made use of APLpy, an open-source plotting package for Python (Robitaille & Bressert 2012).

*http://www.astropy.org

Bibliography

Abada-Simon M., Aubier M., 1997, Astronomy and Astrophysics Supplement Series, 125, 511

Arenas J., Catalan M. S., Augusteijn T., Retter A., 2000, Monthly Notices of the Royal Astronomical Society, 311, 135

Armstrong E., et al., 2013, Monthly Notices of the Royal Astronomical Society, 435, 707

Bahramian A., et al., 2018, Radio/X-ray correlation database for X-ray binaries, doi:10.5281/ZENODO.1252036

Balbus S. A., Hawley J. F., 1991, The Astrophysical Journal, 376, 214

Balbus S. A., Hawley J. F., 1998, Reviews of Modern Physics, 70, 1

Baptista R., Bortoletto A., 2008, The Astrophysical Journal, 676, 1240

Baptista R., Steiner J. E., Cieslinski D., 1994, The Astrophysical Journal, 433, 332

Baptista R., Steiner J. E., Horne K., 1996, Monthly Notices of the Royal Astronomical Society, 282, 99

Barrett P. E., Dieck C., Beasley A. J., Singh K. P., Mason P. A., 2017, The Astronomical Journal, 154, 252

Belloni T., 2010, Lecture Notes in Physics, 794, 17

Belloni T., Homan J., Casella P., van der Klis M., Nespoli E., Lewin W. H. G., Miller J. M., Méndez M., 2005, Astronomy & Astrophysics, 440, 207

Benz A. O., Guedel M., 1989, Astronomy and Astrophysics, 218, 137

Benz A. O., Fürst E., Kiplinger A. L., 1983, Nature, 302, 45

Beuermann K., Thomas H.-C., 1990, Astronomy and Astrophysics, 230, 326

Beuermann K., Stasiewski U., Schwope A. D., 1992, Astronomy and Astrophysics, 256, 433

Bode M. F., Evans A., 2008, Classical Novae, 43

Bond H. E., Miszalski B., 2018, Publications of the Astronomical Society of the Pacific, 130, 094201

Briggs D., 1995, PhD thesis, The New Mexico Institue of Mining and Technology, http://www.aoc.nrao.edu/dissertations/dbriggs/

Bright J. S., et al., 2020, Nature Astronomy

Brocksopp C., Sokoloski J. L., Kaiser C., Richards A. M., Muxlow T. W., Seymour N., 2004, Monthly Notices of the Royal Astronomical Society, 347, 430

Buckley D. A. H., Sullivan D. J., Remillard R. A., Tuohy I. R., Clark M., 1990, The Astrophysical Journal, 355, 617

Chanmugam G., 1987, Astrophysics and Space Science, 130, 53

Chanmugam G., Dulk G. A., 1981, The Astrophysical Journal, 244, 569

Charbonneau P., MacGregor K. B., 1997, The Astrophysical Journal, 486, 502

Chen A., O'Donoghue D., Stobie R. S., Kilkenny D., Warner B., 2001, Monthly Notices of the Royal Astronomical Society, 325, 89

Clark B. G., 1980, Astronomy and Astrophysics, 89, 377

Copeland H., Jensen J. O., Jorgensen H. E., 1970, Astronomy and Astrophysics, 5, 12

Coppejans D., Knigge C., 2020, eprint arXiv:2003.05953

Coppejans D. L., Körding E. G., Miller-Jones J. C. A., Rupen M. P., Knigge C., Sivakoff G. R., Groot P. J., 2015, Monthly Notices of the Royal Astronomical Society, 451, 3801

Coppejans D. L., et al., 2016, Monthly Notices of the Royal Astronomical Society, 463, 2229

Corbel S., Fender R. P., Tzioumis A. K., Nowak M., McIntyre V., Durouchoux P., Sood R., 2000, Astronomy and Astrophysics, 359, 251

Corbel S., Nowak M. A., Fender R. P., Tzioumis A. K., Markoff S., 2003, Astronomy & Astrophysics, 400, 1007

Corbel S., Koerding E., Kaaret P., 2008, Monthly Notices of the Royal Astronomical Society, 389, 1697

Corbel S., Coriat M., Brocksopp C., Tzioumis A. K., Fender R. P., Tomsick J. A., Buxton M. M., Bailyn C. D., 2013, Monthly Notices of the Royal Astronomical Society, 428, 2500

Cordova F. A., Hjellming R. M., Mason K. O., 1983, Publications of the Astronomical Society of the Pacific, 95, 69

Coriat M., et al., 2011, Monthly Notices of the Royal Astronomical Society, 414, 677

Coriat M., Fender R. P., Dubus G., 2012, Monthly Notices of the Royal Astronomical Society, 424, 1991

Crause L. A., et al., 2016, in Ground-based and Airborne Instrumentation for Astronomy VI. SPIE, p. 990827, doi:10.1117/12.2230818

Cropper M., 1990, Space Science Reviews, 54, 195

Davis P. J., Kolb U., Willems B., Gänsicke B. T., 2008, Monthly Notices of the Royal Astronomical Society, 389, 1563

Dinçer T., Bailyn C. D., Miller-Jones J. C. A., Buxton M., MacDonald R. K. D., 2018, The Astrophysical Journal, 852, 4

Downes R. A., Webbink R. F., Shara M. M., 1997, VizieR Online Data Catalog, p. V/94

Dubus G., Otulakowska-Hypka M., Lasota J. P., 2018, Astronomy and Astrophysics, 617, A26

Dulk G. A., Bastian T. S., Chanmugam G., 1983, The Astrophysical Journal, 273, 249

Eggleton P. P., 1976, in Eggleton P., Mitton S., Whelan W., eds, Structure and Evolution of Close Binary Systems. Cambridge, p. 209

Esin A. A., McClintock J. E., Narayan R., 1997, The Astrophysical Journal, 489, 865

Espinasse M., Fender R., 2018, Monthly Notices of the Royal Astronomical Society, 473, 4122

Falcke H., Kording E., Markoff S., 2004, Astronomy and Astrophysics, 414, 895

Faulkner J., 1971, The Astrophysical Journal, 170, L99

Faulkner J., Lin D. N. C., Papaloizou J., 1983, Monthly Notices of the Royal Astronomical Society, 205, 359

Fender R. P., 2001, Monthly Notices of the Royal Astronomical Society, 322, 31

Fender R. P., Belloni T. M., Gallo E., 2004a, Monthly Notices of the Royal Astronomical Society, Volume 355, Issue 4, pp. 1105-1118., 355, 1105

Fender R., Wu K., Johnston H., Tzioumis T., Jonker P., Spencer R., van der Klis M., 2004b, Nature, 427, 222

Fender R., et al., 2017, eprint arXiv:1711.04132

Fender R., Bright J., Mooley K., Miller-Jones J., 2019, Monthly Notice of the Royal Astronomical Society, 490, L76

Flannery B. P., 1975, The Astrophysical Journal, 201, 661

Frank J., King A., Raine D., 1992, Accretion power in astrophysics.. Vol. 21, Cambridge University Press

Frew D. J., 2008, PhD Thesis, 2008, 477 + xxii pages, Department of Physics, Macquarie University, Sydney, Australia

Fuerst E., Benz A., Hirth W., Kiplinger A., Geffert M., 1986, Astronomy and Astrophysics, 154, 377

Gaia Collaboration et al., 2016, Astronomy and Astrophysics, 595, A1

Gaia Collaboration Brown A. G. A., Vallenari A., Prusti T., de Bruijne J. H. J., Babusiaux C., Bailer-Jones C. A. L., 2018, Astronomy & Astrophysics, 616, A1

Gallo E., Fender R., Pooley G., 2003, Monthly Notice of the Royal Astronomical Society, 344, 60

Gallo E., Fender R., Hynes R., 2005, Monthly Notices of the Royal Astronomical Society, 356, 1017

Gallo E., Fender R., Miller-Jones J., Merloni A., Jonker P., Heinz S., Maccarone T., van der Klis M., 2006, Monthly Notices of the Royal Astronomical Society, 370, 1351

Gallo E., Miller B. P., Fender R., 2012, Monthly Notices of the Royal Astronomical Society, 423, 590

Gallo E., et al., 2014, Monthly Notices of the Royal Astronomical Society, 445, 290

Gallo E., Degenaar N., van den Eijnden J., 2018, Monthly Notice of the Royal Astronomical Society, 478, L132

Garrison R. F., Hiltner W. A., Schild R. E., 1977, The Astrophysical Journal Supplement Series, 35, 111

Garrison R., Hiltner W., Schild R., 1982, IAU Circ., No. 3730, #2 (1982). Edited by Marsden, B. G., 3730

Greenstein J. L., Oke J. B., 1982, The Astrophysical Journal, 258, 209

Gudel M., Schmitt J. H. M. M., Bookbinder J. A., Fleming T. A., 1993, The Astrophysical Journal, 415, 236

Gusinskaia N. V., et al., 2017, Monthly Notices of the Royal Astronomical Society, 470, 1871

Gusinskaia N. V., et al., 2020, Monthly Notices of the Royal Astronomical Society, 492, 2858

Hamaker J. P., 2000, Astronomy and Astrophysics Supplement Series, 143, 515

Hamaker J. P., Bregman J. D., Sault R. J., 1996, Astronomy and Astrophysics Supplement, 117, 137

Hameury J.-M., King A. R., Lasota J.-P., 1986, Monthly Notices of the Royal Astronomical Society, 218, 695

Hameury J. M., Lasota J. P., Knigge C., Körding E. G., 2017, Astronomy and Astrophysics, 600, A95

Hannikainen D. C., Hunstead R. W., Campbell-Wilson D., Sood R. K., 1998, Astronomy and Astrophysics, 337, 460

Harrop-Allin M. K., Warner B., 1996, Monthly Notices of the Royal Astronomical Society, 279, 219

Hartley L. E., Murray J. R., Drew J. E., Long K. S., 2005, Monthly Notices of the Royal Astronomical Society, 363, 285

Hawley J. F., Balbus S. A., 1991, The Astrophysical Journal, 376, 223

Heinz S., Sunyaev R., 2003, Monthly Notices of the Royal Astronomical Society, 343, L59

Hellier C., 1996, The Astrophysical Journal, 471, 949

Hellier C., 2001, Cataclysmic Variable Stars. Springer

Hellier C., Beardmore A. P., 2002, Monthly Notices of the Royal Astronomical Society, 331, 407

Hillwig T., Livio M., Honeycutt R., 2004, Publications of the Astronomical Society of the Pacific, 116, 397

Hirose M., Osaki Y., 1990, Publications of the Astronomical Society of Japan, 42, 135

Hjellming R. M., Rupen M. P., 1995, Nature, 375, 464

Hoard D., Wachter S., Kim-Quijano J., 2001, Publications of the Astronomical Society of the Pacific, 113, 482

Hoffmeister C., 1956, Veroeff. Sternwarte Sonneberg, 3, 1

Högbom J. A., 1974, Astronomy and Astrophysics Supplement, 15, 417

Honeycutt R. K., Robertson J. W., Turner G. W., 1998, The Astronomical Journal, 115, 2527

Hoshi R., 1979, Progress of Theoretical Physics, 61, 1307

Howell S. B., Ciardi D. R., 2001, The Astrophysical Journal, 550, L57

Jaidee S., Lyngå G., 1969, Arkiv for Astronomi, 5, 345

Jennison R. C., 1958, Monthly Notices of the Royal Astronomical Society, 118, 276

Johnson C. B., Schaefer B. E., Kroll P., Henden A. A., 2014, The Astrophysical Journal, 780, L25

Jonas J. L., 2009, Proceedings of the IEEE, 97, 1522

Kahabka P., van den Heuvel E. P. J., 1997, Annual Review of Astronomy and Astrophysics, 35, 69

Kato T., et al., 2020, PASJ, 72, 11

Kazarovets E. V., Samus N. N., Durlevich O. V., Kireeva N. N., Pastukhova E. N., 2013, Information Bulletin on Variable Stars, 6052, 1

Kellogg E., Pedelty J. A., Lyon R. G., 2001, The Astrophysical Journal, 563, L151

Kilkenny D., Busse J., 1992, Monthly Notices of the Royal Astronomical Society, 258, 57

King A. R., Wynn G. A., 1999, Monthly Notices of the Royal Astronomical Society, 310, 203

Kiraga M., 2012, Acta Astronomica, 62, 67

Klein-Wolt M., Van der Klis M., 2008, The Astrophysical Journal, 675, 1407

Knigge C., Baraffe I., Patterson J., 2011, Astrophysical Journal, Supplement Series, 194, 28

Kochanek C. S., et al., 2017, Publications of the Astronomical Society of the Pacific, 129, 104502

Kolb U., Baraffe I., 1999, Monthly Notices of the Royal Astronomical Society, 309, 1034

Kording E. G., Jester S., Fender R., 2006, Monthly Notices of the Royal Astronomical Society, 372, 1366

Körding E., Rupen M., Knigge C., Fender R., Dhawan V., Templeton M., Muxlow T., 2008, Science, 320, 1318

Körding E. G., Knigge C., Tzioumis T., Fender R., 2011, Monthly Notices of the Royal Astronomical Society: Letters, 418, L129

Kraft R. P., Mathews J., Greenstein J. L., 1962, The Astrophysical Journal, 136, 312

Krautter J., Klare G., Wolf B., Duerbeck H., Rahe J., Vogt N., Wargau W., 1981, Astronomy and Astrophysics, 102, 337

Kurbatov E. P., Zhilkin A. G., Bisikalo D. V., 2018, eprint arXiv:1808.04584

Kurbatov E. P., Zhilkin A. G., Bisikalo D. V., 2019, Astronomy Reports, 63, 25

Kurtz M., Mink D., 1998, Publications of the Astronomical Society of the Pacific, 110, 934

Kuulkers E., Fender R. P., Spencer R. E., Davis R. J., Morison I., 1999, Monthly Notices of the Royal Astronomical Society, 306, 919

Lasota J.-P., 2001, New Astronomy Reviews, 45, 449

Liebert J., Stockman H. S., 1985, in Lamb D., Patterson J., eds, , Cataclysmic Variables and Low-Mass X-ray Binaries. Cambridge, pp 151–177, doi:10.1007/978-94-009-5319-2˙20

Linnell A. P., Godon P., Hubeny I., Sion E. M., Szkody P., 2007, The Astrophysical Journal, 662, 1204

Linnell A. P., Godon P., Hubeny I., Sion E. M., Szkody P., Barrett P. E., 2009, The Astrophysical Journal, 703, 1839

Linnell A. P., Godon P., Hubeny I., Sion E. M., Szkody P., 2010, The Astrophysical Journal, 719, 271

Littlefair S. P., Dhillon V. S., Marsh T. R., Gänsicke B. T., 2006, Monthly Notices of the Royal Astronomical Society, 371, 1435

Livio M., 1999, Physics Reports, 311, 225

Livio M., Pringle J. E., 1994, The Astrophysical Journal, 427, 956

Lubow S. H., 1991, The Astrophysical Journal, 381, 268

Lubow S. H., Shu F. H., 1975, The Astrophysical Journal, 198, 383

Luri X., et al., 2018, Astronomy and Astrophysics, 616, A9

MacGregor K. B., Charbonneau P., 1997, The Astrophysical Journal, 486, 484

Maccarone T. J., 2003, Astronomy and Astrophysics, 409, 697

Marsh T. R., et al., 2016, Nature, 537, 374

McLean M., Berger E., Reiners A., 2012, ApJ, 746, 23

McMullin J. P., Waters B., Schiebel D., Young W., Golap K., 2007, in Richard A. Shaw Frank Hill David J. Bell. eds, Astronomical Data Analysis Software and Systems XVI ASP Conference Series. Tucson, p. 127

Meintjes P. J., 2016a, Technical report, Magnetic Reconnection and Transient Phenomena in Accretion Driven Systems

Meintjes P. J., 2016b, Technical report, Magnetically driven transient phenomena in accretion driven systems: New breakthroughs with MeerKAT and CTA

Melrose D. B., Dulk G. A., 1982, The Astrophysical Journal, 259, 844

Merloni A., Heinz S., Di Matteo T., 2003, Monthly Notices of the Royal Astronomical Society, 345, 1057

Migliari S., Fender R. P., 2006, Monthly Notices of the Royal Astronomical Society, 366, 79

Migliari S., Fender R., Rupen M., Jonker P., Klein-Wolt M., Hjellming R., van der Klis M., 2003, Monthly Notices of the Royal Astronomical Society, 342, L67

Migliari S., Fender R. P., Rupen M., Wachter S., Jonker P. G., Homan J., van der Klis M., 2004, Monthly Notices of the Royal Astronomical Society, 351, 186

Migliari S., Miller-Jones J. C., Russell D. M., 2011, Monthly Notices of the Royal Astronomical Society, 415, 2407

Miller-Jones J. C. A., et al., 2011, in Proc. IAU Symp. 275. Cambridge University Press, p. 224

Miller-Jones J. C. A., et al., 2012, Monthly Notices of the Royal Astronomical Society: Letters, 419, L49

Mirabel I. F., Rodríguez L. F., 1994, in AIPC. AIP Publishing, pp 413–420, doi:10.1063/1.45597

Molenaar G., et al., 2017, Fundamentals of Radio Interferometry for Aperture Synthesis. https://github.com/ratt-ru/fundamentals_of_interferometry

Mooley K. P., et al., 2017, Monthly Notices of the Royal Astronomical Society, 467, L31

Motch C., , Astronomy and Astrophysics, 338, L13

Nassau J. J., Stephenson C. B., 1963, Hamburger Sternw., Warner & Swasey Obs., 4 (1963)

Nelemans G., 2005, in Hameury J. M., Lasota J. P., eds, Vol. 330, The Astrophysics of Cataclysmic Variables and Related Objects. San Francisco, p. 27 (http://arxiv.org/abs/0409676 arXiv:0409676)

Nelson R. F., Spencer R. E., 1988, Monthly Notices of the Royal Astronomical Society, 234, 1105

Offringa A. R., 2010, ascl, p. ascl:1010.017

Offringa A. R., van de Gronde J. J., Roerdink J. B. T. M., , Astronomy & Astrophysics, 539, A95

Osaki Y., 1974, Publications of the Astronomical Society of Japan, 26, 429

Osaki Y., 1985, Astronomy and Astrophysics, 144, 369

Osaki Y., 1996, Publications of the Astronomical Society of the Pacific, 108, 39

Paczyński B., 1967, Acta Astronomica, 17, 287

Paczynski B., 1976, in Eggleton P., Mitton S., Whelan J., eds, Structure and Evolution of Close Binary Systems. D. Reidel Publishing Co. (IAU Symposium No. 73), Cambridge, p. 75

Paczynski B., Sienkiewicz R., 1981, The Astrophysical Journal, 248, L27

Paczynski B., Sienkiewicz R., 1983, The Astrophysical Journal, 268, 825

Pala A. F., 2019, Technical report, Fundamental properties of Cataclysmic Variables from Gaia DR2

Patterson J., 1994, Publications of the Astronomical Society of the Pacific, 106, 209

Patterson J., 1999, Frontier Science Series, 26

Patterson J., Raymond J. C., 1985a, The Astrophysical Journal, 292, 535

Patterson J., Raymond J. C., 1985b, The Astrophysical Journal, 292, 550

Patterson J., et al., 2005, Publications of the Astronomical Society of the Pacific, 117, 1204

Payne-Gaposchkin C., 1964, The galactic novae. Dover Publication, New York

Peters C., Thorstensen J., 2006, Publications of the Astronomical Society of the Pacific, 118, 687

Pickering E. C., 1907, Astronomische Nachrichten, 175, 333

Plotkin R. M., Gallo E., Markoff S., Homan J., Jonker P. G., Miller-Jones J. C. A., Russell D. M., Drappeau S., , Monthly Notices of the Royal Astronomical Society, 446, 4098

Plotkin R. M., Gallo E., Jonker P. G., 2013, Astrophysical Journal, 773, 59

Plotkin R. M., et al., 2017, The Astrophysical Journal, 848, 92

Pretorius M. L., Knigge C., 2011, Monthly Notices of the Royal Astronomical Society, 419, 1442

Price-Whelan A. M., et al., 2018, The Astronomical Journal, 156, 123

Prinja R. K., Rosen R., 1995, Monthly Notices of the Royal Astronomical Society, 273, 461

Quaintrell H., Fender R. P., 1998, eprint arXiv:astro-ph/9804275

Rappaport S., Joss P. C., Webbink R. F., 1982, The Astrophysical Journal, 254, 616

Rappaport S., Joss P. C., Verbunt F., 1983, The Astrophysical Journal, 275, 713

Rebassa-Mansergas A., Parsons S. G., Copperwheat C. M., Justham S., Gaensicke B. T., Schreiber M. R., Marsh T. R., Dhillon V. S., 2014, ApJ, 790, 28

Remillard R. A., McClintock J. E., 2006, Annual Review of Astronomy and Astrophysics, 44, 49

Retter A., Naylor T., 2000, Monthly Notices of the Royal Astronomical Society, 319, 510

Ribeiro F. M. A., Diaz M. P., 2007, The Astronomical Journal, 133, 2659

Ritter H., Kolb U., 2003, Astronomy and Astrophysics, 404, 301

Robitaille T., Bressert E., 2012, ascl, p. ascl:1208.017

Robitaille T. P., et al., 2013, Astronomy and Astrophysics, 558, A33

Rushton A. P., et al., 2016, eprint arXiv:1608.02886, 8, 1

Russell D. M., Miller-Jones J. C. A., Maccarone T. J., Yang Y. J., Fender R. P., Lewis F., 2011, The Astrophysical Journal, 739, L19

Russell T. D., et al., 2016, Monthly Notices of the Royal Astronomical Society, 460, 3720

Russell T. D., et al., 2019, The Astrophysical Journal, 883, 198

Schmidt G. D., Hoard D. W., Szkody P., Melia F., Honeycutt R. K., Wagner R. M., 1999, The Astrophysical Journal, 525, 407

Schwab F. R., 1984, The Astronomical Journal, 89, 1076

Shakura N. I., Sunyaev R. A., 1973, Astronomy and Astrophysics, 500, 33

Shakura N., Sunyaev R., 1976, Monthly Notices of the Royal Astronomical Society, 175, 613

Shappee B. J., et al., 2014, The Astrophysical Journal, 788, 48

Shara M. M., 1989, Publications of the Astronomical Society of the Pacific, 101, 5

Shara M. M., Livio M., Moffat A. F. J., Orio M., 1986, The Astrophysical Journal, 311, 163

Silber A. D., 1992, PhD Thesis, Massachusetts Institute of Technology

Sion E. M., 1985, The Astrophysical Journal, 292, 601

Smak J., 1971, Acta Astronomica, 21, 467

Smirnov O., Tasse C., 2015, Monthly Notices of the Royal Astronomical Society, 449, 2668

Smith D. A., Dhillon V. S., 1998, Monthly Notices of the Royal Astronomical Society, 301, 767

Sokoloski J. L., Rupen M. P., Mioduszewski A. J., 2008, The Astrophysical Journal, 685, L137

Southwell K. A., Livio M., Charles P. A., O'Donoghue D., Sutherland W. J., 1996, Astrophysical Journal v.470, p.1065, 470, 1065

Spruit H. C., Ritter H., 1983, Astronomy and astrophysics.. Vol. 124, EDP Sciences [etc.]

Stark M. A., Wade R. A., Thorstensen J. R., Peters C. S., Smith H. A., Miller R. D., Green E. M., 2008, The Astronomical Journal, 135, 991

Starrfield S., Truran J. W., Sparks W. M., 2000, The nova outburst: Thermonuclear runaways on degenerate dwarfs, doi:10.1016/S1387-6473(00)00018-X

Still M. D., Buckley D. A. H., Garlick M. A., 1998, Monthly Notices of the Royal Astronomical Society, 299, 545

Tapia S., 1977, The Astrophysical Journal, 212, L125

Tappert C., Augusteijn T., Maza J., 2002, in Gänsicke B. T., Beuermann K., Reinsch K., eds, The Physics of Cataclysmic Variables and Related Objects. San Francisco: Astronomical Society of the Pacific (http://arxiv.org/abs/0109557 `arXiv:0109557`)

Tappert C., Augusteijn T., Maza J., 2004, Monthly Notices of the Royal Astronomical Society, 354, 321

Tasse C., et al., 2018, A&A, 611, A87

Taylor A. R., Seaquist E. R., Mattei J. A., 1986, Nature, 319, 38

Taylor G. B., Carilli C. L., Perley R. A., 1999, Synthesis Imaging in Radio Astronomy II, 180

Tetarenko A. J., et al., 2016a, Monthly Notices of the Royal Astronomical Society, 460, 345

Tetarenko B. E., et al., 2016b, ApJ, 825, 10

Tetarenko A. J., et al., 2017, Monthly Notices of the Royal Astronomical Society, 469, 3141

Thompson A. R., Moran J. M., Swenson G. W., 2017, Interferometry and Synthesis in Radio Astronomy. Astronomy and Astrophysics Library, Springer International Publishing, Cham, doi:10.1007/978-3-319-44431-4

Thoroughgood T. D., et al., 2005, Monthly Notices of the Royal Astronomical Society, 357, 881

Thorstensen J. R., 2020, arXiv eprints 2005.02150

Thorstensen J. R., Ringwald F. A., Wade R. A., Schmidt G. D., Norsworthy J. E., 1991, The Astronomical Journal, 102, 272

Tomov T., Munari U., Kolev D., Tomasella L., Rejkuba M., 1998, Astronomy and Astrophysics, 333, L67

Tomov T., Munari U., Marrese P., 2000, Astronomy and Astrophysics, 354, L25

Townsley D. M., Gänsicke B. T., 2009, Astrophysical Journal, 693, 1007

Tremou E., et al., 2020, Monthly Notice of the Royal Astronomical Society, 493, L132

Tudor V., et al., 2017, Monthly Notices of the Royal Astronomical Society, 470, 324

Tudose V., Fender R. P., Linares M., Maitra D., van der Klis M., 2009, Monthly Notices of the Royal Astronomical Society, 400, 2111

Turner K. C., 1985, in Hjellming Robert Gobson D., eds, , Vol. 116, Radio Stars. pp 283–288, doi:10.1007/978-94-009-5420-5˙41

Vande Putte D., Smith R. C., Hawkins N. A., Martin J. S., 2003, Monthly Notice of the Royal Astronomical Society, 342, 151

Vanderplas J. T., Ivezić Ž., 2015, Astrophysical Journal, 812, 18

Vanderplas J., Connolly A. J., Ivezic Z., Gray A., 2012, in Proceedings - 2012 Conference on Intelligent Data Understanding, CIDU 2012. pp 47–54 (http://arxiv.org/abs/1411.5039 arXiv:1411.5039), doi:10.1109/CIDU.2012.6382200

Verbunt F., Zwaan C., 1981, Astronomy and Astrophysics, 100, L7

Voges W., et al., 1999, Astronomy and Astrophysics, 349, 389

Vogt N., 1982, The Astrophysical Journal, 252, 653

Volkov I. M., Shugarov S. Y., Seregina T. M., 1986, Astronomicheskij Tsirkulyar, 1418, 3

Warner B., 1987, Monthly Notices of the Royal Astronomical Society, 227, 23

Warner B., 1995, Cataclysmic variable stars. Vol. 5

Warner B., 2006, he Journal of the American Association of Variable Star Observers, 35, 98

Whitehurst R., 1988, Monthly Notices of the Royal Astronomical Society, 232, 35

Wu K., Wickramasinghe D. T., Warner B., 1995, Proceedings of the Astronomical Society of Australia, 12, 60

Wynn G. A., King A. R., Horne K., 1997, Monthly Notices of the Royal Astronomical Society, 286, 436

Yuan F., Narayan R., 2014, Annual Review of Astronomy and Astrophysics, 52, 529

Zorotovic M., et al., 2016, Monthly Notices of the Royal Astronomical Society, 457, 3867

van den Heuvel E. P. J., Bhattacharya D., Nomoto K., Rappaport S. A., 1992, Astronomy and Astrophysics, 262, 97

van Dokkum P., 2001, Publications of the Astronomical Society of the Pacific, 113, 1420